Biomolecular Ions in Superfluid Helium Nanodroplets

Dissertation zur Erlangung des Grades
eines Doktors der Naturwissenschaften (Dr. rer. nat.)
am Fachbereich Physik
der Freien Universitt Berlin

von

Ana Isabel González Flórez

Berlin

Januar 2016

Fritz-Haber-Institut
der Max-Planck-Gesellschaft

Freie Universität Berlin

Abstract

The function of a biological molecule is closely related to its structure. As a result, understanding and predicting biomolecular structure has become the focus of an extensive field of research. However, the investigation of molecular structure can be hampered by two main difficulties: the inherent complications that may arise from studying biological molecules in their native environment, and the potential congestion of the experimental results as a consequence of the large number of degrees of freedom present in these molecules.

In this work, a new experimental setup has been developed and established in order to overcome the afore mentioned limitations combining structure-sensitive gas-phase methods with superfluid helium droplets. First, biological molecules are ionised and brought into the gas phase, often referred to as a clean-room environment, where the species of interest are isolated from their surroundings and, thus, intermolecular interactions are absent. The mass-to-charge selected biomolecules are then embedded inside clusters of superfluid helium with an equilibrium temperature of ~ 0.37 K. As a result, the internal energy of the molecules is lowered, thereby reducing the number of populated quantum states. Finally, the local hydrogen bonding patterns of the molecules are investigated by probing specific vibrational modes using the Fritz Haber Institute's free electron laser as a source of infrared radiation.

Although the structure of a wide variety of molecules has been studied making use of the sub-Kelvin environment provided by superfluid helium droplets, the suitability of this method for the investigation of biological molecular ions was still unclear. However, the experimental results presented in this thesis demonstrate the applicability of this experimental approach in order to study the structure of intact, large biomolecular ions and the first vibrational spectrum of the protonated pentapeptide leu-enkephalin embedded in helium droplets has been recorded. The experimental results show well resolved spectra, which are in good agreement with theoretical calculations. Moreover, the weakly interacting nature of helium droplets is confirmed by the excellent agreement obtained with the available gas-phase data.

Using standard gas-phase mass spectrometry techniques allows to study the molecular ions as a function of charge state. As a result, the role of the interplay between Coulomb repulsion and hydrogen bonding in the secondary structure of the target molecules can be investigated. For this purpose, the infrared spectra of the proteins ubiquitin and cytochrome c embedded in helium droplets were recorded. The experimental results are interpreted in terms of a charge-induced unzipping of the proteins, where a structural transition from helical into extended C_5-type hydrogen bonded structures occurs. This interpretation is supported by simple energy considerations, as well as by quantum chemical calculations on

model peptides. The transition in secondary structure observed here is most likely universal for isolated proteins in the gas phase.

Embedding positively charged ions inside helium droplets also offers the possibility to directly investigate the intrinsic properties of helium droplets. One fundamental characteristic of helium droplets is their unique ability to pick up the species with which they collide. In order to gain more insight into this process, the presence of an electrical charge was used to accelerate and detect the ion-doped droplets as a function of the mass and size of the dopant. A systematic investigation of the pick-up probability demonstrates the existence of a dopant dependent minimum droplet size below which no pick-up occurs. As a result, different hypotheses and theoretical models are proposed and discussed in order to shed more light into the constraints and limitations of the pick-up process.

Zusammenfassung

Die Struktur und Funktion von Biomolekülen sind eng miteinander verknüpft und bilden den Schwerpunkt eines umfangreichen Forschungsgebiets. Insbesondere die Bestimmung und Vorhersage biomolekularer Strukturen ist hierbei von großer Bedeutung, um ein Verständnis über molekulare Prozesse zu erlangen. Allerdings kann das Erforschen dieser Strukturen durch zwei Hauptfaktoren erschwert werden: Zum einen kann die natürliche biologische Umgebung durch ihre komplexen Eigenschaften Komplikationen hervorrufen; zum anderen kann die große Anzahl an Freiheitsgraden dieser Moleküle zu einer Überlagerung in den experimentellen Ergebnissen führen.

In dieser Arbeit wurde ein neuer Versuchsaufbau entwickelt, der struktursensitive Methoden der Gasphasenanalytik mit dem Ansatz der suprafluiden Heliumtröpfchen-Methode kombiniert, um die zuvor erwähnten Einschränkungen zu überwinden. Hierfür werden die Biomoleküle zunächst ionisiert und in die Gasphase, die eine einzigartige Reinraumumgebung darstellt, transferiert. Die nun von ihrer ursprünglichen Umgebung isolierten Moleküle sind frei von intermolekularen Wechselwirkungen. Dies erlaubt eine detaillierte Untersuchung ihrer intrinsischen Struktureigenschaften. Anschließend werden die Biomoleküle nach ihrem Masse-zu-Ladungs-Verhältnis selektiert und können von suprafluiden Heliumtröpfchen aufgenommen werden. Die eingebetteten Ionen werden nun auf die Gleichgewichtstemperatur des Tröpfchens von ~ 0.37 K abgekühlt, wodurch ihre interne Energie – und somit die Anzahl der besetzten Quantenzustände – verringert wird. Mithilfe des IR Freie-Elektronen-Lasers des Fritz-Haber-Instituts können schließlich charakteristische Molekülschwingungen untersucht werden, die Rückschlüsse auf das lokale Netzwerk von Wasserstoffbrückenbindungen zulassen.

Zwar wurden die Eigenschaften einer Vielzahl von Molekülen bereits in der sub-Kelvin-Umgebung von suprafluiden Heliumtröpfchen erforscht, allerdings war bis dato unklar, ob sich dieser experimentelle Ansatz auch auf Biomoleküle übertragen lässt. Die in dieser Arbeit vorgestellten experimentellen Ergebnisse zeigen jedoch eindeutig, dass sich diese Methode zur Strukturuntersuchung großer, intakter Biomoleküle eignet. Unter den präsentierten Ergebnissen befindet sich das erste Schwingungsspektrum des protonierten Pentapeptids Leu-Enkephalin das mit der Heliumtröpfchen-Methode aufgenommen wurde. Die hochaufgelösten experimentellen Spektren stimmen gut mit theoretischen Berechnungen überein. Weiterhin konnte durch die hervorragende Übereinstimmung mit literaturbekannten Daten die schwache Wechselwirkung der Heliumtröpfchen bestätigt werden.

Standardtechniken der Massenspektrometrie ermöglichen es, molekulare Ionen in der Gasphase als Funktion ihres Ladungszustands zu untersuchen und so die Auswirkungen

des Zusammenspiels von Coulomb-Abstoßung und Wasserstoffbrückenbindungen auf die Sekundärstruktur der Zielmoleküle zu erforschen. Zu diesem Zweck wurden Infrarotspektren der in Heliumtröpfchen eingebetteten Proteine Ubiquitin und Cytochrom c aufgenommen. Die experimentellen Ergebnisse lassen sich als Coulomb-induzierter Übergang aus einer hauptsächlich helikalen in eine gestreckte Sekundärstruktur interpretieren, welche durch C_5-Wasserstoffbrückenbindungen gekennzeichnet ist. Diese Deutung wird durch ein simples elektrostatisches Modell sowie durch quantenmechanische Berechnungen an Modellpeptiden unterstützt. Dieser Übergang der Sekundärstruktur ist aller Voraussicht nach für isolierte Proteine – wie sie in der Massenspektrometrie auftreten – allgemeingültig.

Des Weiteren wird durch das Dotieren mit positiv geladenen Ionen ermöglicht die intrinsischen Eigenschaften der Heliumtröpfchen direkt zu untersuchen. Ein grundlegendes Merkmal von Heliumtröpfchen ist ihre einzigartige Fähigkeit, Moleküle durch Kollisionen aufzunehmen. Um einen genaueren Einblick in diesen Prozess zu erlangen, wurden Beschleunigungsexperimente der geladenen ionendotierten Heliumtröpfchen durchgeführt, wobei diese in Abhängigkeit der Masse und Größe der eingebetteten Ionen detektiert werden. Eine systematische Untersuchung der Aufnahmewahrscheinlichkeit zeigt die Existenz einer vom Dotanden abhängigen Mindestgröße der Tröpfchen, unterhalb derer die Aufnahme des Moleküls ausbleibt. Anhand dieser Beobachtungen werden verschiedene Hypothesen sowie theoretische Modelle vorgeschlagen und diskutiert, um die Einschränkungen und Grenzen dieses Aufnahmeprozesses weiter zu beleuchten.

Contents

1 Introduction

Gaining complete knowledge over the structural properties of biological molecules has become an active field of research. An enormous effort is made in trying to understand and even predict biomolecular structure. This interest is based on the fact that the structure and the function of biological molecules are closely related. Biomolecular structure is primarily studied using X-ray crystallography and nuclear magnetic resonance (NMR) as well as infrared (IR) spectroscopy [1]. These methods facilitate the investigation of the three-dimensional fold of proteins, their interactions with their surroundings as well as other properties of the structure and dynamics of biological molecules in solution- and solid-state. However, the investigation of biological molecules in their native environment presents several difficulties. A delicate balance between intra- and intermolecular hydrogen-bonding forces and hydrophobic interactions often results in a large variety of different conformations of the same molecule. Additionally, these conformations typically are in a dynamic equilibrium, *i.e.* they can interconvert, which makes the investigation of a single species particularly challenging. However, it is possible to isolate the species of interest in a clean environment, free from intermolecular interactions: the gas phase.

The investigation of biomolecular ions in the gas phase has been made possible by the recent development of soft ionisation techniques such as electrospay ionisation (ESI) [2, 3], matrix-assisted laser desorption/ionisation (MALDI) [4] and fast-atom bombardment (FAB) [5]. As a result, a vast variety of mass spectrometry based methods have emerged aiming to shed more light on the properties and dynamics of biomolecular structures. Ion mobility-mass spectrometric techniques [6–8], as well as isotopic labelling techniques such as Hydrogen/Deuterium (H/D) exchange [9–11], for example, have proven to be extremely successful at determining the overall structure of biomolecular ions. However, they lack sensitivity for a more detailed chemical information about the local hydrogen bonding patterns. This gap can be filled with gas-phase infrared spectroscopic techniques that allow to directly determine the structural details by probing specific vibrational modes without unwanted interferences from the environment [12–14].

To date, two main experimental approaches have been available for the investigation of molecular vibrational modes in the gas phase: the infrared multiple photon dissociation (*IR-MPD*) technique and the *messenger* technique. Both techniques are based on the dissociation of a molecule or molecular complex after absorption of infrared radiation. The vibrational excitations of large molecular systems and clusters have been mainly investigated using the *IR-MPD* method [14]. This technique is based on the dissociation of strongly bound species

1

such as covalent bonds within molecules and has proven to be highly suited to identify the structural details of biomolecular ions. However, it requires the absorption of multiple IR photons, thus leading to highly excited molecules. As a consequence, the interpretation of the vibrational spectra obtained using this method can be complicated by broadening and shifts in the position of absorption bands [12–14]. This problem can be overcome by monitoring the fragmentation yield of a weakly bound complex as in the messenger technique. In this experimental method, the molecule of interest is tagged with a small molecule or rare gas atom that can be detached after absorption of only few or even a single infrared photon. Thus, the obtained vibrational spectrum closely resembles that of a linear absorption spectrum, which greatly facilitates its assignment. However, the previously mentioned soft ionisation techniques used to efficiently generate biomolecular ions are not well suited for the formation of weakly bound species. As a result, only small complexes of true biological interest have been studied so far using this technique [15, 16].
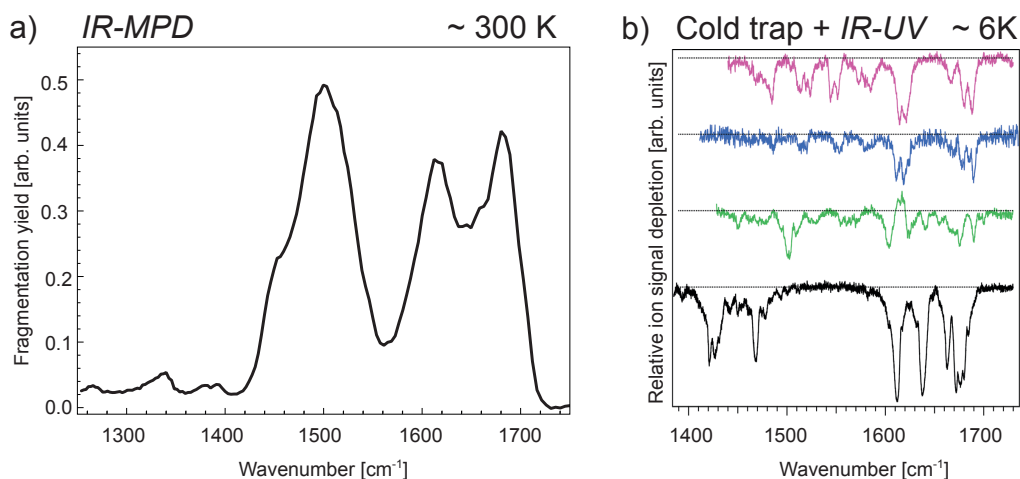
Figure 1.1: Panel (a) shows the IR spectrum of the peptide gramicidin S measured at room temperature using the *IR-MPD* technique (adapted from Ref. [17]). Panel (b) shows the IR spectra of four different conformers obtained using the IR-UV ion dip technique in combination with a cryogenic ion trap (adapted from Ref. [18]) Reducing the temperature from ~ 300 K [17] to ~ 6 K [18] results in a smaller number of quantum states with significant occupation probabilities, thus reducing spectral congestion and facilitating the interpretation of the experimental results.

Cryogenic multipole ion traps [19, 20] have evolved as a powerful extension of these gas-phase techniques to investigate molecular ions at low temperatures [21–24]. Reducing the internal temperature of a molecule has a dramatic impact on the IR spectrum, as shown in Figure 1.1. The vibrational spectrum of the decapeptide gramicidin S measured at room temperature using the *IR-MPD* technique [17] is shown in panel (a). Three main absorption bands can be observed in the wavenumber range 1400 cm^{-1} and 1720 cm^{-1}. Figure 1.1 (b)

shows the vibrational spectra of four different conformers of the same peptide. However, in this case, the species of interest were accumulated in an ion trap kept at a temperature of ~ 6 K [18], thereby lowering the internal energy of the trapped ions. This drastically reduces the number of populated quantum states. Consequently, the spectral congestion is greatly reduced and sharp absorption lines are obtained, thus simplifying the spectral assignment process. Cryogenic multipole ion traps are usually combined with various spectroscopic schemes. Currently, the most commonly employed (double resonance) scheme for the study of cold biomolecular ions is based on ultraviolet (UV) photodissociation probing and IR pumping, the so-called IR-UV ion dip technique [21, 25]. This method has provided highly resolved infrared spectra of conformer-selected biomolecular ions, reflecting the intensities of the vibrational transitions with great accuracy [26]. However, it is limited by the requirement of a UV chromophore, which is not present in many molecules of interest.

Superfluid helium nano droplets have emerged as an alternative approach to study molecular structures at sub-Kelvin temperatures [27–30]. In this method, the species of interest are embedded inside clusters consisting of $\sim 10^3$ to up to $\sim 10^{10}$ helium atoms. Although particles embedded in helium droplets are not isolated from their environment, the virtually non-interacting nature of superfluid helium yields infrared spectra that reproduce the gas-phase data with great accuracy [27, 31]. Moreover, helium droplets have a very low equilibrium temperature (~ 0.37 K) and lack absorption bands from the far IR to the deep UV. The combination of these properties makes superfluid helium the ideal matrix for isolation of particles at cryogenic temperatures.

Although superfluid helium droplets have been extensively used to investigate the vibrational modes of a wide variety of molecules, the study of biomolecular structure using this technique is still in its infancy. Typically, molecules investigated using helium clusters are brought into the gas phase *via* laser evaporation or sublimation in a heated cell. The high temperatures required to heat the samples in these processes are incompatible with the fragile nature of most large biological molecules, and often lead to their fragmentation or denaturation. An alternative solution is to ionise the species of interest using soft ionisation techniques such as electrospray ionisation. An experimental approach combining electrospray ionisation with matrix isolation in helium droplets was recently demonstrated [32, 33]. Using this method, intact biomolecular ions as large as complete proteins have been successfully incorporated inside helium clusters [32]. In this thesis, this experimental apparatus was further developed in order to obtain the first infrared spectra of large biomolecular ions embedded in helium droplets. It is demonstrated that the internal degrees of freedom of the embedded systems are efficiently cooled by the helium environment while barely affecting the structure of the target species. Moreover, the experimental results show that helium droplets can be combined with intense light sources such as free electron lasers to determine the structural details of large biological molecules without the issues present in other experimental approaches like, for example, the need for a UV chromophore.

Another advantage of using positively charged ions in combination with helium clusters is

the possibility to investigate the intrinsic properties of helium droplets in a simple fashion. Due to the presence of an electrical charge, the ion-doped droplets can be easily manipulated as well as directly detected. In this work, one of the fundamental characteristics of helium droplets, the ability to pick up impurities *via* mechanical impact, was investigated making use of standard mass selection techniques. Moreover, using positively charged ions as probes paves the way to further investigate many other aspects of helium droplets that are still unclear such as solvation dynamics, binding energies between solvent and helium environment, as well as the process by which an ion is ejected from a droplet upon absorption of multiple IR or UV ions [33–36].

Outline of the Thesis

The main focus of this thesis is the study of the secondary structure of biomolecular ions at the cryogenic temperatures provided by helium droplets, as well as the investigation of the intrinsic properties of superfluid helium. The key aspects required to achieve these goals are introduced and motivated in Chapter 2.

A new experimental setup was developed in order to make use of the advantages of cooling biomolecular ions to sub-Kelvin temperatures and interrogate them using infrared radiation. This apparatus is described in detail, discussed, and characterised in Chapter 3.

Chapter 4 focuses on the properties of the pick-up process. Acceleration experiments were performed that allowed to systematically investigate the pick-up probability as a function of dopant size and mass. The results are compared to the different theoretical models in order to rationalise the limitations and constraints of this process.

The combination of helium droplets and gas-phase infrared spectroscopy resulted into the first vibrational spectrum of the protonated pentapeptide leucine enkephalin measured at sub-Kelvin temperatures. The results are presented in Chapter 5, showing highly resolved vibrational spectra with sharp bands in excellent agreement with the calculations as well as with the available gas-phase data [25]. Moreover, the effect of charge solvation was further investigated by complexing leucine enkephalin with an 18-crown-6 molecule. The high resolution of the vibrational spectra allowed for an assignment of a preferred low energy conformation.

As the size of the species of interest increases so does the complexity of their infrared spectra. Chapter 6 presents the first vibrational spectra of two different proteins, ubiquitin and cytochrome c, in the cold environment provided by superfluid helium droplets. The structural evolution of these proteins as a function of charge state is discussed by comparing the experimental results with two simple models in terms of Coulomb energy and position of the absorption bands.

2 Concepts

The focus of this work is the IR spectroscopic investigation of positively charged peptides and proteins embedded inside helium droplets making use of the free electron laser facility available at the Fritz Haber Institute. In this chapter, a brief introduction to biological molecules is given in Section 2.1. An overview of the properties of superfluid helium in general, and of helium nano droplets in particular, can be found in Section 2.2. The basics of vibrational spectroscopy and some of the different techniques employed to investigate the vibrational modes of different molecules are discussed in Section 2.3. Finally, Section 2.4 motivates the specific combination of infrared spectroscopy and helium droplets in order to investigate biological molecules.

2.1 Biological Molecules

2.1.1 From Individual Atoms to Proteins

All living organisms are composed of biological molecules with a distinct chemical composition, shape, and function. The vast majority of biological molecules can be classified into four major groups: lipids, nucleic acids, carbohydrates, and proteins. The building blocks of proteins are a set of 22 different monomer units called amino acids. An amino acid, as schematically illustrated in Figure 2.1, is a compound that contains an amino and a carboxyl group, and a distinctive side chain labeled the R-group. Depending on their stereochemistry, amino acids can be found in L- and D-configuration. Most naturally occurring proteins contain exclusively L-amino acids.
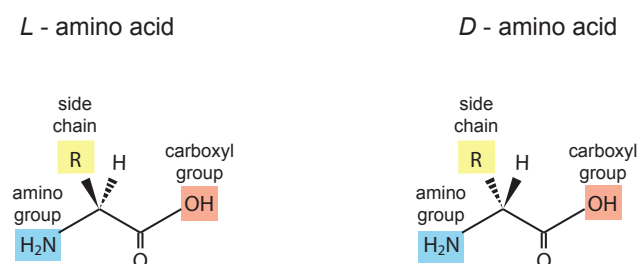
Figure 2.1: Schematic representation of amino acids in the L- and D- configuration.
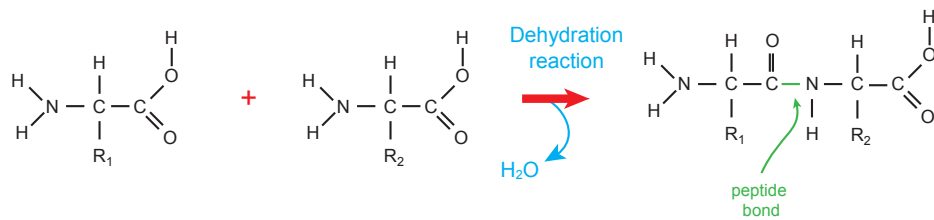
Figure 2.2: The linking of the amino group of one amino acid to the carboxyl group of another amino acid leads to the formation of a peptide bond. This process is accompanied by the loss of a water molecule.

The amino group of one amino acid can link to the carboxyl group of another amino acid to form a so-called peptide bond. As depicted in Figure 2.2, this reaction is accompanied by the loss of a water molecule and the remaining part of each amino acid involved in this reaction is called an amino acid *residue*. A series of amino acids joined by peptide bonds form a polypeptide chain. The repeating part of the chain consists of covalently bound atoms and is called the *main chain* or *backbone* of the protein. The variable part is referred to as the *side chain*. The number of amino acids in the polypeptide chain is used to label it as a peptide or a protein, with proteins containing more than 50 building blocks. By convention, the amino group is taken to be at the left side of the chain (*N*- terminal) and the carboxyl group at the right side (*C*- terminal).

2.1.2 Protein Structure

In 1953, Frederick Sanger determined the complete amino acid sequence of a protein, insulin, in a benchmark experiment [37]. Since then, the sequence of more than 100 000 proteins has been studied and determined, demonstrating the remarkable fact that each protein has a unique sequence of amino acids.

The complete protein structure can be characterised by primary, secondary, tertiary, and quaternary structure. The knowledge of the identity of a protein requires the detailed knowledge of its sequence of amino acid residues, also known as the *primary structure*. The atoms of a polypeptide chain can arrange in localised regions of a protein into distinct structures, such as helices, pleated sheets, and turns. This general three dimensional arrangement of the backbone conformation is called the *secondary structure*. The overall three dimensional shape of the polypeptide chain is called the *tertiary structure*, and is believed to be crucial in the determination of the function of the protein. Most proteins consist of several polypeptide chains, linked to each other through non-covalent bonds. The three dimensional arrangement of multiple protein monomers is the *quaternary structure*.

The diverse range of functions that proteins can take in cellular life depends on the protein three-dimensional structure, which is determined by its chemical composition and environment.
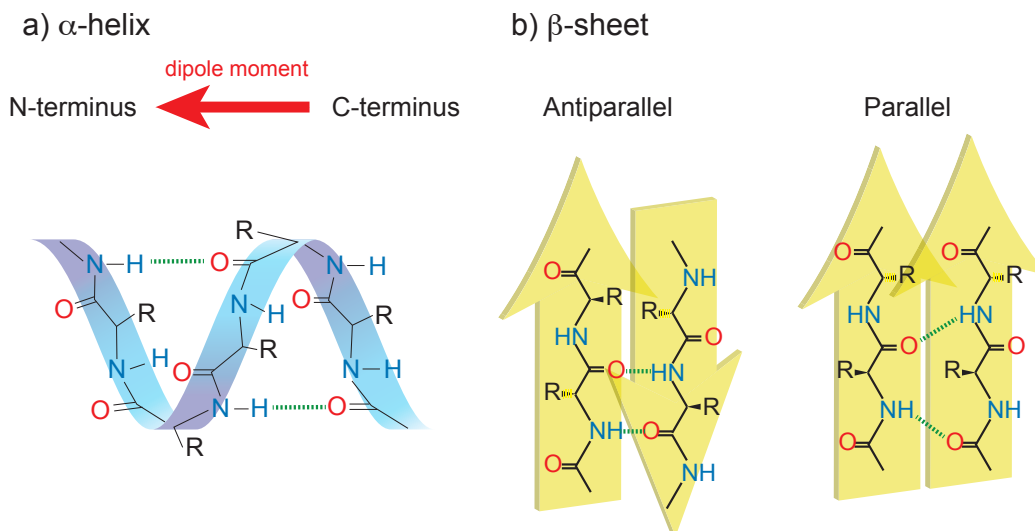
Figure 2.3: Schematic representation of an α-helix (a) and a β-sheet (b).

In order to predict the three dimensional structure of a protein, understanding the role each amino acid plays in the final fold is essential. Therefore, the investigation of the secondary structure of proteins is a crucial intermediate step in order to understand their function.

Secondary Structure

The three dimensional arrangement of neighbouring amino acid residues can form periodic structures, giving rise to three main elements: helices, β-sheets, and turns.

In 1951, the α-helix was proposed by Pauling and Corey [38] as one of the periodic structures of polypeptide chains. Six years later it was confirmed for the first time in a crystal structure of myoglobin (a 153 residue protein of ≈ 17 kDa of mass) by X-ray diffraction. This kind of secondary structure (see Figure 2.3 (a)) exhibits a spiral conformation, with a coiled backbone where each N−H group coordinates with a hydrogen to the C=O group of the amino acid four residues earlier ($i+4 \rightarrow$ i). Hence, all the C=O and N−H groups of the backbone are hydrogen bonded except for the amino acid residues at the end of the helix. Although α-helices are the most common kind of helices, other forms are also possible such as the 3_{10}- and π-helices, where the N−H group acts as a hydrogen bond donor to the C=O group three ($i+3 \rightarrow$ i) and five ($i+5 \rightarrow$ i) residues earlier, respectively. For *L*-amino acids and, thus, for proteins, helices are coiled in a clockwise manner, with all R groups pointing outward. Helices are usually less than 45 Å long (~ 30 amino acid residues) and have a dipole moment pointing from the C- to the N-terminus.

The β-pleated sheet or β-sheet has also been proposed in 1951 by Pauling and Corey [39]. It consists of extended polypeptide chains with neighbouring chains running in opposite (antiparallel) or the same (parallel) direction (see Figure 2.3(b)), the so-called β-strands.

Hydrogen bonds between adjacent polypeptide chains can form, since the C=O group of a residue is adjacent and in the same plane as the N−H group of the residue in the neighbouring β-strand. Depending on whether the arrangement is parallel or antiparallel, the hydrogen bonds point in a perpendicular or a diagonal direction to the chain, respectively.

In a compact, globular shape, as preferred by most proteins, the direction of the polypeptide chain must be often reversed. This is achieved by the so-called turns. Of particular importance is the β-turn, in which the C=O group of a residue i is hydrogen bonded to the N−H group of a residue $i+3$.

The secondary structure of proteins can be probed, for example, by means of infrared (IR) spectroscopy (see Section 2.3). Exciting molecular vibrations by the absorption of IR light provides information about the presence or absence of specific functional groups. Particularly interesting are the vibrations that can be excited in the so-called *fingerprint* region (~ 400 cm^{-1} to ~ 2000 cm^{-1}). In this region, each compound produces a different pattern of absorption bands. However, the large number of oscillators that can be excited in this region can lead to broad absorption bands that frequently overlap, thus hindering the interpretation of the spectrum. One way to overcome this problem is to reduce the density of populated states by drastically reducing the temperature of the compound. This is achieved, for example, by embedding the molecules in superfluid helium nano droplets.

2.2 Helium Droplets

Since 1954, chemical species have been investigated using the so-called matrix isolation technique [40, 41]. In this experimental technique, sample molecules are trapped within an unreactive matrix, usually an inert gas at low temperature. In principle, any substance that can be frozen can be used as a matrix to isolate a certain particle. However, solid noble gases are usually employed as host materials due to their weak interaction with the guest particles.

The study of impurities solvated in liquid helium droplets was developed in the early 1990's by Scheidemann *et al.* [42] as an elegant way to use liquid helium for matrix isolation while overcoming the intrinsic difficulties encountered when using bulk helium (discussed later in this chapter). Indeed, the demonstration of the pick-up of neutral neon atoms in helium clusters [42] opened the door to the investigation of atoms and molecules in one of the most amazing elements in nature.

2.2.1 Why Helium Droplets?

Helium is the second most abundant element after hydrogen and can be found in the form of two isotopes, ^{4}He and ^{3}He. Helium shows the remarkable property of remaining liquid at absolute zero temperature and ambient pressure due to the high zero point energy and its weakly interacting nature. Instead of solidifying, ^{4}He undergoes a unique phase transition to a superfluid state called He II at a temperature of $T = 2.17$ K. In contrast, the ^{3}He isotope

does not show a superfluid behaviour until a much lower temperature ($T = 2.6$ mK) and will not be further addressed in the remainder of this work. Superfluidity was first observed by Pyotr Kapitza (in Moscow), and independently by John F. Allen and Don Misener (in Cambridge, UK) in 1937. It has played a crucial role in the field of low temperature physics due to the dominance of quantum effects ever since. One of the most characteristic properties of superfluid helium is the vanishingly small viscosity experienced by impurities travelling below a certain critical velocity. In addition to being only weakly interacting, superfluid helium has a very high heat conductivity and does not absorb light from the deep infrared to the far ultraviolet.

At low temperature the thermal wavelength associated to a helium atom is comparable to the He−He interatomic distance. As a result, superfluid helium shows a quantum rather than classical behaviour, thus displaying the most bizarre effects. For example, just a month after the discovery of superfluidity in helium was reported [43, 44] scientist accidentally came across another quantum effect, the helium fountain [45]. There, it was observed that superfluid helium could flow into a heated tube through a porous plug that would be too small for the normal fluid to pass. Superfluid helium has also been observed to crawl up the walls and out of an open container [46], and to form quantised vortices in order to conserve angular momentum. The idea of quantised circulation in helium was first discussed by Lars Onsager in 1946 at Yale University and further developed by Richard Feynman in 1955. The first experimental evidence of quantised vortices in helium came from the work by Vinen *et al.* [47, 48]. Although the quantum mechanic effects present in bulk helium have been widely studied, many of them are still a matter of debate in finite helium droplets. For example, the presence of a critical velocity, the so-called *Landau velocity*, under which no friction is present has been confirmed experimentally only recently in helium droplets [49] after years of debate [50–52]. Moreover, only recently has the formation of quantised vortices been demonstrated as well in helium nano droplets by Vilesov *et al.* with the observation of characteristic Bragg patterns from xenon clusters trapped in the vortex cores [53].

While the reasons mentioned above encourage the use of helium for matrix isolation, the actual process of doping and investigating impurities in bulk helium has proven to be very challenging. Seeding the matrix in a controlled manner has been shown to lead to an unavoidable aggregation of dopants. This is due to the typically weaker interactions between helium and the doped impurity than between the impurities themselves. Furthermore, dopants also exhibit a rather strong interaction with the containing vessel walls. As a result, the seeded impurity precipitates towards the wall of the vessel instead of remaining solvated in the bulk helium.

These issues can be circumvented by using finite superfluid nano droplets as a matrix instead of bulk helium. Superfluid helium droplets typically consist of between $\sim 10^3$ to up to $\sim 10^{10}$ helium atoms. In the form of ideal nano cryostats, they offer the possibility of combining the mentioned advantages of helium without the issues presented by bulk helium. In the last decades, helium droplets have been systematically used to incorporate and study a

wide variety of dopants, from small molecules [54] and alkali metals [55] to C_{60} [56] buckyballs and proteins [32].

2.2.2 Properties of Helium Droplets

Due to the extraordinarily weak van der Waals interactions between the atoms (< 1 µeV [57]), helium is known to have the lowest boiling point of all substances (4.2 K for ^{4}He at atmospheric pressure) [58] and it remains liquid to a temperature of 2.17 K. It was first liquefied by Kamerlingh Onnes in 1908. However, further cooling in an attempt to produce solid ^{4}He at a reduced pressure proved to be completely unsuccessful as a result of the remarkable absence of a triple point. Although several properties were discovered over the next 30 years, such as the specific heat maximum at 2.17 K, it was not until 1938 that the nature of He II was recognised to be a manifestation of superfluidity [43, 44]. There, it was experimentally confirmed that no measurable resistance to the flow of He II through small capillaries exist. However, later that year the demonstration of the existence of a viscous drag with a viscosity coefficient similar to that of helium gas [59] led to the formulation of the two fluid model proposed by Tisza and Landau.

The Two Fluid Model

Figure 2.4 (a) schematically illustrates the heat capacity of helium as a function of temperature. Cooling down liquid helium below a temperature of 2.17 K results in a phase transition from the normal fluid He I into the superfluid He II, the so-called λ-transition. This phase transition is believed to be directly related to Bose-Einstein condensation. In order to describe many macroscopic thermodynamic and hydrodynamic properties of He II, the so-called "two-fluid model" was developed. This model was first suggested by Tisza [60] and further developed by Landau [61]. In the two-fluid model, the flow of He II can be conceptually described by assuming a mixture of two fluids: the superfluid and the normal fluid component. The superfluid component carries no viscosity nor entropy. In contrast, the normal fluid component carries all viscosity η and entropy S. The mass density of bulk helium (ρ_{bulk}) can be described in terms of the operators of the mass density of the superfluid (ρ_s) and the normal (ρ_n) component as

$$\rho_{\text{bulk}} = \rho_s + \rho_n. \tag{2.1}$$

Following the properties of Bose-Einstein condensates, many of the particles are in the ground state while the remainder occupy excited states. At a temperature of 0 K, the normal fluid fraction (ρ_n/ρ_{bulk}) is non-existent, and it increases with rising temperature until it becomes the only available component at 2.17 K.

The two different flows described in the model require the assignment of individual velocities **v** to each component. Therefore, the mass-flux density **j** can be expressed as
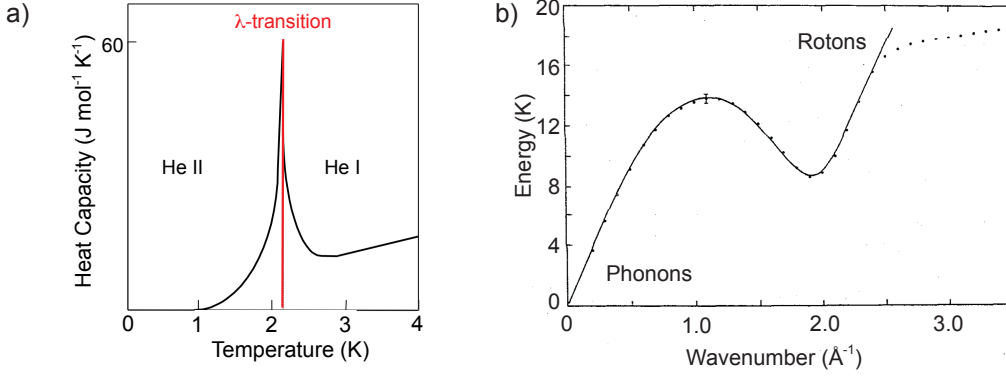
Figure 2.4: a) The specific heat capacity of liquid ^{4}He displays an abnormal behaviour at 2.17 K, the so called λ-transition. There, a phase transition between normal fluid (He I) and superfluid (He II) takes place. The graph is adapted from Ref. [62]. b) Dispersion curve of bulk He II at a temperature of 1.1 K and under its saturated vapour pressure, adapted from Ref. [63].

$$\mathbf{j} = \rho_{\mathbf{s}}\mathbf{v_s} + \rho_{\mathbf{n}}\mathbf{v_n}. \tag{2.2}$$

In addition, the flow of the superfluid fraction is believed to be free of turbulence and thus rotation is not allowed. Therefore,

$$\nabla \times \mathbf{v_s} = \mathbf{0}. \tag{2.3}$$

It was not until 1946 that the validity of the two-fluid model was experimentally demonstrated by Andronikashvili [64]. There, the viscosity of helium was determined using a stack of oscillating discs immersed in liquid ^{4}He and measuring the period of the oscillator as a function of temperature. The distance between the discs was small enough for the normal fluid to become coupled to the discs and thus contribute to the moment of inertia. However, the superfluid component remains uncoupled to the system. The results showed that, above the λ-point, the period of the oscillator is nearly independent of temperature. However, for temperatures below 2.17 K the frequency of the oscillator increases rapidly as the fraction of normal fluid decreases. The experimental results are in agreement with the two-fluid model and indicate that the superfluid fraction increases sharply below the $\lambda-$point. This experiment provided the evidence necessary to establish the two-fluid model of superfluidity.

Elementary Excitations and Critical Velocity

Landau predicted that superfluidity arises in helium by the impossibility of the superfluid flow to generate elementary excitations. The dispersion curve of the vibrational excitations of liquid helium was first measured in 1960 by Henshaw and Woods [65] using inelastic neutron scattering.

As depicted in Figure 2.4 (b), the dispersion curve has two regions, the *phonon* and the

roton region. Phonons are low energy excitations that occur in crystals as well as in superfluid helium. The phonon region is governed by long wavelength excitations with a small momentum p. The energy ϵ of a phonon is a linear function of its momentum and obeys $\epsilon = c \cdot p$, where c is the velocity of sound. Rotons are higher-energy excitations that are unique to helium and their properties are still under study. The excitation of rotons is attributed to the local minimum (p_0) in the dispersion curve with a corresponding energy Δ present in the dispersion curve at a wavenumber of ~ 1.9 Å^{-1}. The energy of rotons follows the form $\epsilon = \Delta + (p - p_0)^2$.

Also included in Landau's theory [61] is the prediction of the lack of viscosity or energy dissipation for small velocities of the flow of liquid helium at absolute zero through a capillary. This comes as a result of the peculiar shape of the dispersion curve and leads to a critical velocity $v_L \sim \Delta/p_0 \sim 58$ m s^{-1} [66]. Below this critical velocity v_L, also known as the *Landau velocity*, an object is able to move frictionless through helium since no energy can be dissipated through creation of elementary excitations. The drag remains zero until v_L is reached. After this point, dissipation sets in very abruptly. The critical Landau velocity has been experimentally verified for bulk helium [67] and more recently [49] in helium nano droplets, even for droplets containing as few as ~ 1000 helium atoms. The concept of a critical Landau velocity is crucial for the pick-up of impurities by helium droplets. Otherwise, a particle moving through a purely superfluid droplet for which no energy could be dissipated through elementary excitations independent of the relative velocity with the helium environment, would fly frictionless through the helium medium. As a result, the initial kinetic energy of the impurity could not be dissipated and, therefore, the particle could not be successfully trapped inside the helium droplet.

2.2.3 Pick-up by Helium Droplets

The Pick-up Technique

The pick-up technique was first introduced using argon clusters by Scoles *et al.* [68, 69]. At the beginning it was unclear whether helium clusters could pick-up certain species. However, it soon became evident that helium droplets have the unique ability to pick-up a wide variety of species with which they collide [42] with pick-up cross-sections close to that of their geometrical cross-sections. In most experiments, the species of interest are incorporated into the helium droplets *via* mechanical impact in a gas cell. This widely-employed technique is based on the thermalization of the dopant with the surrounding helium environment, which results in evaporation of helium atoms and thereby removes the internal and collision energy of the dopant. As a result, the species of interest are trapped inside the droplet at the superfluid helium temperature (~ 0.37 K). Once inside the droplets, the captured particles can move freely within the droplet and have been shown to rotate almost freely [70]. Moreover, the sequential pick up of many particles, *e.g.* metal ions, can lead to the formation of large clusters inside helium droplets [71].
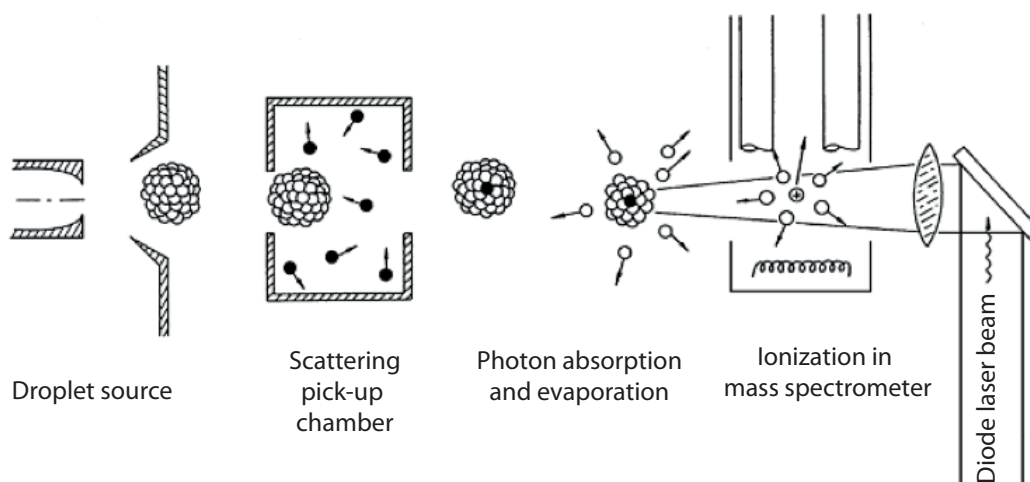
Figure 2.5: Schematic representation of the pick-up chamber typically used for the capture of particles inside helium droplets *via* mechanical impact. Figure adapted from Ref. [72].

Figure 2.5 schematically displays a typical experimental setup used to embed an impurity inside a helium droplet. There, the so-called pick-up chamber is filled with the vapour of the species of interest, where they are captured by the traversing beam of helium droplets. Further downstream, the embedded particle is interrogated in the detection chamber. This versatile technique has been successfully applied to incorporate all kinds of dopants into the droplets, from small molecules [54] and alkali metals [55] to C_{60} buckyballs [56]. However, the requirement of thermal evaporation of the dopant in this particular setup makes the investigation of fragile species such as biological molecules extremely challenging. The high temperatures required in the thermal evaporation technique will lead to the decomposition or the denaturation of most biological molecules. Therefore, a variation of this technique has been developed in the last years in which positively charged molecules are brought into the gas phase *via* electrospray ionisation and accumulated inside a hexapole ion trap [32, 33]. This technique will be discussed in detail in Chapter 3.

Evaporative Cooling

In order to cool down a thermally excited helium droplet, helium atoms can be evaporated from its surface. A statistical description of the density of states of helium clusters for a given excitation energy has been calculated by Brink and Stringari [73]. There, a terminal temperature of 0.4 K was predicted, in excellent agreement with the value of 0.37 K later determined experimentally [70, 74].

Evaporative cooling is an essential mechanism in the pick-up process, since it allows the thermalisation of the dopant with the helium environment. The pick-up process can be rationalised in terms of an inelastic collision, in which the internal energy of the guest particle,

E_{int}, and the collision kinetic energy are transferred to the droplet [42, 75]. Thus, the energy associated with the pick-up is given by:

$$E_{\text{pick-up}} = \frac{1}{2} \frac{m_{\text{dopant}} m_{\text{D}}}{m_{\text{dopant}} + m_{\text{D}}} (\mathbf{v}_{\text{dopant}} - \mathbf{v}_{\text{D}})^2 + E_{\text{int}} \tag{2.4}$$

where m_{dopant} and m_{D} are the masses of the dopant and the droplet, respectively, and v_{dopant} and v_{D} denote the corresponding velocities.

Typically, the velocities of the dopants in the frame of this work are small compared to the velocities of the droplets (~ 50 m s^{-1} *vs.* ~ 500 m s^{-1}). In addition, since $m_{\text{D}} \gg m_{\text{dopant}}$, Equation (4.2) can be simplified to

$$E_{\text{pick-up}} \approx \frac{1}{2} m_{\text{dopant}} v_D^2 + E_{\text{int}}. \tag{2.5}$$

After pick-up has taken place, the energy $E_{\text{pick-up}}$ is dissipated into the helium environment, which results in the release of helium atoms from the droplet surface, therefore re-cooling the remaining droplet. The number of helium atoms released during the thermalisation process can be estimated as ≈ 1600 atoms per 1 eV of the pick-up energy [27]. Consequently, the initial size of the droplet decreases after capturing an impurity and thermalising the system back to ~ 0.37 K.

To date, evaporation of helium atoms due to the dissipation of the internal and collision energy has been considered the main limitation in the pick-up process. As an example, measuring the reduction of the droplet size as a result of thermalisation with a SF$_6$ molecule has provided a limit of ≈ 1000 helium atoms on the minimum size of droplets that can be employed in this particular case [76]. Recently, Chen *et al.* [77] have proposed a correlation between the kinetic energy and the doping efficiency, arising from a finite deceleration rate of the ion inside the droplet. The dissipation of kinetic energy as a purely kinematic constraint on the pick-up of molecular ions by helium droplets will be discussed in detail in Chapter 4.

2.2.4 Ion Ejection from Helium Droplets

Absorption of resonant light by ions doped inside helium droplets can lead to the ejection of the dopant from the droplet [33–36], as schematically depicted in Figure 2.6. Subsequently, the bare ion without helium complexes is detected. Ion ejection is routinely used as a marker for photon absorption in order to obtain IR and ultraviolet (UV) spectra [33–36]. However, the mechanisms involved in this process are not yet clear. In the following, several aspects about the ejection process that have been unveiled during the last years are reviewed.

Gspann and Vollmar were the first to discuss the observation of small, charged helium clusters after electron impact ionisation of large helium droplets [78]. The clusters consisted mainly of He$_2^+$, as was later revealed by the experiments of Toennies *et al.* [79]. Initially it was suggested that a total evaporation of helium atoms, as a consequence of the energy release during the formation of He$_2^+$, would lead to the detection of the bare ion. However, it
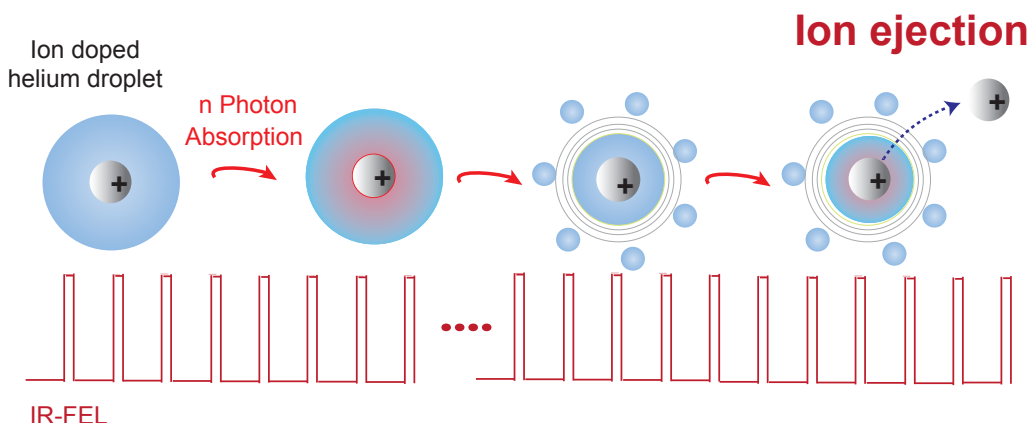
Figure 2.6: Molecules embedded inside helium droplets can absorb resonant photons, resulting in an energy transfer from the dopant into the helium environment. As a consequence, helium atoms are evaporated in order to thermalise the droplet back to the equilibrium temperature of ~ 0.37 K. However, an additional non-statistical process takes place in which the molecule is ejected from the droplet.

was later demonstrated by Janda *et al.* that the fragment distribution is independent of the cluster size, thus indicating an impulsive energy transfer that ejects He_2^+ ions [80].

Such a non-thermal cooling of the excited ion has been *a posteriori* confirmed by several experiments [33, 34, 81, 82]. IR and UV spectroscopic experiments have also provided strong indications suggesting that the detection of the bare ion is not a result of a complete evaporation of helium atoms from the droplet [33, 34]. Considering that every helium atom leaving the droplet takes away its binding energy of ~ 5 cm^{-1} [62], it is evident that the amount of evaporated helium atoms due to the absorption of one photon is much smaller than the typical number of helium atoms used in the helium clusters of most experiments. However, the ejection of the ion generally requires the absorption of multiple photons [33, 35, 83]. Therefore, it could be expected that the process of evaporation of helium atoms repeats itself with each absorbed photon until only the bare ion is left. This process seems unlikely since it would require, for example, the absorption of 20 photons at 382 nm to eject Hemin$^+$ from a droplet with a size of $\sim 10^5$ helium atoms [33]. In contrast, the experimental results indicate that the absorption of only 2 photons suffices to eject the ion from the droplet under the mentioned conditions [33]. Furthermore, as will be discussed in detail in Chapters 5 and 6, while increasing the photon density can lead to the fragmentation of the molecule, reducing the photon density only leads to a decrease of the signal intensity. The ion complexed with helium clusters is in no case observed. On the other hand, it is observed that the number of ions ejected by exciting a particular molecular transition with a fixed photon density correlates with the size of the helium droplets, showing a strongly increased ejection yield

with decreasing droplet size [33, 34].

Whereas the cooling of ions after vibrational or electronic excitations is thought to be governed by a non-thermal process, excited neutrals have shown evidence of following a thermal cooling process [84]. It has been argued that neutrals and ions could have a different cooling process after excitation due to the enlarged solvation shell that surrounds ions as a result of their strong interaction with the helium environment [85–88]. The interaction between helium and a neutral impurity is quite weak and is dominated by dispersion and multipole-induced interactions. The interaction with charged species shows an additional charge-induced dipole interaction, which decreases proportional to r^4. Therefore, the interaction between the charge and the surrounding helium rapidly becomes weaker for large molecules such as the ones investigated in this work. As a consequence, differences in certain characteristics of the ejection mechanisms such as, for example, the ejection yield as a function of droplet size could be expected for ions of different size. However, excellent agreement is observed between the experimental findings about the ejection process of ionised species of very different sizes (see Ref. [35] and Chapters 5 and 6). Such a good agreement between experimental results suggests that the cooling process is independent of the size of the ion. Thus, the role of the charge in the ejection as well as in the cooling mechanism is still unclear. It must also be noted that, to date, an ejection of neutral atoms or molecules following excitation has not been demonstrated. This could be an argument in favour of a different cooling mechanism between neutrals and charged species. However, such an experimental demonstration can be rather challenging due to the intrinsic difficulties related to the detection of neutral species.

Recently, another remarkable property of the ion ejection process has been discovered, namely that the excited species leave the droplets with isotropic angular distributions and very similar speeds of ~ 60 m s^{-1} [49].

Although the experiments performed in the last two decades have helped to elucidate many of the properties and characteristics concerning the ejection of ions from helium droplets, the details of the mechanism still remain elusive.

2.3 Vibrational Spectroscopy

The investigation of the vibrational modes of a peptide or protein can help to elucidate its secondary structure. Additionally, a large number of molecular properties can be unveiled by probing its vibrational excitations, such as the location of the charge, the hydrogen bonding interactions or its symmetry. In the following, the vibrational modes of a molecule and the different techniques available to investigate them *via* infrared spectroscopy will be discussed.

2.3.1 Vibrations in Molecules

Molecular oscillators can vibrate around their rest position with a frequency that depends on the mass and the interatomic binding energy. A molecule with N atoms has $3N-6$ modes

of vibrational motion, $3N-5$ in the case of linear molecules. As a first approximation, the vibrational motion of an oscillator can be described as a periodic harmonic motion using the quantum harmonic oscillator. In this approximation, the potential energy of a particle $V(x)$ displaced by a distance r from its equilibrium position R_e is described as a parabolic function [89, 90]

$$V(x) = \frac{1}{2}k_f(r - R_e)^2,$$ (2.6)

where k_f is the force constant of the bond.

For each harmonic oscillator the vibrational energy $E(x)$ is quantized, showing equally spaced energy levels given by

$$E_v = \left(v + \frac{1}{2}\right)\hbar\omega \qquad \text{with} \qquad \omega = \sqrt{\frac{k_f}{m}}$$ (2.7)

for $v = 0, 1, 2, ...$, where ω is the frequency of oscillation and v the vibrational quantum number and m the mass.

Equation 2.7 shows that the vibrational levels are equally separated by energy quanta $\hbar\omega$. The energy separation between molecular vibrational levels is in the IR range. As a consequence, the absorption of a resonant IR photon can lead to the excitation of the molecule to a particular vibrational level, provided that such a motion is accompanied by a change in the dipole moment.

It is important to note that, although the harmonic oscillator is a good first approximation, it does not rigorously describe the potential energy of the vibrational modes of most molecules, since real chemical bonds have an intrinsic anharmonic nature. This anharmonic character of the oscillator potential has several consequences as the energy levels are no longer equally spaced. Furthermore, the vibrational modes are no longer independent and can couple to each other.

IR spectra can be obtained by measuring the absorption of light by a solid, liquid, or gaseous sample. These are the so-called *absorption* spectroscopic techniques. They are based on the Beert Lambert Law, that relates the absorption of light by a material to the properties of the material through which the light is travelling. Typically, the intensity of the radiation is measured before and after the propagation through the sample, $I_0(\nu)$ and $I(\nu)$, respectively. As a result, the absorption cross section $\sigma(\nu)$ can be obtained from

$$\frac{I(\nu)}{I_0(\nu)} = e^{-\sigma(\nu)\cdot n\cdot l},$$ (2.8)

where n represents the density of absorbing particles and l the path length [91]. A general limitation of this technique is the requirement for a high density of absorbing particles ($\geq 10^{10}$ molecules cm^{-3}) necessary to obtain an absorption spectrum. Such densities are generally not available in a sample of mass-selected molecular ions and a change in the intensity of the radiation is thus not detectable. Therefore, vibrational spectra in the gas

phase are usually obtained employing *action* spectroscopy. This technique is based on the effect of the light on the molecule such as, for example, its fragmentation or ionization.

2.3.2 Infrared Spectroscopy in the Gas Phase

IR spectroscopy in the gas phase has become a well established method to investigate the structure of isolated molecular ions [14, 92]. In the condensed phase, unwanted interferences in certain regions of the spectrum such as a predominant signal of the solvent or buffer, or shifts in the spectral lines due to an interaction with the solvent molecules, are a common problem. However, such interferences are circumvented in the gas phase due to the absence of solvents. In addition, gas-phase experiments offer the possibility of mass-to-charge selection in the case of ions.

One of the most common strategies employed to obtain the vibrational spectrum of a gas-phase molecule is the measurement of its fragmentation yield as a consequence of the energy deposited in the molecule after absorption of resonant IR radiation. However, the dissociation threshold of most molecules is usually higher than the typical energy of a single IR photon. Two approaches are available to circumvent this limitation: the investigated system must have a very low dissociation barrier or the laser sources must be powerful enough to make possible the absorption of multiple photons by a single ion. The latter can be achieved using the so-called IR multiple-photon dissociation (*IR-MPD*) spectroscopy [12–14]. It was first demonstrated by Beauchamp *et al.* in 1978 [93] with the dissociation of mass-selected ions using a tunable CO_2 laser and has recently experienced a revived interest with the development of high pulse-energy optical parametric oscillators (OPOs) and IR free electron lasers such as the Free Electron Laser for Infrared eXperiments in Nijmegen (FELIX), the Centre Laser Infrarouge d'Orsay (CLIO) and the Fritz Haber Institute Free Electron Laser (FHI FEL) facilities.

The dissociation mechanism of polyatomic molecules in the *IR-MPD* process is schematically depicted in Figure 2.7 (a). Due to the anharmonic coupling between vibrational modes, the energy gained with the absorption of each photon can be dissipated over the entire molecule *via* intramolecular vibrational redistribution (*IVR*) [94]. Provided the molecule is large enough, the *IVR* mechanism becomes extremely rapid and thus, the molecule is prepared for the absorption of the next photon after a remarkably short time (typically less than 1 ns for aromatic molecules [12]). This process repeats itself until the internal energy of the (highly excited) molecule exceeds the dissociation energy.

The *IR-MPD* process has proven to be extremely versatile for the investigation of large molecules in the gas phase. However, its main drawback is the typical broadening of the vibrational absorption bands due to an increase in the density of states as a function of the internal energy. In addition, the spectral lines are often red-shifted since the normal modes are not completely orthogonal to each other [12]. Hence, the assignment of vibrational modes in IR spectra based on calculated linear absorption spectra is challenging.
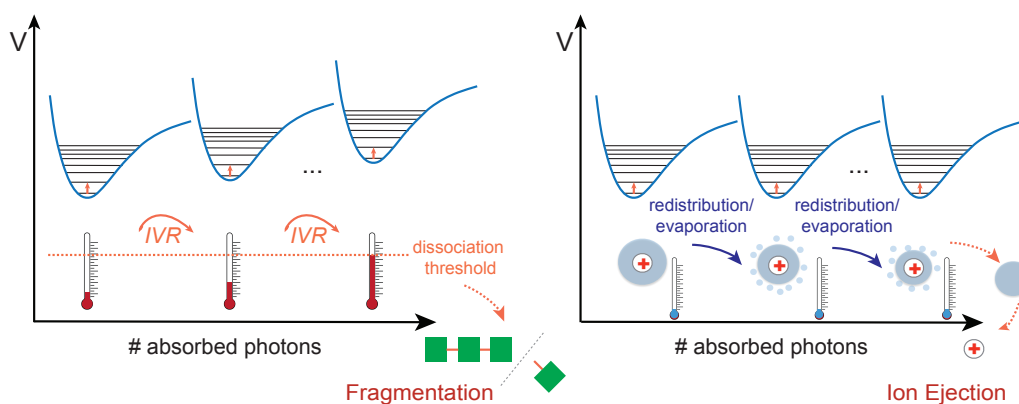
Figure 2.7: (a) In the *IR-MPD* process, the energy pumped into a specific vibrational level is redistributed *via IVR*. Once the internal energy reaches the dissociation threshold the molecule can undergo unimolecular dissociation. In contrast, the excitation of a molecule embedded in a helium droplet (b) is dissipated into the helium bath, therefore, the molecule relaxes back into the ground state at an ultra low temperature. Further photons can be absorbed until the molecule is eventually ejected from the droplet.

Another common strategy is the so-called *messenger technique*, where a weakly bound atom is detached upon absorption of a single or very few photons. Since its development by Lee and co-workers in the 1980s [95] this experimental method has been widely used to obtain IR spectra of ionic species, mainly relatively small systems [22, 96–98]. The low binding energy of the messenger, usually rare gas atoms, is crucial for the dissociation upon absorption of a very low number of photons as well as for ensuring that the structure of the investigated molecule remains virtually unaffected. Since detachment of the messenger can occur after absorption of a single IR photon, the resulting spectrum resembles closely a linear absorption spectrum and a potential broadening of the vibrational absorption bands can be significantly reduced.

One drawback of the messenger technique, particularly in the context of this work, is its limited applicability for the study of biological molecules. Supersonic expansions are usually necessary to directly bind the rare gas atom to the species of interest. However, due to their intrinsically fragile nature, biological molecules require a gentle transfer into the gas phase, typically achieved using electrospray ionisation or matrix-assisted laser desorption/ionization techniques, which usually do not favour the formation of weakly bound clusters. This limitation can be easily circumvented by accumulating the ions of interest inside cold ion traps [24, 99]. Particularly relevant in the field of biological molecular ions is the single-photon spectroscopic scheme in which a single UV photon is employed to induce dissociation, the IR-UV ion dip

technique. This spectroscopic technique is often used in combination with cold ion traps [21], and has proven to be one of the most powerful double-resonance methods for conformational assignment. In this experimental approach, an IR pulse is fired prior to a UV pulse, thus depleting the ground state population of the parent molecule whenever the IR frequency is resonant with a vibrational transition. As a result, a dip is measured in the subsequent UV spectrum [21]. This technique offers the possibility to investigate the vibrational modes of conformer-selected biological molecules at low temperatures (see Figure 1.1), yielding resolved spectra that enable a clear assignment of the vibrational bands. However, this technique can only be applied to biological molecules containing a UV chromophore.

2.4 Infrared Spectroscopy in Helium Droplets

Although, strictly speaking, molecules embedded in helium droplets are not "isolated", this technique is emerging as a good alternative to investigate biological molecules at very low temperatures in a very weakly interacting matrix.

In the 1990s, Goyal *et al.* obtained the first IR spectrum of a molecule (SF_6) embedded in liquid helium clusters [28]. Comparison with earlier studies that employed heavier rare gas complexes to embed SF_6 [68, 100, 101] quickly showed that embedding the guest particles in helium clusters yields much sharper vibrational bands. Since then, the popularity of helium droplets as a spectroscopic matrix has gradually increased until being considered "ideal nano-cryostats" [31, 102, 103]. Several reasons have contributed to this title; first, helium is completely transparent to photons with energies below 20 eV, which makes it a particularly useful matrix for spectroscopic studies since no active modes are present from the far IR to the deep UV. Second, helium droplets offer the possibility to study atoms and molecules at very low temperatures since they are isothermal at 0.37 K [70, 73]. Hence, the number of quantum states of the embedded molecule with a significant occupation probability is drastically reduced. Consequently, the spectrum appears less congested showing sharp lines that simplify the spectral assignment process. Third, the virtually non-interacting helium bath leads to perturbations so weak that the IR spectra of neutral [27] as well as ionised molecules [34, 35] embedded in helium droplets can be directly compared to the theory for the corresponding isolated system.

During the last decades, the structure and properties of neutral molecules have been widely investigated by means of helium nanodroplet spectroscopy [105–107]. This technique has demonstrated to be a powerful tool as well for the investigation of neutral biological molecules [28–30]. It was mentioned in the previous section that one of the challenges encountered when working with biological molecules is their characteristic fragile nature. Neutral species investigated using helium clusters are commonly brought into the gas phase *via* laser evaporation or are sublimated in a heated cell. However, these techniques tend to heat the sample to very high temperatures, often resulting in their fragmentation. One way to overcome this problem is to ionise the biological molecule of interest using soft ionisation
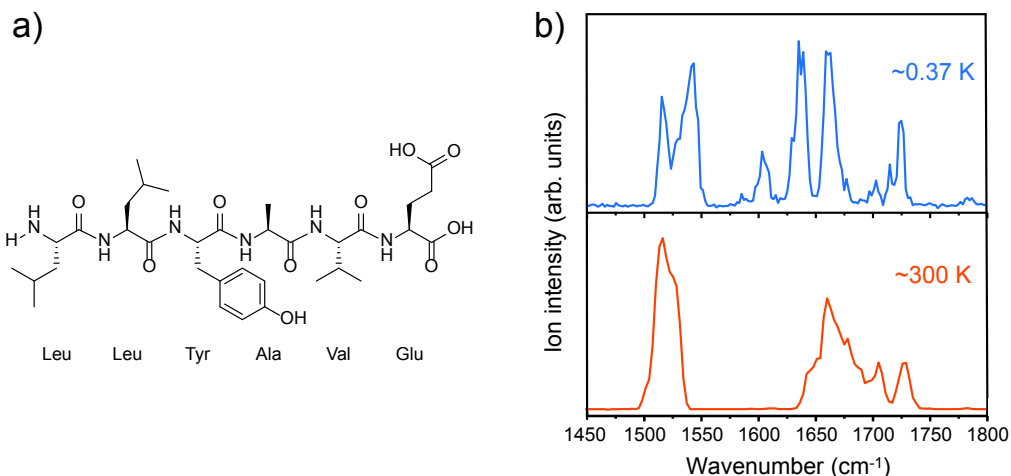
Figure 2.8: a) Schematic representation of the hexapeptide Leu-Leu-Tyr-Ala-Val-Glu. b) The IR spectra of the hexapeptide Leu-Leu-Tyr-Ala-Val-Glu measured using the *IR-MPD* technique at room temperature [104] (lower panel) and helium droplets (upper panel). Reducing the temperature from ~ 300 K to ~ 0.37 K results into a much more resolved spectrum with sharp transitions and a line width similar to the bandwidth of the laser.

techniques such as electrospray ionisation.

Figure 2.8 (b) shows the infrared spectrum of the positively charged hexapeptide Leu-Leu-Tyr-Ala-Val-Glu (schematically represented in Figure 2.8 (a)) measured at room temperature using the *IR-MPD* technique [104] (red, lower panel) and using helium droplets (blue, upper panel). Cooling down the molecule to temperatures of ~ 0.37 K results in a much richer spectrum, with sharp transitions that could otherwise not be resolved. In contrast to the *IR-MPD* technique, the energy gained by the absorption of multiple photons can be dissipated in the helium bath instead of being redistributed over the entire molecule. As a consequence, the spectrum obtained is believed to correspond to the excitation of the molecular excitations from the ground state. This process is schematically depicted in Figure 2.7 (b). Furthermore, as it will be discussed in detail in Chapter 5, using helium nano droplets as a spectroscopic matrix yields spectra comparable to those of gas-phase isolated ions measured in a cryogenic trap, with the advantage that no UV chromophore or messenger atom is needed.

3 Experimental Methods

This chapter describes in detail the characteristics of the two different experimental setups employed in this work. The chapter is divided as follows: the fundamental idea of the experiment and an overview of the instrumental setup are discussed in Section 3.1. A description of the modified *Q-TOF Ultima* apparatus and its components, as well as the theoretical background of RF multipole devices can be found in Section 3.2. The details of the ion trap, developed in the frame of this thesis, where ions are picked up by a traversing beam of helium droplets is discussed in Section 3.3. Helium droplets are produced by a pulsed, cryogenic Even-Lavie valve as discussed in Section 3.4. The ion-doped helium droplets have been investigated using a Faraday cup and a Daly detector, presented in Section 3.5. The free electron laser facility at the Fritz-Haber-Institut is described in Section 3.6. Finally, the trigger system used in typical experiments and the devices used to detect the bare ion after photo excitation are presented in Section 3.7.

3.1 Overview

Figures 3.1 and 3.2 schematically depict the two different experimental setups that have been used during this thesis in order to investigate biological molecules in the gas phase at sub-Kelvin temperatures. Both experimental setups are based on the same fundamental idea. Ions are brought into the gas phase using an electrospray ionisation source (ESI). After being m/z-selected by a quadrupole mass filter, the ions are accumulated inside a hexapole ion trap for several seconds. After the trap is sufficiently filled, the ions are picked up by a pulsed beam of helium droplets that crosses the trap along the main axis and subsequently cooled down to an equilibrium temperature of ~ 0.37 K *via* evaporation of helium atoms. Further downstream, the ion-doped droplets are detected using two different kinds of detectors: a Faraday cup or a Daly-type detector. The cold molecules can then be probed by means of optical spectroscopy. Upon resonant absorption of multiple photons, an ion embedded inside a droplet can be ejected. Subsequently, the ejected ion is detected using a linear time-of-flight (*TOF*) mass spectrometer. Vibrational spectra are obtained by monitoring the ion ejection as a function of wavelength.

Initially, experiments were performed with the machine schematically depicted in Figure 3.1. This experimental setup is described in detail elsewhere [108]. As a part of this thesis, a new experimental apparatus was developed and made fully operational (see Figure 3.2). Although both setups share the same fundamental idea, the new experimental apparatus presents several
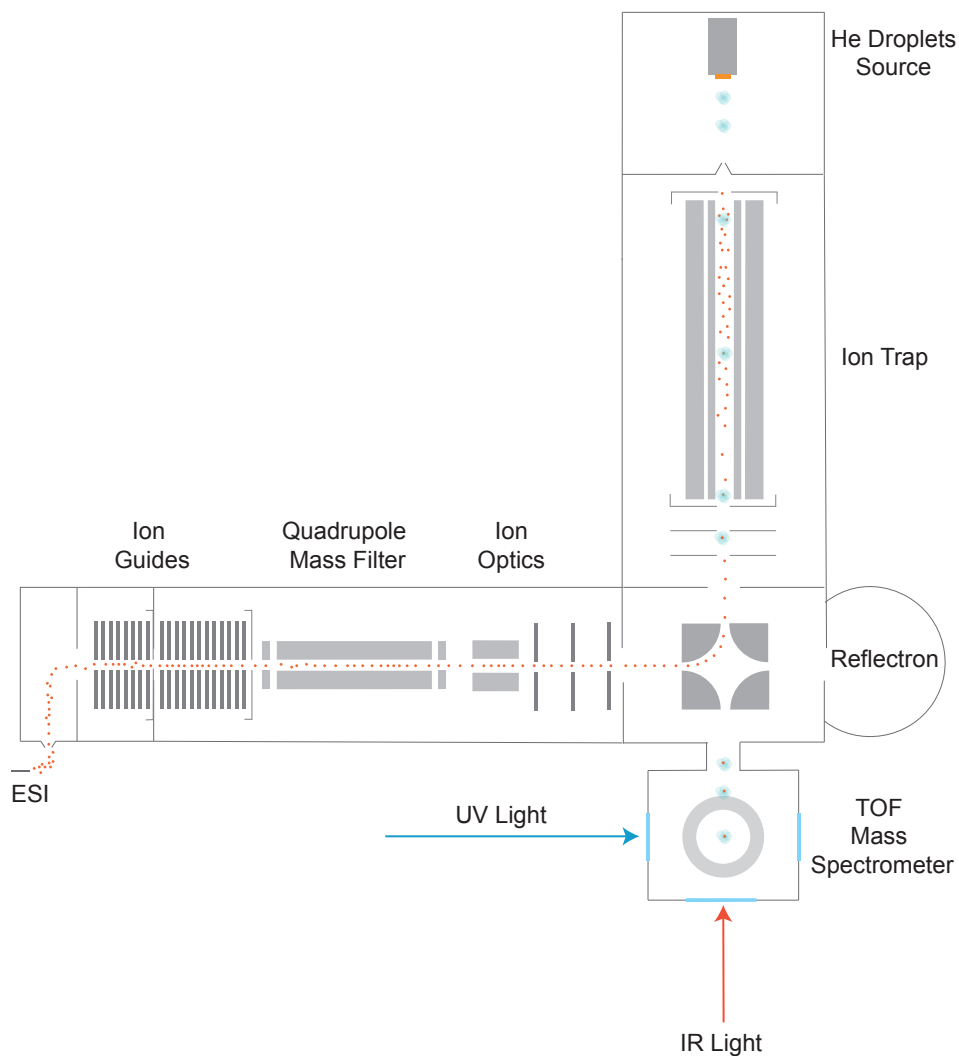
Figure 3.1: Scheme of the initial experimental setup: Ions are brought into the gas phase *via* electrospray ionisation, *m/z*-selected by a quadrupole mass filter and accumulated inside a hexapole ion trap. The ions are picked up by the traversing pulsed beam of helium droplets. The ions leave the hexapole trap embedded inside the helium droplets, where they are cooled down to ≈ 0.37 K *via* evaporative cooling and further investigated in the detection chamber. A detailed description of this machine can be found in Ref. [108].
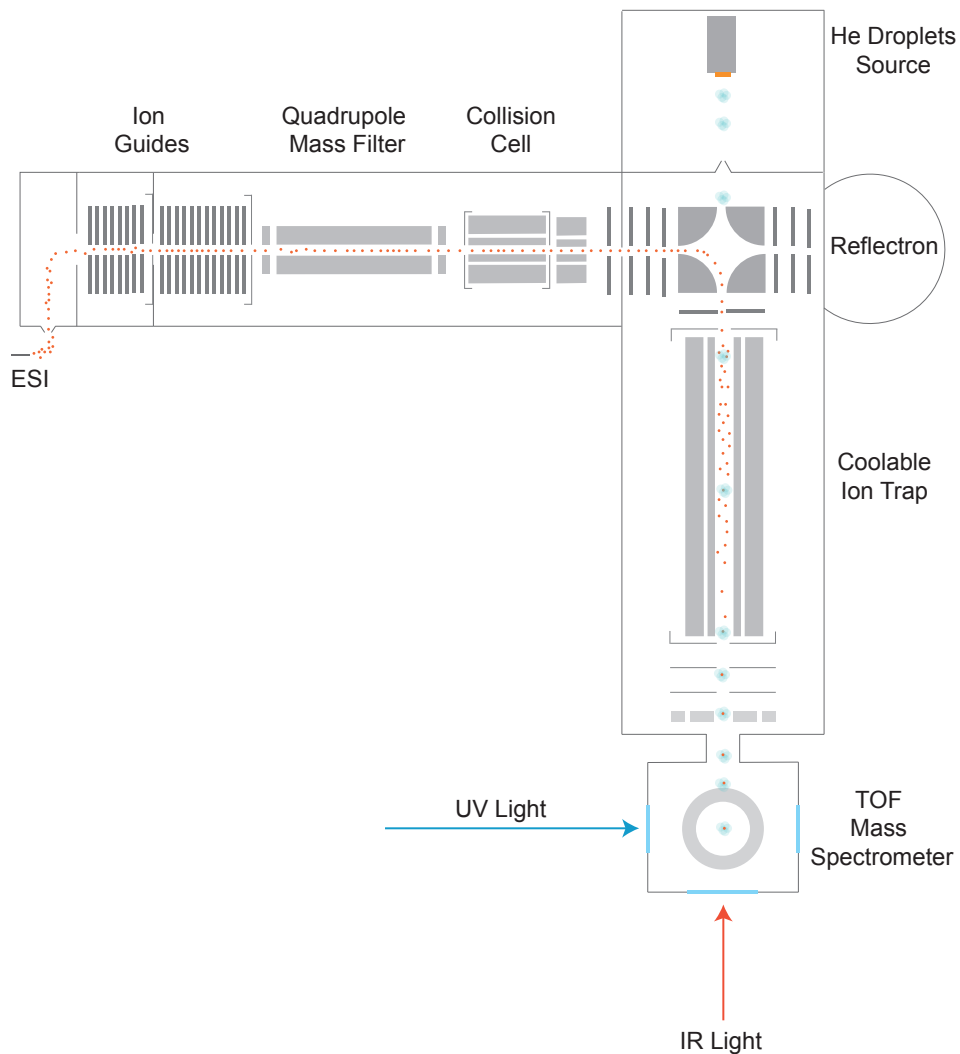
Figure 3.2: Scheme of the experimental setup developed during this thesis. The fundamental idea is shared with the setup shown in Figure 3.1. However, replacing the ion optics present between the quadrupole mass filter and the bender in Figure 3.1 with a collision cell (in the commercial *Q-TOF* originally installed), and, in addition, exchanging the position of the bender and the ion trap greatly improved the ion transmission.

Table 3.1: Base and typical pressures (in mbar) in the experimental apparatus. Pressures during operation are obtained when the Even-Lavie valve is operated at a repetition rate of 10 Hz, stagnation pressure of ~ 65 bar and opening time of 19.1 μs at different temperatures (T_{Nozzle}). The typical pressure of the previous doping chamber is included for comparison.

| Vacuum Stage	Base Pressure	$T_{\text{Nozzle}} = 25\,\text{K}$	$T_{\text{Nozzle}} = 19\,\text{K}$	$T_{\text{Nozzle}} = 15\,\text{K}$
Ion Source Chamber I	$1.4 \cdot 10^0$	$1.4 \cdot 10^1$	$1.4 \cdot 10^1$	$1.4 \cdot 10^1$
Ion Source Chamber II	$3.8 \cdot 10^{-1}$	$1.7 \cdot 10^0$	$1.7 \cdot 10^0$	$1.7 \cdot 10^0$
Quadrupole Chamber	$8.5 \cdot 10^{-7}$	$3.6 \cdot 10^{-6}$	$3.6 \cdot 10^{-6}$	$3.6 \cdot 10^{-6}$
Reflectron Chamber	$2.2 \cdot 10^{-7}$	$2.2 \cdot 10^{-7}$	$2.2 \cdot 10^{-7}$	$2.2 \cdot 10^{-7}$
He droplets Chamber	$7.4 \cdot 10^{-8}$	$5.4 \cdot 10^{-6}$	$9.0 \cdot 10^{-6}$	$1.1 \cdot 10^{-5}$
Old Doping Chamber	$7.2 \cdot 10^{-7}$	$2.4 \cdot 10^{-7}$	$2.4 \cdot 10^{-7}$	$2.4 \cdot 10^{-7}$
New Doping Chamber	$2.0 \cdot 10^{-8}$	$1.0 \cdot 10^{-7}$	$1.0 \cdot 10^{-7}$	$1.0 \cdot 10^{-7}$
Detection Chamber	$2.5 \cdot 10^{-8}$	$1.9 \cdot 10^{-8}$	$1.9 \cdot 10^{-8}$	$1.9 \cdot 10^{-8}$

important modifications, described in the following.

Particular effort was made to improve the overall vacuum inside the instrument. The new experimental apparatus consists of seven differentially pumped regions. The ESI source typically operates at ambient pressures while the first two regions containing the two ion guides are usually kept in the mbar regime. The rest of the apparatus, on the other hand, requires high vacuum conditions ($\leq 10^{-6}$ mbar). Table 3.1 summarises the typical pressures of the apparatus under the specified experimental conditions. Particularly important is the improvement in the vacuum level of the so-called doping region: the chamber where the ion trap is located and the species of interest are incorporated inside the helium droplets. Previously, the ion trap was placed inside an aluminum chamber [108] with a typical pressure of $\sim 10^{-7}$ mbar. This has been replaced by a stainless steel chamber, thereby improving the vacuum level to pressures of $\sim 10^{-8}$ mbar. As a result, the previously observed, unfavourable formation of ion-water clusters was completely suppressed as can be seen exemplarily in the TOF mass spectra of protonated leonine enkephalin $[\text{Leu-Enk+H}]^+$ peptide ions in Figure 3.3.

The ion transmission has been considerably improved. Previously, after passing through the quadrupole mass filter, ions were guided into a quadrupole bender using a stack of lenses and various ion optics [108]. This has been replaced by the (in the commercial *Q-TOF* setup originally installed) collision cell described in detail in Section 3.2.2. The ion transmission was thereby increased by more than one order of magnitude.

In addition, a new ion trap was designed and built in the course of this work, featuring a copper housing that can be cooled with liquid nitrogen. This allows the accumulated ions to be thermalised to temperatures of down to ~ 80 K prior to the pick-up by helium droplets. The details of this device are discussed in detail in Section 3.3.

The remainder of this chapter is restricted to the description of the newly developed experimental apparatus as schematically depicted in Figure 3.2.
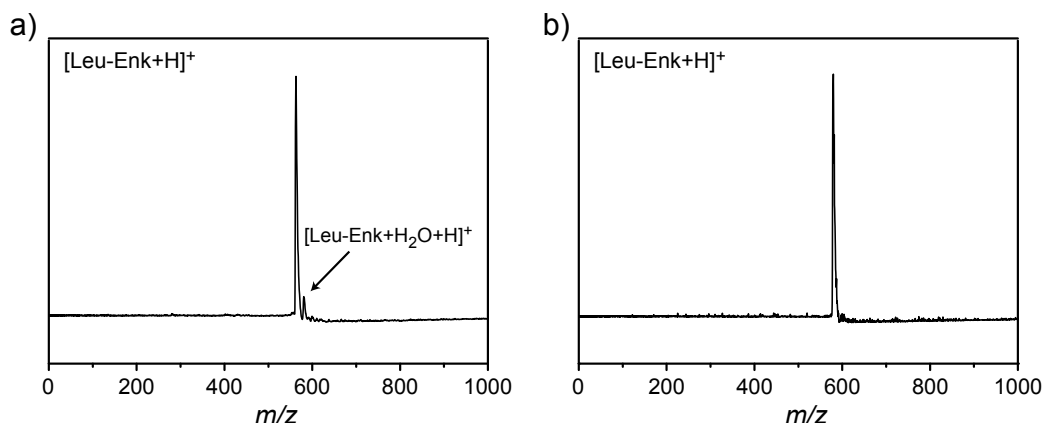
Figure 3.3: TOF mass spectra of ejected ions after photo excitation of droplets doped with [Leu-Enk+H]$^+$ peptide ions. A water adduct, [Leu-Enk+H$_2$O+H]$^+$ can be observed in the TOF mass spectra obtained with the previous experimental setup (see panel a)). The formation of water adducts is suppressed below the noise level using the current experimental setup (see panel b)).

3.2 The Modified Q-TOF Ultima

A modified *Q-TOF Ultima* (Waters Corporation, Manchester, UK) has been employed as the front end part of the experimental setup. This section of the instrument allows the production and *m/z*- selection of molecular ions. Further downstream, the ions can be investigated using a high resolution reflectron time-of-flight mass analyser. Alternatively, the ions can be stored inside a hexapole ion trap for further investigation using superfluid helium droplets.

3.2.1 Ion Production

Electrospray Ionisation

Electrospray ionisation is a standard ionisation technique used in mass spectrometry to transfer molecules from solution into the gas phase. It was pioneered by Malcolm Dole in 1968 and further refined by John B. Fenn in the late 1980s to be applicable to larger molecules of biological relevance. The capability of producing non-volatile and weakly bound species in the gas phase without fragmentation [2, 3] makes this soft ionisation technique particularly useful. In this work, ESI has been applied to study biomolecular cations in the gas phase.

The ESI process is schematically illustrated in Figure 3.4. A solution containing the analyte molecules is pumped into a capillary where a high voltage is applied with respect to a counter electrode (depicted as a skimmer in Figure 3.4). The polarity of this voltage determines the polarity of the ions. In the present case, a positive voltage is applied in order to study positively charged ions. The electric field that is created between the capillary and the skimmer is strongest at the capillary's tip, where it slightly penetrates into the liquid. As
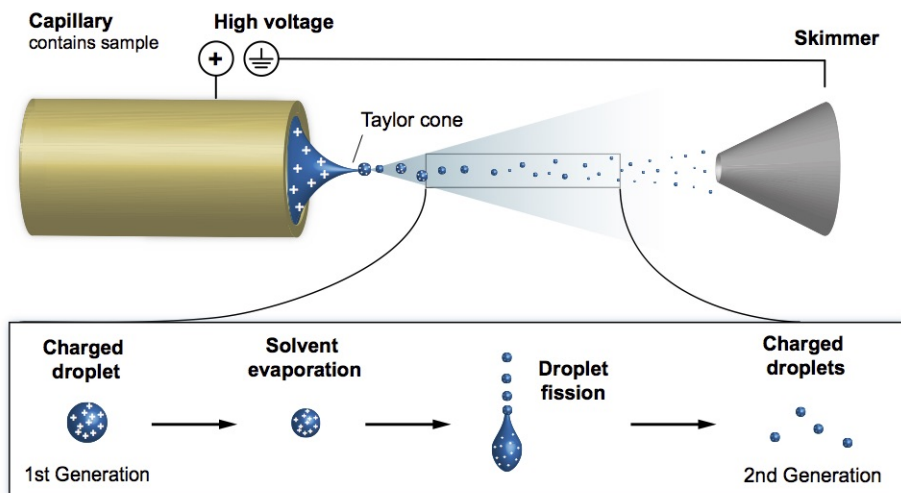
Figure 3.4: Schematic representation of the electrospray ionisation process. A high electric field at the tip of the capillary leads to separation of charges inside the solvent and to the formation of the Taylor cone. The cone can break up into small solvent droplets containing analyte ions. On the way towards the instrument inlet (skimmer), the solvent evaporates and many droplet fission events finally lead to the desolvated molecular ions.

a result, the solvent becomes polarised and the meniscus at the opening of the capillary is deformed into the shape of a cone, the so-called Taylor cone. Charged droplets form when the electric field exceeds a certain critical voltage given by [109]

$$E_0 = \sqrt{\frac{2\gamma\cos(49°)}{\epsilon_0 r_c}}, \tag{3.1}$$

where γ is the surface tension of the solvent, r_c the radius of the capillary, and ϵ_0 the vacuum permittivity. The droplets decrease further in size due to solvent evaporation and break down into even smaller charged droplets, once the maximum density of charges inside the droplet is reached at the so-called Rayleigh limit. This process can repeat itself, reducing the size of the charged droplet with each subsequent droplet generation until a nano-sized droplet containing only one single ion is eventually obtained.

Z-Spray

Figure 3.5 shows a schematic drawing of the commercial Z-spray source originally installed on the *Q-TOF Ultima MS* machine. The dissolved sample (1, Figure 3.5) is pumped through a stainless steel capillary of ∼100 µm diameter at a constant flow rate of 5 µl/min controlled using a syringe pump. A high voltage (∼ 3 kV) is applied to the capillary (2, Figure 3.5) leading to the formation of charged droplets. The subsequent evaporation of the solvent is further facilitated by the nebulizer and the heated desolvation gas (typically both N_2) sprayed
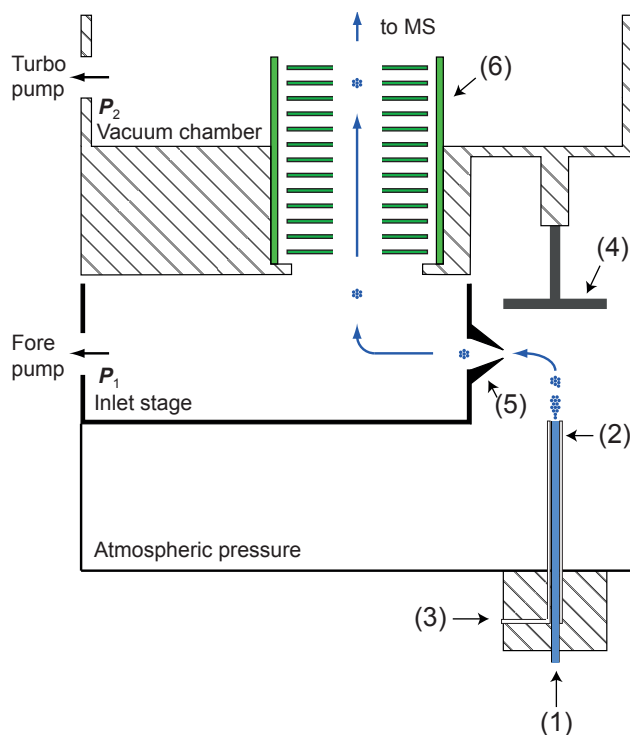
Figure 3.5: Schematic view of the Z-spray source (adapted from Ref [110]). Individual components are: (1) dissolved sample, (2) stainless steel capillary, (3) nebuliser gas (N_2), (4) grounded counter electrode, (5) skimmer, (6) ion guide.

at typical flow rates of ≈ 50 l/h and ≈ 150 l/h, respectively (3, Figure 3.5). While the neutral molecules hit the counter electrode placed in front of the capillary (4, Figure 3.5), the ions are deflected by 90° towards the skimmer (5, Figure 3.5) and into the first pressure stage with a typical pressure of $P_1 \approx 14$ mbar. Subsequently, the ions are deflected by 90° into the ion guide (6, Figure 3.5), located in the second pressure stage ($P_2 \approx 1.7$ mbar).

3.2.2 Multipole RF Devices

The investigation of molecular ions in the gas phase requires capabilities to manipulate the ion's motion. Under high vacuum conditions and at defined ion energies, this can be done with high accuracy using static electric fields. However, static ion optics become inefficient when the pressure is increased, *i.e.*, when collisions with background gas molecules lead to slow ions. Additionally, ions cannot be trapped with static electric fields because global electric potential minima do not exist in the case of static potentials [111]. Instead, the electric fields that are produced by radiofrequency (RF) alternating, electric potentials of so-called multipole RF devices can be used for guiding and trapping of ions even at elevated pressures [19]. The setup makes use of several multipole RF devices in order to guide, m/z-select, and accumulate ions. In the following section the basic operating principle of such devices is discussed, followed by a detailed description of the specific ion guides, quadrupole mass filter, and hexapole ion trap used in this work.

Operating Principles

Multipole RF devices usually consist of $2n$ parallel, cylindrical electrodes symmetrically arranged on a circle with a radius r_0. The electric potential inside the multipole arrangement is given by Laplace's equation [111]

$$\Delta\Phi = 0. \tag{3.2}$$

The electric potential Φ is best described using polar coordinates (r, ϕ) due to the symmetry of most $2n$ multipole devices. The z-dependence is neglected, assuming infinitely long electrodes. Thus, the solution to Equation 3.2 can be expressed as [19]

$$\Phi(r, \phi) = \Phi_0 \left(\frac{r}{r_0}\right)^n \cos(n\phi), \tag{3.3}$$

with boundary conditions

$$\Phi(r = r_0, \phi) = \Phi_0 \cos(n\phi) \qquad \text{and} \qquad \Phi(r = 0, \phi) = 0. \tag{3.4}$$

The electric potential Φ_0 that is applied to the electrodes rapidly reverses its polarity in a periodic manner. It can generally be described as a superposition of a DC component U and an AC component V that oscillates with a frequency $\Omega = 2\pi f$:

$$\Phi_0 = U + V\cos(\Omega t) \tag{3.5}$$

The motion of a charged particle inside such an oscillatory potential can only be described analytically in the case of the quadrupole electrode arrangement. This is briefly discussed at the end of this section. A general description of the particle's motion inside multipole electric potentials can be given within the so-called *adiabatic approximation* proposed by D. Gerlich [19]. In this approximation, the ion moves inside a static, conservative, *effective potential* $V^*(r)$ given as

$$V^*(r) = \frac{n^2}{4}\frac{q^2}{m\Omega^2}\frac{V^2}{r_0^2}\left(\frac{r}{r_0}\right)^{2n-2} + qU\left(\frac{r}{r_0}\right)^n \cos(n\phi), \tag{3.6}$$

where q is the total charge of the ion and m is the ion's mass.

In the adiabatic picture, the total ion energy is a constant of the motion of the ion. Thus, its kinetic energy can be transferred into effective potential energy (or electrostatic potential energy) in a permanent exchange. An ion that enters the multipole at a distance r from the centre experiences a potential energy of $V^*(r)$. The ion will be pushed towards the field minimum localised at the centre of the multipole at $r = 0$. Since the kinetic and the potential energy are being constantly exchanged, the ion starts to oscillate around $r = 0$ perpendicular to the multipole axis. In the adiabatic approximation, the ion will not hit an electrode as long as it does not gain energy from the field, for example by moving too close

to the electrodes. However, if the ion already enters the multipole with a certain transverse energy E_t, its trajectory will become unstable and eventually hit an electrode provided E_t exceeds the effective potential at the surface of the electrode ($r = r_0$).

The stability of the ion trajectory can be described in terms of a stability parameter η, also known as adiabaticity parameter, which is given as

$$\eta(r) = 2n(n-1)\frac{qV}{m\Omega^2 r_0^2}\left(\frac{r}{r_0}\right)^{n-2}.\tag{3.7}$$

The trajectory of the ions is considered stable when the following conditions are met [19]:

$$\eta\left(\frac{r}{r_0} = 0.8\right) \leq 0.3\tag{3.8}$$

and

$$V^*\left(\frac{r}{r_0} = 0.8\right) \geq E_t.\tag{3.9}$$

In order to ensure a successful ion transmission, these stability criteria have to be taken into account when the geometry and operating conditions of RF devices are chosen. From Equation 3.8 the maximum transverse energy E_m of the ion for a given amplitude V of the oscillating potential can be obtained [20]:

$$E_m = \frac{1}{8}qV\eta\frac{n}{n-1}\left(\frac{r}{r_0}\right).\tag{3.10}$$

Furthermore, from Equation 3.9, the minimum RF amplitude ($V_{\min}$) that is necessary to guide an ion of a certain mass m and transverse energy E_t can be calculated as

$$V_{\min}(m, E_t) = \sqrt{m\frac{4}{n^2}\frac{r_0^2(2\pi f)^2}{(0.8)^{2n-2}}\frac{E_t}{q^2}}.\tag{3.11}$$

The characteristic properties of the ion motion inside an RF electric field can be used to, for example, transmit, m/z-select, or trap ions using different devices. In the remainder of this section, the details of the ion guides, quadrupole mass filter and linear hexapole ion trap used for these purposes are discussed.

Ion transmission

After being brought into the gas phase *via* electrospray ionisation, the ions are guided by two ring-electrode ion guides through two differentially pumped vacuum chambers with background pressures of ~ 14 mbar and ~ 1.7 mbar, respectively. As the ions pass through these first two chambers they undergo multiple collisions with the background gas molecules and are thus thermalised. Upon entering the adjacent high-vacuum region ($\sim 10^{-6}$ mbar), ions are accelerated to a well-defined kinetic energy of ~ 34 eV. Each ring-electrode ion guide is composed of a stack of thin (~ 0.5 mm) ring electrodes, has circular central opening with

a diameter of 5 mm, and a so-called *endcap* with a pinhole of $\sim$ 1.5 mm diameter. The operational principle of such ring-electrode guides is similar to that of regular multipole devices. Neighbouring electrodes carry oscillating electric potentials that are phase shifted by 90° with respect to each other. Therefore, the same potential is applied to every other electrode. The ring ion guides used are operated with a maximal amplitude of $\sim$ 600 V_{pp} at a frequency of 780 KHz and 1.9 MHz, respectively.

After m/z selection (see below), the ions pass through a hexapole collision cell. In principle, the collision cell can be used to induce fragmentation to assist in structural investigation. However, in this work it is used exclusively to guide the ions into the next chamber where they are accumulated inside a hexapole ion trap. The collision cell consists of six electrodes symmetrically arranged in a circle with a radius of $\sim$ 5 mm operated at a frequency of 770 KHz with a maximal amplitude of $\sim$ 600 V_{pp}. In order to maximise ion transmission, two electrostatic lenses are placed at the entrance and the exit of the device. An additional shorter hexapole guide operated at the same frequency and amplitude as the collision cell is installed to increase ion transmission.

Quadrupole Mass Filter

As mentioned earlier, the equation of motion of an ion inside a multipole oscillatory electric field can only be described analytically in the case of a quadrupole, *i.e* a set of four parallel, cylindrical electrodes, where two opposite electrodes carry the same oscillating electrical potential, which is phase shifted by 90° with respect to the potential of the other two electrodes. Here, the ion's motion is described by the well-characterised Mathieu equations [112]. It is found that a difference in DC electrical potential between the two pairs of electrodes leads to a m/z-dependent discrimination of ions. Therefore, such quadrupole devices can be used to effectively filter ions within a narrow m/z range, which allows further investigation on these isolated species.

The quadrupole mass filter employed in the here described experimental setup is operated at a frequency of 880 KHz. The ion transmission is enhanced by short quadrupole segments that are installed at the entrance and the exit of the quadrupole, the so-called *pre-* and *post-* quadrupole filters, respectively. These filters are operated at the same frequency as the quadrupole itself, however, with an additional DC electrical potential bias. Their purpose is to create more homogeneous fields at the edges of the quadrupole mass filter, and to focus the ion beam to improve ion transmission.

3.2.3 Ion Detection

After being m/z-selected by the quadrupole mass filter, the ions can be detected using a reflectron time-of-flight mass analyser. This allows to investigate and optimise the signal of the bare ions produced by the source prior to being accumulated in the ion trap and doped into the helium droplets.
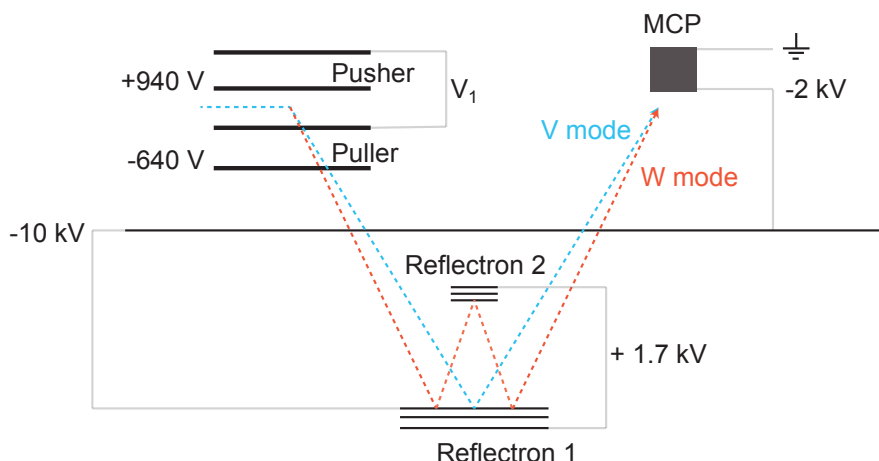
Figure 3.6: Schematic diagram of the reflectron time-of-flight mass analyser used in this work.

The time-of-flight mass spectrometer employed for this purpose is schematically depicted in Figure 3.6. The incoming ions pass through a stack of electrodes labelled as *pusher*, *puller*, and V_1, respectively. Voltages of typically 940 V and -640 V are applied to the *pusher* and *puller* electrodes, respectively. The electrode V_1 is usually kept at ~ 11.5 V. Pusher and puller plates are switched by high-voltage switches (*Behlke*) between the voltage V_1 and 940 V (*pusher*) or -640 V (*puller*), respectively, at a repetition rate of ~ 100 Hz. The mass separation of the ions is achieved using one or the two available reflectrons, which are set to the same potential. Depending on the incident angle determined by the voltage applied to the V_1 electrode, the ions pass through one (*V mode*) or both reflectrons (*W mode*). The two reflectrons are kept at the same potential, usually higher than the flight tube potential of -10 kV. Finally, the ions are detected using a micro channel plate (*MCP*).

3.3 Ion Storage

3.3.1 Hexapole Ion Trap

Inhomogeneous, oscillating electric fields can be used for guiding and trapping of ions as discussed in Section 3.2.2. Multipole ion traps, such as linear hexapoles, are widely applied to store ions over extended periods of time and a detailed review of linear ion traps is given, *e. g.*, by Douglas *et al.* [113].

In this work, the *m/z*-selected ions are accumulated inside the coolable ion trap schematically depicted in Figures 3.7 and 3.8. The device consists of six cylindrical electrodes with a diameter
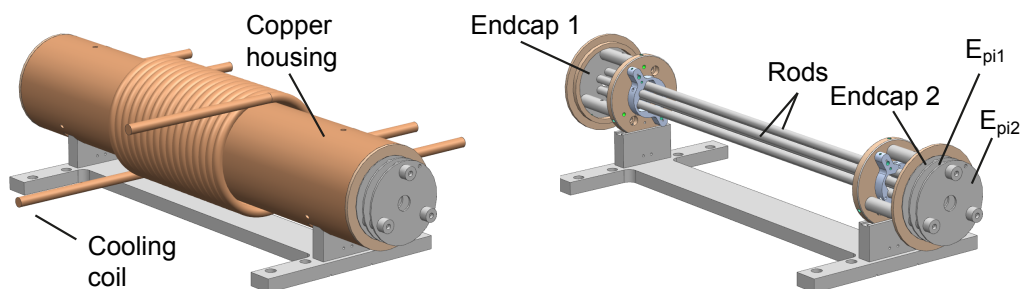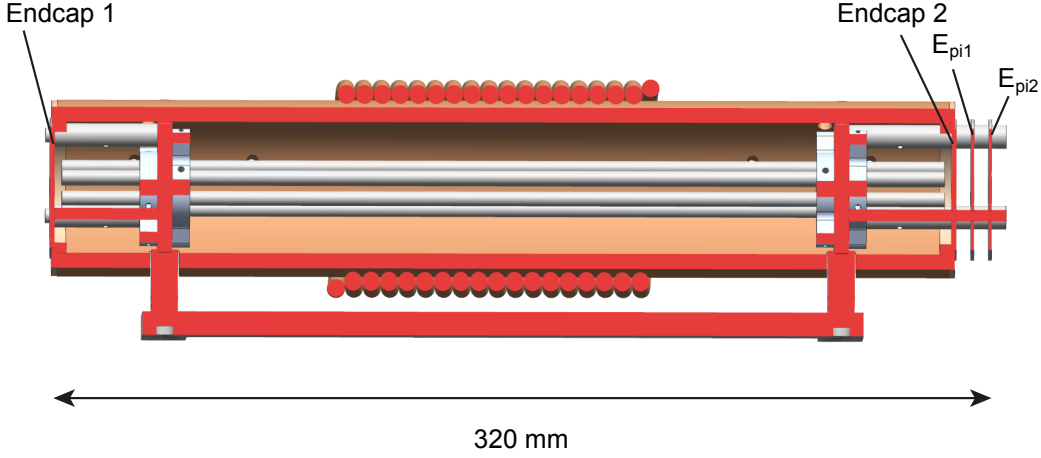
Figure 3.7: Full and sectional view of the ion trap developed in the frame of this work. The hexapole ion trap is placed inside a copper housing that can be refrigerated using liquid nitrogen. In addition to the six electrodes and two endcaps, two further electrodes are placed at the exit of the trap that can be used to accelerate the ion-doped droplets.

of 5 mm placed on a 14.1 mm diameter circle. The length of the electrodes is 300 mm. It is operated at a frequency of 1.1 MHz with an amplitude of $V_{pp} \sim 400$ V provided by an in-house built RF generator. The ions can oscillate around an offset DC voltage (U_{bias}) of ~ 30 V. In order to achieve longitudinal confinement, the electrodes at the entrance and exit of the trap, the so-called endcaps, are kept at a small voltage U_{endcap} over the DC offset of the trap. As a result, the trap depth can be defined as

$$E_{pot} = z \cdot (U_{endcap} - U_{bias}), \tag{3.12}$$

where z represents the total charges $q \cdot e$ of the molecule. Two plates used as ion lenses, (E_{pi1} and E_{pi2}) are installed on the side where the ions exit the trap (see Figures 3.7 and 3.8).

The incoming ions have a well defined kinetic energy of ~ 34 eV. The DC bias of the trap E_{bias} is kept just below this value (~ 30 V). As a result, ions entering the trap have an excess kinetic energy of ~ 4 eV that needs to be reduced to ensure proper trapping by the endcap potentials of $E_{endcap} \approx 33$ V. In order to achieve this, the six electrodes are mounted inside a tube made out of copper that can be filled with a buffer gas through a stainless steel tube with a diameter of 6 mm until a background pressure of $\sim 7.2 \cdot 10^{-6}$ mbar is reached. Typically, ions are accumulated for several seconds. During this time, collisions with the buffer gas (usually helium) remove any excess of kinetic energy and ions are effectively trapped inside the hexapole and endcap potentials. In addition, these ion-neutral collisions thermalise the internal energy of the ions to the temperature of the buffer gas. The exact accumulation time is experimentally determined for each investigated molecule and chosen such that the density of ions in the trap is close to the space charge limit. This is exemplarily shown in Figure 3.9 where the integrated signal of droplets doped with [Leu-Enk+H]$^+$ peptide ions is displayed as a function of the trap loading time of the bare ion, before pick-up occurs. This shows that after ~ 3 seconds, the space-charge limit for this particular ion is achieved. Typical values of the accumulation time can vary from ~ 3 seconds for amino acids and small peptides to up

Figure 3.8: Sectional view of the ion trap.

to ~ 10 seconds for larger proteins, depending on how efficiently the ion of interest can be produced and transmitted. Once the trap is filled with ions, the DC offset voltages of U_{bias} and U_{endcap} are lowered to 0 V and 3 V, respectively. Then, the stored ions are captured by the traversing beam of helium droplets. Due to the high mass and large velocity of the droplets, their kinetic energy (150 - 300 eV) exceeds the trapping potential. Therefore, only ions embedded in helium droplets can leave the ion trap.

An important feature of the ion trap presented here is that all DC voltages can be independently applied in order to manipulate the energies of the ion-doped droplets. As will be discussed in Chapter 4, being able to accelerate the ion-doped droplets beam is crucial to determine their size distributions. This can be achieved by applying an acceleration voltage to the trap bias (U_{bias}) towards a ground potential placed just outside the trap (E_{pi2}).

The ion trap developed in the frame of this work also offers the possibility to cool the confined ions by refrigerating the copper housing with liquid nitrogen. The use of cold, RF ion traps was pioneered by Gerlich *et al.* [19, 20] in the early 1990s in order to study interstellar chemistry. Today, many different forms of cold ion traps are widely used, such as linear 22-pole ion traps [114], cool ring electrode traps [99] or wire-based quadrupole ion traps [115]. In the present experimental setup, we use a flow of liquid nitrogen through a coil-shaped copper tube attached to the copper housing of the trap (Figures 3.7 and 3.8) in order to refrigerate the entire device to temperatures of ~ 80 K. In turn, the collisions between the cold atoms of the helium buffer gas and the accumulated ions thermalise the latter to temperatures of ~ 80 K.
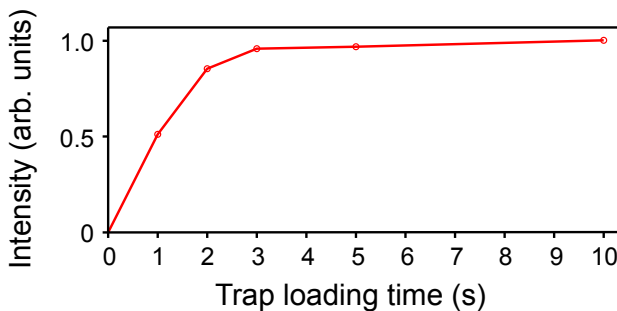
Figure 3.9: Integrated signal of droplets doped with [Leu-Enk+H]$^+$ ions as a function of trap loading time of the bare ion (prior to pick-up).

3.4 Droplets Generation

Helium clusters are generated by expanding high purity helium gas into vacuum at very low temperatures and high stagnation pressures. The flux of helium droplets is determined by the diameter of the orifice used for the expansion, the opening time of the pulsed nozzle, the stagnation pressure, and the nozzle temperature [116].

Helium droplets can be produced using either continuous or pulsed sources. Continuous sources are widely used due to the high beam fluxes of helium droplets that can be achieved, and the well defined initial conditions of the expansion in terms of pressure and temperature [72]. However, using a continuous source requires large vacuum pumps to maintain appropriate vacuum conditions. Moreover, experiments performed using pulsed lasers can only probe a very small fraction of the generated helium droplets. In these cases, pulsed sources have become popular since high peak fluxes of helium clusters can be achieved with lower background pressures, resulting in a less demanding pumping system to remove the emitted gas [116].

In this work, helium droplets are formed through the expansion into vacuum of 99.999% pure helium gas through a pulsed cryogenic Even-Lavie valve [116, 117] cooled to temperatures of a few Kelvin. The nozzle is refrigerated by a closed-cycle helium cryocooler (*Sumimoto* RDK 408D2) with a cooling power of 40 W at the first stage (30 K) and of 1 W at the second stage (~ 4 K). The central part of the cluster beam is cut out by a skimmer with a 4 mm diameter opening (*Beam Dynamics* Model 50.8) placed ~ 13.5 cm away from the nozzle.

A careful alignment of the valve and, thus, of the propagation axis of the droplets beam with the rest of the apparatus is crucial for the experiment. Therefore, the cold head is mounted on a vacuum chamber flange using stainless steel bellows. The position and orientation of the cold head can be changed using three threaded stainless steel ferrules.

In a typical experiment, the Even-Lavie valve is operated at a repetition rate of $5 - 10$ Hz, with a stagnation pressure of ~ 65 bars and an opening time of 19.1 µs. The nozzle is operated at a temperature range of $15-25$ K creating droplets consisting of $\sim 10^6$ to $\sim 10^4$ helium atoms, respectively. The droplets have typical velocities of $400 - 500$ m s^{-1} that result in a spatial width of ~ 80 µs within the laser-interaction region due to velocity spread. A detailed discussion on the size distribution of helium droplets employed in this work can be found in

Chapter 4.

The typical base and operating pressures of the different vacuum stages when the Even-Lavie valve is operated at a repetition rate of 10 Hz are summarised in Table 3.1 . The pressure in the source chamber is found to increase smoothly as the temperature of the nozzle T_{Nozzle} is lowered. The valve is operated such that the pressure in the source chamber does not rise higher than $1 \cdot 10^{-4}$ mbar and at a fore pressure of $1 \cdot 10^{-2}$ mbar.
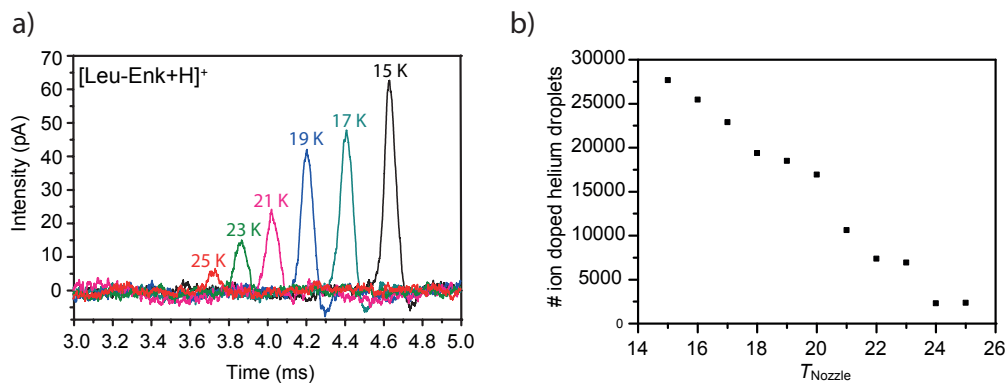
3.5 Detection of Doped Droplets

Using charged particles as dopants in helium droplets provides the great advantage of being able to directly detect the ion-droplet complex. On the one hand, this allows to systematically characterise different parameters of the helium droplet beam, such as its size or velocity as a function of nozzle temperature. A detailed knowledge of these parameters is crucial to achieve an optimal performance with the experimental apparatus. Additionally, being able to directly measure the current of the ion-doped helium droplets opens the possibility to investigate further the mechanisms behind the process by which an impurity is embedded inside a helium droplet. Two different detectors were employed for this task: the Faraday cup and the Daly type detector. Their characteristics are discussed in detail in this section.

3.5.1 Faraday Cup Detector

Figure 3.10: Two Faraday cups with a conical and a flat detection surface, respectively, were used in this thesis to detect ion-doped helium droplets.

Faraday cup detectors consist of a metal, conductive surface (copper, in this case) that gains a small net charge when a charged particle collides against it. The ion is then neutralised, and the metal can be discharged to produce a small current equivalent to the number of impinging ions. In the present experiment, this current is amplified by a current-to-voltage converter with a calibrated gain of 10^{10} V/A and a maximal bandwidth of 1.1 kHz (*FEMTO* DLPCA-200).

Figure 3.11: a) Typical traces of the helium droplets doped with [Leu-Enk+H]$^+$ measured with the Faraday cup detector for temperatures of the nozzle in the range $15-25$ K. b) Number of detected helium droplets doped with [Leu-Enk+H]$^+$ as a function of T_{Nozzle}.

Figure 3.10 shows the two Faraday cup detectors used in this work to detect ion-doped helium droplets. The Faraday cup with a conical shape (left side of Figure 3.10) has a very large detection surface which makes it particularly well suited to measure the signal of a beam with a rather large solid angle. The detector shown on the right side of Figure 3.10 has a flat detection surface that is orthogonal to the propagation axis of the molecular beam. As a consequence, the distance between the nozzle and the point where the ion-doped droplets are detected can be estimated in a more precise manner. Hence, this geometry allows to more accurately determine the beam velocity. The copper surface of this detector is considerably smaller than the surface of the conical Faraday cup. The detector is mounted with a so-called suppression grid that can be used to suppress secondary and scattered electrons or scattered ions, so that the current is not lost. In this experiment, the grid is usually kept at a small positive voltage ($\sim$ 2-3 V) in order to suppress current losses of scattered ions.

One of the main disadvantages of the Faraday cup detectors is the intrinsic difficulty related to the measurement of the typically low beam currents (less than $\sim$ 80 pA). However, their simplicity and the possibility of measuring the direct current of the ion-doped helium droplets makes the Faraday cup detectors particularly useful. These two detectors have been used to determine the size distributions of ion-doped helium droplets and their corresponding velocities presented in Chapter 4.

Figure 3.11 (a) shows typical traces measured with the Faraday cup detector of helium droplets doped with leucine-enkephalin ([Leu-Enk+H]$^+$, $\sim$ 556 Da) generated at a nozzle temperature (T_{Nozzle}) in the range of $15-25$ K. The intensity of the signal of the ion-doped helium droplets increases as the temperature of the nozzle is lowered, from $\sim$ 5 pA at $T_{\text{Nozzle}} = 25$ K until $\sim$ 70 pA at $T_{\text{Nozzle}} = 15$ K.

Being able to directly measure the current of the ion-doped helium droplet beam allows to directly determine the number of ion doped helium droplets for a given T_{Nozzle}. It is assumed

that each helium droplet is doped by only one charged ion. In principle, pick-up of multiple ions by a single helium droplet is possible. As a first approximation, one of the requisites that have to be met is for the particle density in the trap to be sufficiently high to allow multiple collisions between droplets and ions. However, this event seems unlikely assuming an ion density in the trap of $\sim 10^6$ ions $\cdot$ cm^{-3} [12], the geometry of the trap introduced in Section 3.3 and helium droplets with radius of between ~ 60 and ~ 300 Å. Moreover, the experimental results presented in Chapter 4 strongly indicate that multiple ion pick-up does not take place under the current experimental conditions. There, it is shown that ion-doped droplets are accelerated from different voltages applied to the trap bias towards a ground potential placed just outside the trap. Then, the temporal profiles are fitted according to their width and arrival time. Droplets containing more than one ion would experience a larger acceleration which would be reflected in the measured arrival time distribution. However, the measurements performed for a wide range of sizes of helium droplets show temporal profiles that are in excellent agreement with the assumption that each droplet is doped with a single ion.

The number of ion-doped helium droplets can be obtained by integrating the measured signal as shown in Figure 3.11 (a) and dividing the result by the elementary charge $z = 1.6 \cdot 10^{-9}$ C (in case of singly charged ions). The results depicted in Figure 3.11 (b) show that the number of detected doped droplets increase with increasing cluster size. Approximately 27000 helium droplets doped with [Leu-Enk+H]$^+$ are detected per pulse when the valve is operated at $T_{\text{Nozzle}} = 15$ K. This number decreases linearly as the temperature of the nozzle increases, until $T_{\text{Nozzle}} = 25$ K, where only ≈ 2300 ion doped helium droplets are detected. No signal of helium droplets doped with [Leu-Enk+H]$^+$ is obtained for higher T_{Nozzle} (see Chapter 4 for a detailed discussion).

3.5.2 Daly Detector

Ion-doped helium droplets can also be detected with a Daly detector [118]. This kind of detector consists of a *doorknob* shaped metal block made of aluminum placed off-axis and set to a high voltage (~ 20 kV). Secondary electrons are released when the ions hit the metal block, and are subsequently accelerated towards an electron multiplier placed at a distance of ~ 5 cm and held at a voltage of ~ 3.2 kV. The signal is amplified with the same *FEMTO* DLPCA-200 amplifier introduced in section 3.5.1.

Figure 3.12 shows typical signals of helium droplets doped with [Leu-Enk+H]$^+$ obtained with this kind of detector for nozzle temperatures in the range of $15-25$ K. One of the main advantages of the *Daly* detector is its high sensitivity, increasing the signal-to-noise ratio by a factor 100. However, its unknown mass dependent detection efficiency does not make it suitable to perform experiments where the size of the helium droplets are probed.
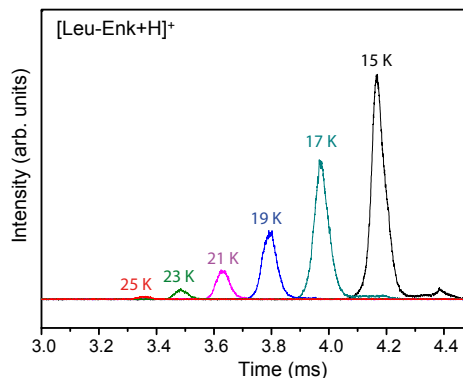
Figure 3.12: Typical traces of helium droplets doped with [Leu-Enk+H]$^+$ recorded with the *Daly* detector for temperatures of the nozzle between 15 - 25 K.

3.6 Infrared Light Source

The experiments presented in this work were performed using the Fritz Haber Institute IR-free-electron laser (FHI FEL) [119]. In this section, the operating principles of free electron lasers are briefly described, based on Ref. [120, 121], followed by a summary of the characteristics of the FHI FEL.

3.6.1 Operating Principles

The infrared radiation of a FEL is generated from the acceleration of free electrons to speeds close to the speed of light. Pulses of electrons are produced by an electron gun and brought to energies of several MeV by linear accelerators. The beam is subsequently injected into an *undulator*, where a periodic array of magnets with alternating poles are arranged as schematically shown in Figure 3.13. The perpendicular magnetic field causes the accelerated electrons to *wiggle* transversely along a sinusoidal path due to Lorentz's forces. As a result, the electrons emit photons with a wavelength determined by the travelled effective path length per undulator period λ_u. Since the electrons do not move in a straight line but in a sinusoidal manner, the travelled path length is longer than λ_u by a factor $(1+K^2)$, where K is a dimensionless parameter that accounts for the strength of the magnetic field [121].

Two additional relativistic effects have to be accounted for in order to determine the wavelength of the emitted photons. First, in the rest frame of the electron, the undulator appears contracted and λ_u appears reduced by the relativistic Lorentz factor

$$\gamma = \frac{E}{m_0 c^2} = \frac{1}{\sqrt{1-\beta^2}} \qquad \text{with} \quad \beta = \tfrac{v_z}{c}, \tag{3.13}$$

where E is the energy of the electron and m_0 its mass at rest. Second, the emitted light is further shifted by a factor 2γ due to the strong Doppler effect in the laboratory frame. As a
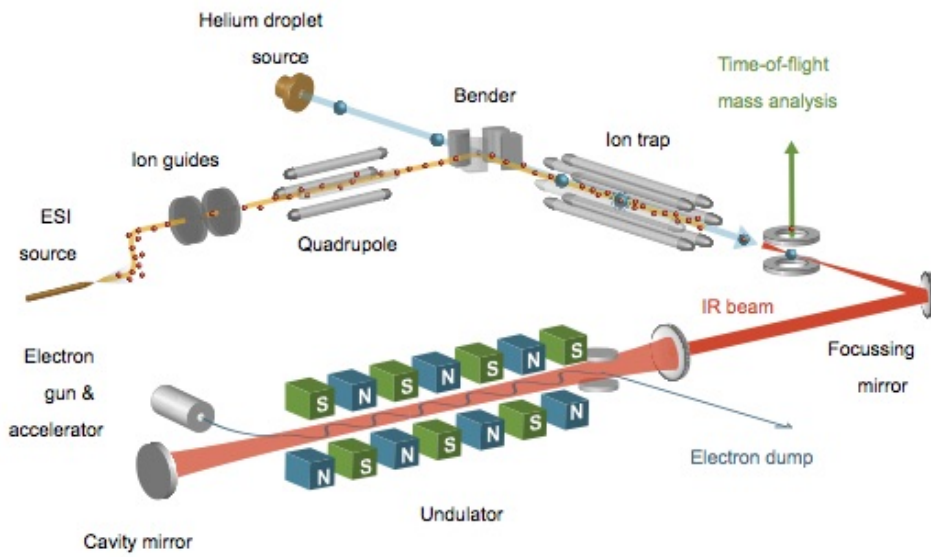
Figure 3.13: Schematic view of the free electron laser coupled to the experimental setup.

result, the wavelength of the emitted radiation is determined by

$$\lambda_{\text{emission}} = \frac{\lambda_u}{2\gamma^2}(1 + K^2). \tag{3.14}$$

However, the initially emitted radiation is weak and incoherent due to the much larger spatial spread of the electrons compared to $\lambda_{\text{emission}}$. This is solved by placing the undulator inside an optical resonator with two high-reflective dielectric mirrors at each side as shown in Figure 3.13. As a result, the emitted radiation is reflected between both mirrors. The resonator is tuned such that when new electrons are injected in the cavity they interact with the inhomogeneous magnetic field and experience a so-called *ponderomotive force*. The electron density along the longitudinal axis of the undulator can be modulated on the scale of the modulated wavelength in an effect called *microbunching*. As a result, the emitted radiation is no longer incoherent, the electrons radiate in phase which results in an increase of the radiation power by many orders of magnitude. Light is then extracted through a central hole in the outcoupling mirror.

### 3.6.2 Characteristics of the FHI FEL

In the FHI FEL electrons are generated by an electron gun modulated at 1 GHz and accelerated to an energy of up to 50 MeV by two linear accelerators.

Presently, the FEL is tunable between 3.5 µm and 50 µm, making it very well suited for the

investigation of biological molecules using vibrational spectroscopy. The light comes in macro pulses of up to 10 µs in length, each of which contains micro pulses of 0.3 - 5 ps length, spaced by 1 ns [119]. The total macropulse energy can reach well above 100 mJ. The full width at half maximum is kept near 0.5% of the corresponding wavelength. Calibration is performed by measuring the FEL spectrum with a Cherny-Turner grating spectrometer equipped with a pyro array detector for several wavelength points within an experimental spectrum. The spectrometer itself is calibrated against a stabilized HeNe laser.

3.7 Detection after Photo Excitation

The absorption of multiple resonant photons can lead to the ejection of an ion, originally embedded in a superfluid helium droplet [33, 34] (see Section 2.2.4). Monitoring the ejection process as a marker for photon absorption was routinely used in this work to obtain the IR spectra of biological molecules presented in Chapters 5 and 6.
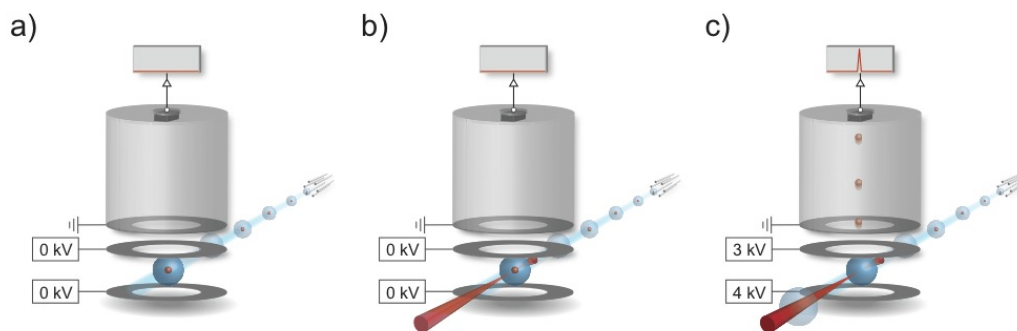
Figure 3.14: Schematic view of the detection of ions ejected from helium droplets after photo excitation. Once the ion-doped helium droplet is placed roughly between the extraction plates (a) it interacts with the counter propagating IR laser light (b). At this moment, the extraction plates are switched to high voltage (c) and the ejected ion is detected by an electron multiplier.

A schematic view of the experimental setup developed for this task is depicted in Figure 3.14. It is a home built Wiley-McLaren type time-of-flight mass spectrometer (TOF) [122]. The ejected ions are repelled by the high voltage applied to the extractor and repeller plates and accelerated to different velocities v depending on their mass m and charge state z by the homogeneous electric field applied to the TOF mass spectrometer. The ejected ions are then detected by an electron multiplier (*ETP ion detect*, AF880). The signal is amplified by an amplifier (*Phillips Scientific*, 6954) and then sent to a 100 MHz, 12-bit digitizer (*Acquiris*, DC440) .
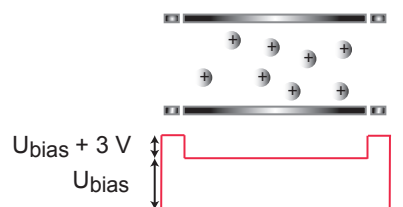
A system of three delay generators is used to carefully trigger the experimental apparatus. A schematic view of the trigger scheme employed during the spectroscopic work is depicted in

Figure 3.15. First, ions are accumulated in the ion trap during several seconds and thermalised to the ambient temperature *via* collisions with the buffer gas atoms. After the trap has been sufficiently filled, the residual buffer gas is pumped away during 3 seconds. During the next 10 seconds, the experiment is triggered as follows. The triggers of the detection scheme coordinate three different events: generation of the droplets, firing of an IR macro pulse, and applying a high voltage to the extraction plates. All delays are dictated by the so-called FEL trigger t_0. Macro pulses of IR radiation are fired at $t_0 + 3800$ µs at a repetition rate of 5 Hz. The droplet source is typically operated at a repetition rate of 10 Hz. At $T_{\text{Nozzle}} = 25$ K, the droplets require a flight time of ~ 2800 µs between the nozzle and the TOF mass spectrometer. This time can vary until up to ~ 3500 µs for the slower, larger droplets produced at $T_{\text{Nozzle}} = 15$ K. Thus, generating the droplets approximately ~ 1000 µs to ~ 300 µs after t_0 provides enough time for the droplets to reach the detection region at $t_0 + 3800$ µs. At this point, the acquisition system starts recording data. Setting the acquisition system to start recording data at $t_0 + 3800$ µs allows to maintain the rest of the delays constant, independent of the droplet size by only varying the delay for droplet generation. Once the ion-doped helium droplets are located roughly between the extraction and detection plates ($t_0 + 3800$ µs), macro pulses of IR radiation are fired. If the generated photons are resonant with a vibrational transition, the ion can be ejected from the droplet. In order to re-direct the ejected ion towards the electron multiplier mounted on top of the TOF mass analyser, a high voltage is applied to the extraction plates during the next 200 µs at a delay $t_0 + 3800$ µs.
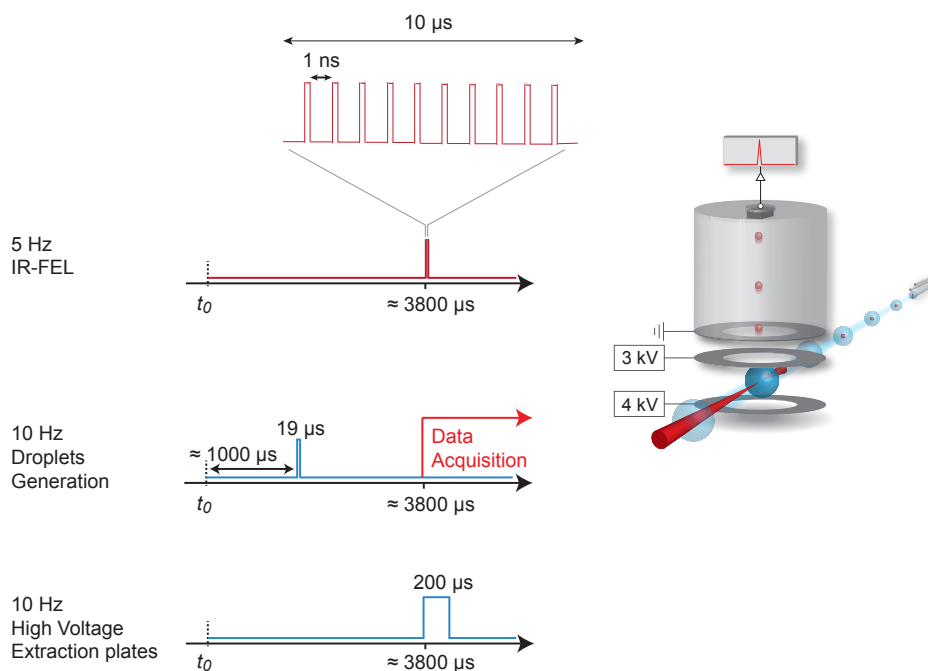
In order to improve the signal-to-noise ratio, a so-called *background mode* is employed in which two different data sets are needed, the already mentioned signal of the ejected ions and, additionally, the signal obtained when the ion-doped droplets are present in the detection region but the laser light is absent. The final signal is given by the subtraction of both data sets.

1. **Trap loading during 5 seconds**
   Buffer gas collisions help remove
   excess of kinetic energy

U_{bias} + 3 V
U_{bias}

2. **Data acquisition during 10 seconds**

10 µs

1 ns

5 Hz
IR-FEL

t_0 ≈ 3800 µs

3 kV

4 kV

10 Hz
Droplets
Generation

19 µs

≈ 1000 µs

Data
Acquisition

t_0 ≈ 3800 µs

10 Hz
High Voltage
Extraction plates

200 µs

t_0 ≈ 3800 µs

Figure 3.15: The trigger system for spectroscopic work is composed of two steps. First, the ion trap is loaded for approximately 5 seconds. After the trap is sufficiently filled, the data is acquired during the next 10 seconds. During that time, the helium droplets beam and the extraction plates are pulsed at a frequency of 10 Hz, while the free electron laser is operated at a repetition rate of 5 Hz.

4 Pick-Up Probability of Molecular Ions by Helium Droplets*

Evaporation of helium atoms is generally considered the main factor that determines the minimal size of a superfluid helium droplet required to pick-up a certain impurity. In this chapter, a systematic investigation of the pick-up probability as a function of the mass and size of the dopant is presented. The experimental results demonstrate that there is a droplet size dependent pick-up process that leads to a minimum size of doped droplets that can be detected. However, these results can not be explained in terms of thermal evaporation. In order to gain insight into the constraints and limitations of the pick-up process different hypotheses are discussed. The role of kinetic energy on the pick-up process is investigated and compared to theoretical models. Additionally, the possibility of size dependent stability of the doped droplet is considered.

4.1 Introduction

Superfluid helium droplets have been used for over 20 years as "nano-cryostats" allowing to isolate individual atoms and molecules and investigate their properties, for example performing microwave and infrared spectroscopy [27, 31, 72, 74]. In most experiments, the species of interest are incorporated into the helium droplets *via* mechanical impact in a gas cell. The widely-employed pick-up technique [42] is based on the thermalisation of the dopant with the surrounding helium environment, which results in evaporation of helium atoms, thereby removing the energy of the dopant. As a result, the species of interest are trapped inside the droplet at the superfluid helium temperature (~ 0.37 K). This versatile technique has been successfully applied to incorporate all kinds of dopants into the droplets, from small molecules [54] and alkali metals [55] to C_{60} buckyballs [56].

A crucial experimental parameter which determines the efficiency of the pick-up process is the size of the nanodroplets [27]. Therefore, particular attention has been paid to controlling and measuring the number of helium atoms composing a droplet. For continuous beams, acceleration after capture of metal ions [123] and electrons [124], as well as scattering by a secondary beam [125] have been used to determine the size of the helium droplets. For pulsed beams, the size distributions have been obtained by monitoring the fluorescence of the embedded species [126] and using Rayleigh scattering of light [116]. Recently, the size distributions of larger droplets of up to 10^{10} helium atoms have been experimentally determined [127] by monitoring the He_2^+ fragments ejected after multiple ionisation.

A general problem arising for the direct measurement of the size distributions is the requirement of charged particles needed to apply the standard mass selection techniques. Therefore, despite the thorough characterisation of the droplet size distributions performed in the past, a major question still remains unanswered, namely which are the constraints for the pick-up of impurities by helium droplets.

To date, evaporation of helium atoms due to the dissipation of the internal and collision energy has been considered the main factor that limits the minimum droplet size required to pick-up an impurity. As an example, measuring the reduction of the droplet size as a result of thermalisation of a SF_6 molecule has provided a limit of ~ 1000 helium atoms on the minimum size of droplets that can be employed in this particular case [76]. Recently, Chen *et al.* [77] have proposed a correlation between the kinetic energy and the limited doping efficiency, arising from a finite deceleration rate of the ion inside the droplet.

Here, we use acceleration experiments of the ion-doped helium droplets in order to directly measure the size distributions of doped droplets as a function of dopant. This was made possible by the recently introduced pick-up technique employing mass-to-charge selected ions from a linear radio-frequency ion trap [32, 33]. As a result we are able to systematically study the pick-up process for a broad range of molecular ions with masses from ~ 133 Da to ~ 12 kDa. The measurements show that there is a dopant dependent minimum droplet size below which no doped droplets are observed. The results are discussed in terms of two possible

pick-up constraints, namely (*i*) an insufficient dissipation of the collision energy through the helium environment, and (*ii*) that there are a minimum number of helium atoms required for solvation to be energetically favourable.

4.2 Experimental Setup and Computational Details

4.2.1 Experimental Setup
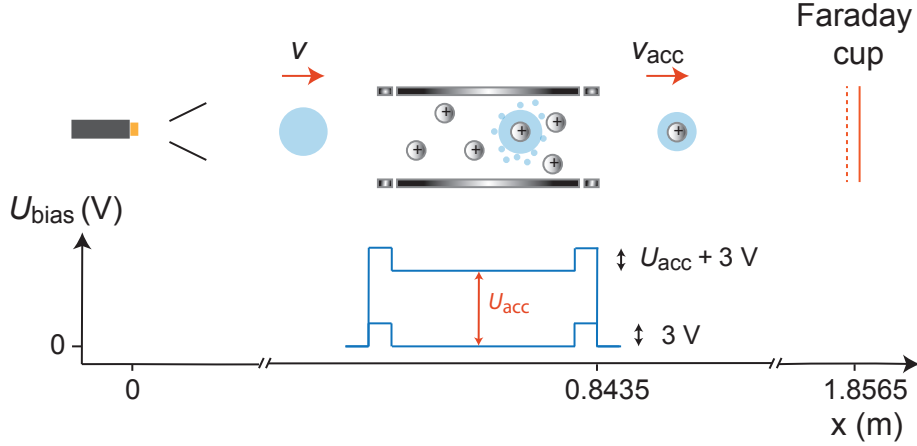
Figure 4.1: Schematic of the experimental setup used to investigate the size distribution of helium droplets doped with biomolecular ions. The doped helium droplets are accelerated towards a ground electrode placed outside the trap for different acceleration voltages U_{acc}. The arrival time distributions are measured with a Faraday cup.

The size distributions of helium droplets doped with biomolecular ions have been studied using time-of-flight mass spectrometry with the experimental setup shown in Figure 4.1. The ions of interest are confined inside a hexapole ion trap where they can be picked up *via* mechanical impact by the traversing beam of helium droplets. The ion-doped helium droplets are accelerated from a voltage U_{acc} applied to the trap bias towards a ground potential placed just outside the trap. Further downstream, the doped helium droplets are detected using a Faraday cup connected to a calibrated current-to-voltage amplifier (Femto DLPCA-200).

Figure 4.2 (a) shows the temporal profiles for four different U_{acc} voltages that are obtained with helium droplets doped with [Leu-Enk+H]$^+$. The droplet source was operated at $T_{Nozzle} = 25$ K with a stagnation pressure of ~ 68 bar at a repetition rate of 10 Hz. Figure 4.2 (b) shows the time profile of the unaccelerated beam. This time profile can be fitted with a Gaussian velocity distribution (red solid line) of ~ 510 m s^{-1} and a full width at half maximum of ~ 4 m s^{-1}. Under the experimental conditions used here, the measured peak currents of the unaccelerated beam are ~ 2 pA with the source operated at $T_{Nozzle} = 25$ K increasing to values of up to 80 pA at $T_{Nozzle} = 15$ K. The upper three panels of Figure 4.2 (a)
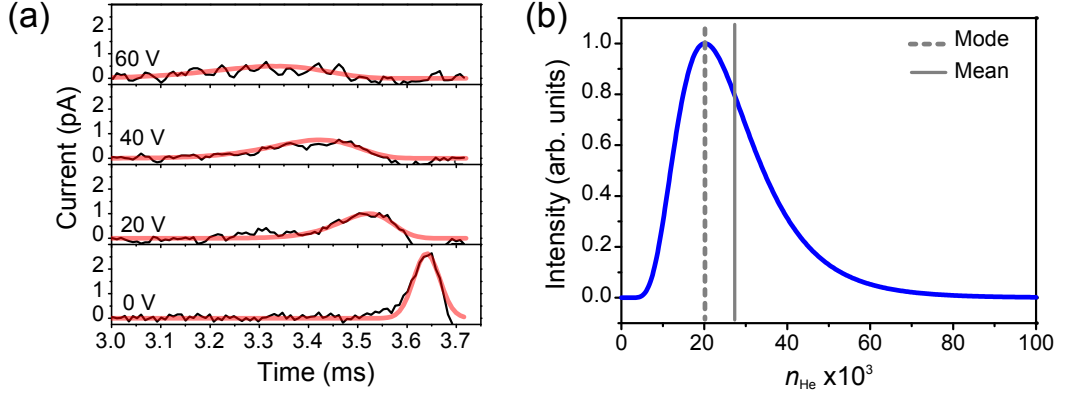
Figure 4.2: a) Measured temporal profiles (black) of droplets doped with [Leu-Enk+H]$^+$ for four different acceleration voltages and $T_{Nozzle} = 25$ K, together with the fit of the expected log-normal distribution (red). b) Fitted droplet mass distribution obtained using the time profiles of panel a).

show the time profiles of the accelerated beam for three different trap bias potentials U_{acc}. Since the droplets do not have a single mass, but a broad mass distribution, the time profiles become broader and shift towards shorter arrival times with increasing acceleration voltages.

The size distribution of a helium cluster can be well described by a log-normal distribution with the probability density function

$$P(n) = \frac{1}{n\sigma\sqrt{2\pi}}e^{-\frac{(ln(n)-\mu)^2}{2\sigma^2}}, \tag{4.1}$$

where μ and σ describe the mean and the standard deviation, respectively [125]. While these parameters depend on the temperature of the source, they are independent of the acceleration voltage at a given temperature. The values of μ and σ were obtained by fitting the data of Figure 4.2 (a) with Equation 4.1, which resulted in the size distribution shown in Figure 4.2 (b). The maximum (mode) of a lognormal distribution is given by $e^{\mu-\sigma^2}$ and is shown in Figure 4.2 (b) with a dotted grey line. However, the mean value, $e^{\mu+\frac{\sigma^2}{2}}$ (solid grey line in Figure 4.2 (b)), is often a more useful parameter to describe the size distribution.

4.2.2 Materials

In order to investigate the pick-up probability as a function of dopant, several different species have been used: caesium cations (Cs$^+$, $\sim$ 133 Da), the amino acid tyrosine ([Tyr+H]$^+$, $\sim$ 182 Da), the pentapeptide leu-enkephalin in the form of the monomer ([Leu-Enk+H]$^+$, $\sim$ 556 Da) and the dimer ([2Leu-Enk+H]$^+$, $\sim$1111 Da), the pentadecapeptide gramicidin A ([GA+2H]$^{2+}$, $\sim$ 1882 Da), and the two proteins ubiquitin from bovine erythrocytes ([Ubi+8H]$^{8+}$, $\sim$ 8.5 kDa) and cytochrome C from equine heart ([CytC+8H]$^{8+}$). All species were purchased from *Sigma Aldrich* and used without further purification. The species were

dissolved at 50 µM in a 1:1 H_2O:MeOH solution with 1% formic acid, with the exception of Cs^+ that was dissolved at concentrations of up to 10 mM.

4.2.3 Calculation of Helium Solvation Energies*

A charged molecule inside a helium droplet will interact *via* van der Waals as well as *via* charge-induced dipole interaction. Further, for the total energy balance, the cost for creating the void in which the molecule is inserted has to be taken into account. The creation of the void can be treated as a two step process. In the first step, a cluster of helium atoms of the size of the molecule that will eventually fill the void is cut out. Those helium atoms are then redistributed in the droplet, which slightly increases the outside surface of the droplet, thereby slightly increasing its surface energy. However, this effect can be neglected. The helium atoms on the surface of the void will lack the dispersion interaction with the previously present helium atoms. This interaction is replaced by a dispersive interaction with the molecule that will fill the void. The difference between molecule−helium and helium−helium interaction can be used in order to calculate the dispersion energy. In practice, we use an estimated molecular structure (see below) and calculate the solvent accessible surface area (SASA) using the program VMD [128]. This SASA is then further broken down to contributions from exposed hydrogen, carbon, nitrogen and oxygen atoms, again using VMD. The number of interacting helium atoms is calculated by dividing the SASA by the square of the diameter of a helium atom (1.9 A). The well depth for the dispersive interactions for He-He, He-H, He-C, He-N and He-O is estimated by using the MM3 parameter set [129] and taking the geometric means of the respective parameters. It is important to note that the He-H interaction is weaker than the He-He interaction. The He-C, He-N and He-O interactions, on the other hand, are stronger. A large number of exposed hydrogen atoms can thus lead to an interaction that is weaker (unbound) than the void would have when being filled with helium atoms. Thus, it is not necessarily expected for the van der Waals binding energy difference to be monotonic with system size, but rather to depend on the composition of the exposed molecular surface. In order to estimate the polarization interaction, the COSMO continuum model [130] as implemented in Turbomole [131] and MOPAC [132] is used.

For [Leu-Enk+H]$^+$, a previously proposed structure is used [25]. The SASA is calculated to be 838 Å^2, which results, using the procedure described above, in a difference in van der Waals binding, compared to the helium the molecule replaces, of -0.01 eV. To calculate the charged-induced dipole (dispersion) binding energy using the COSMO model, the electron density distribution in the molecule needs to be calculated. In the case of protonated [Leu-Enk+H]$^+$, Turbomole using the B3LYP density functional, the def2-SVP basis set and a helium dielectric constant of 1.057 the dispersion energy using the COSMO model is calculated to be -0.06 eV. MOPAC, using the semiempirical PM3 Hamiltonian, is in fair agreement and results in dispersion energy of -0.08 eV. The resulting total binding energy of protonated [Leu-Enk+H]$^+$

---

*calculations by Gert von Helden

can thus be estimated to be between -0.07 eV and -0.09 eV.

As the system size of $[2\text{Leu-Enk}+\text{H}]^+$ is large, dispersion energies for this and larger species are only calculated using MOPAC. A structure is derived using a molecular dynamics based, empirical force field approach. Its SASA is calculated as 1173 Å^2 and the resulting van der Waals binding difference is very small (-0.007 eV). Its dispersion energy is -0.075 eV. The total binding can thus be estimated to be -0.08 eV.

The difficulty in performing the same calculations for $[\text{GA}+2\text{H}]^{2+}$ lies in the fact that this peptide does not have an easily identifiable basic site, and thus it is not clear where protonation occurs. We presume the first and last amidic nitrogen to be protonated and calculate accordingly the molecular structure using Turbomole. The resulting structure has a SASA of 1751 Å^2, resulting in a difference in van der Waals binding of +0.01 eV (thus unbound). The calculated dispersion energy (using MOPAC) is -0.19 eV. The total binding can thus estimated to be -0.18 eV.

For $[\text{Ubi}+8\text{H}]^{8+}$, two different structures and two different charge states are considered. The compact, native like structure of a neutral molecule is taken. Interaction energies for the extended "A-state" structure are calculated for the neutral as well as the +11 charge state [133]. The SASA ranges from 4900 Å^2 for the compact structure to 7700 Å^2 for the extended structure, with van der Waals binding energy differences ranging from -0.19 eV to -0.15 eV, respectively. The corresponding dispersion energies range from -1.3 eV for the compact neutral structure, -1.6 eV for the extended neutral structure to -2.6 eV for the extended structure in charge state +11. In the present experiment, the charge state +8 is investigated. It is known to be extended [133] and for a coarse estimate of the polarization interaction energy, we interpolate between the charge 0 and charge +11 values to obtain -2.3 eV as a value for the polarization energy. Together with the van der Waals energy difference, the total binding energy can be estimated to be -2.5 eV.

4.3 Results and Discussion

4.3.1 Size Distributions of Ion-doped Helium Droplets

The size distributions of the helium droplets are investigated as a function of nozzle temperature using caesium cations (Cs^+, $\sim$ 133 Da) as a dopant (see Figure 4.3 and Table 4.1). As expected, the size of the helium droplets increases as the temperature of the nozzle is lowered. The droplets formed at $T_{\text{Nozzle}} = 25$ K have a size distribution with a mean value of $\sim 2.5 \cdot 10^4$ helium atoms ($r_{\text{droplet}} \sim 65$ Å) and this increases steadily until $T_{\text{Nozzle}} = 18$ K for which the mean value of the distribution is $\sim 1.4 \cdot 10^5$ helium atoms ($r_{\text{droplet}} \sim 115$ Å). However, at $T_{\text{Nozzle}} = 17$ K the distribution is bimodal and peaked around two different sizes ($\sim 10^5$ and 10^6 helium atoms). For temperatures lower than $T_{\text{Nozzle}} = 17$ K only one size distribution, corresponding to $\sim 10^6$ helium atoms ($r_{\text{droplet}} \sim 222$ Å), is observed. It is important to note that Cs^+ can be efficiently doped into even smaller droplets than the ones produced at
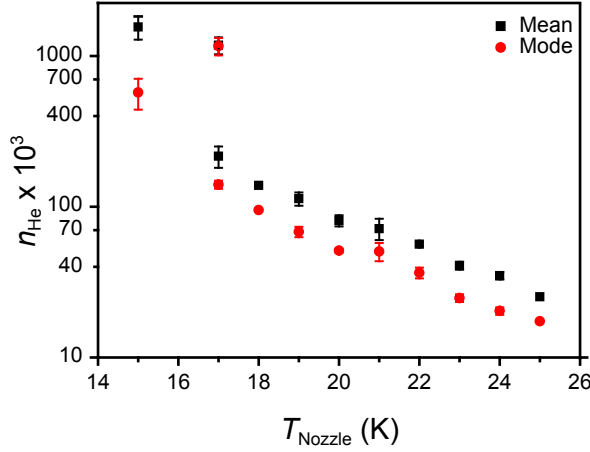
Figure 4.3: Mean (black squares) and mode (red circles) values of the size distributions for helium droplets doped with Cs^+, as a function of the source temperature.

Table 4.1: Measured mean velocities, v, and mean and mode number of helium atoms, $n_{\mathrm{He}}^{\mathrm{Mean}}$ and $n_{\mathrm{He}}^{\mathrm{Mode}}$, respectively, for helium droplets doped with Cs^+ as a function of temperature of the nozzle, T_{Nozzle}. The calculated radius of the mean size of helium droplets, r_{Mean}, and its corresponding cross section, σ_{D}, are also shown.

T_{Nozzle} (K)	v (m s^{-1})	$n_{\mathrm{He}}^{\mathrm{Mode}}$	$n_{\mathrm{He}}^{\mathrm{Mean}}$	r_{Mean} (Å)	σ_{D} (Å^2)
25	510	$1.7 \cdot 10^4$	$2.5 \cdot 10^4$	65	17 400
23	490	$2.4 \cdot 10^4$	$4.0 \cdot 10^4$	76	18 300
21	470	$5.0 \cdot 10^4$	$7.1 \cdot 10^4$	92	26 700
19	450	$6.8 \cdot 10^4$	$1.1 \cdot 10^5$	107	36 200
17	425	$1.4 \cdot 10^5$	$2.1 \cdot 10^5$	133	55 800
17	425	$1.1 \cdot 10^6$	$1.2 \cdot 10^6$	235	172 800
15	405	$7.1 \cdot 10^5$	$1.8 \cdot 10^6$	273	234 000

$T_{\mathrm{Nozzle}} = 25$ K. However, the signal is too weak to perform measurements with the Faraday cup and therefore no experimental data points were collected at higher temperatures. The low signal-to-noise ratio can be overcome using a Daly-type detector, where the sensitivity is increased by a factor of 100. Using this detector, helium droplets doped with Cs^+ can be detected for nozzle temperatures up to 31 K ($v \sim 590$ m s^{-1}). The signal becomes weaker for $T_{\mathrm{Nozzle}} = 33 - 35$ K ($v \sim 615$ m s^{-1}) and is completely absent for $T_{\mathrm{Nozzle}} = 37$ K. Although the signal-to-noise ratio is dramatically improved when a Daly-type detector is used, its sensitivity depends on the droplet mass in an unknown way and the signal can therefore not be used to determine the size distributions.

The size distributions of the ion-doped helium droplets presented here are in good general agreement with the results reported in the past [33] and with the size distributions obtained by Lavie *et al.* using a very similar pulsed valve [116].

4.3.2 Pick-up Probability as a Function of the Ion Mass and Size

In order to further investigate the pick-up process, the size distributions of helium droplets have been measured for a variety of biomolecular ions, ranging from protonated amino acids to proteins. Figure 4.4 shows the mean value of the size distributions of helium droplets doped with four different ions. For reference purposes, the values for droplets doped with Cs^+ are shown as well. From Figure 4.4 (a) one can see that small ions such as $[Leu\text{-}Enk+H]^+$ are easily trapped in the droplets of all sizes created at $T_{Nozzle} = 15 - 25$ K. However, the droplets doped with a larger peptide such as $[2Leu\text{-}Enk+H]^+$ can only be observed for $T_{Nozzle} = 15 - 23$ K, see Figure 4.4 (b). Doping of even larger species like, for example, $[GA+2H]^{2+}$, was observed only for $T_{Nozzle} = 15 - 20$ K, see Figure 4.4 (c). Finally, doping of proteins like ubiquitin $[Ubi+8H]^{8+}$ was detected only for $T_{Nozzle} = 15 - 17$ K, see Figure 4.4 (d).
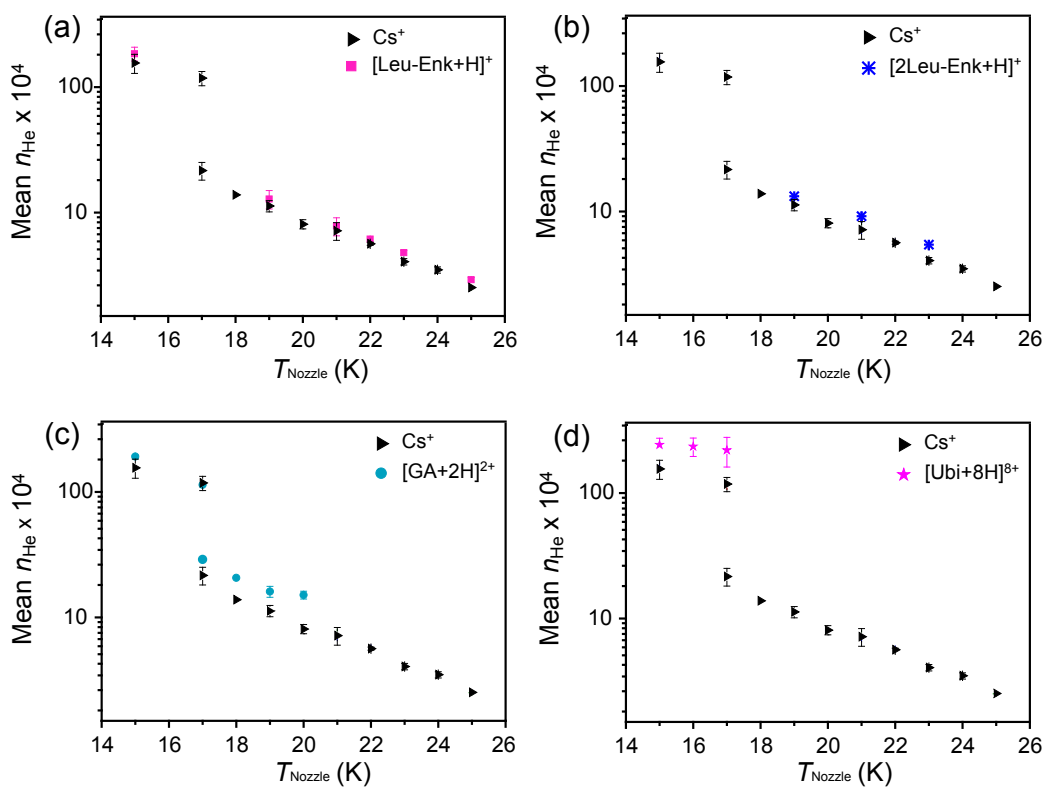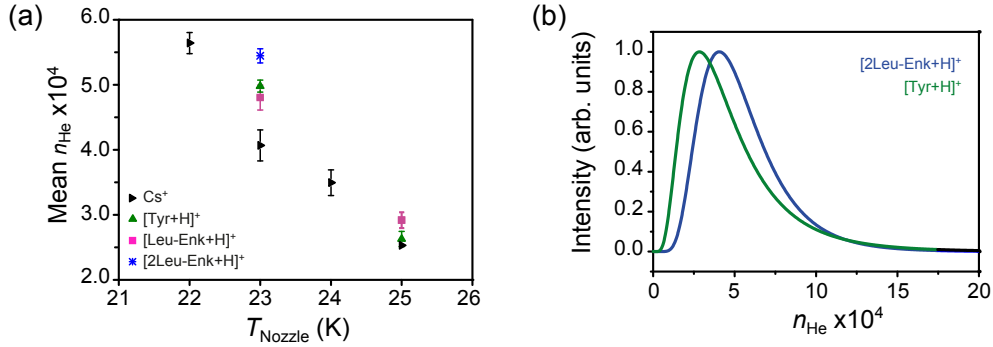

Figure 4.4: Size distributions of helium droplets doped with different biomolecular ions: (a) $[Leu\text{-}Enk+H]^+$, (b) $[2Leu\text{-}Enk+H]^+$, (c) $[GA+2H]^{2+}$, (d) $[Ubi+8H]^{8+}$, as a function of nozzle temperature. The size distributions measured for Cs^+ (black triangles) are shown as a reference.

These experimental results show that larger droplets are required to pick up larger species.

Table 4.2: Parameters of the smallest helium droplets required to pick-up different biomolecular ions.

	Mass (Da)	σ_{ion} (Å^2)	T_{Nozzle} (K)	v (m s^{-1})	$n_{\text{He}}^{\text{Mean}}$
[Leu-Enk+H]$^+$	556	161 [134]	25	510	$2.9 \cdot 10^4$
[2Leu-Enk+H]$^+$	1111	248 [134]	23	490	$5.4 \cdot 10^4$
[GA+2H]$^{2+}$	1884	386 [134]	20	460	$1.5 \cdot 10^5$
[Ubi+8H]$^{8+}$	8500	1646 [134]	17	425	$2.4 \cdot 10^6$
[CytC+8H]$^{8+}$	12000	1250 [135]	17	425	$1.6 \cdot 10^6$

The observations are further supported by a detailed analysis of the temperature range of $T_{\text{Nozzle}} = 22 - 25$ K, presented in Figure 4.5 (a). For example, at $T_{\text{Nozzle}} = 23$ K, the mean value of the size distribution measured using [2Leu-Enk+H]$^+$ as a dopant is larger than for a smaller cation like [Tyr+H]$^+$. Similarly, for a droplet beam produced at $T_{\text{Nozzle}} = 25$ K, the mean value of the size distribution of helium droplets doped with [Leu-Enk+H]$^+$ is shifted towards larger values compared to the droplets doped with [Tyr+H]$^+$. This effect becomes even more evident when the predicted lognormal distributions are compared to each other, see Figure 4.5 (b). The distribution measured for droplets doped with [2Leu-Enk+H]$^+$ (blue) at $T_{\text{Nozzle}} = 23$ K is clearly shifted towards a higher number of helium atoms with respect to the lognormal distribution measured for [Tyr+H]$^+$ (green). The summary of the smallest size distributions required for pick-up is presented in Table 4.2.

Figure 4.5: (a) Size distributions of helium droplets for different dopants as a function of T_{Nozzle}. (b) Lognormal size distributions of helium droplets obtained at $T_{\text{Nozzle}} = 23$ K with [2Leu-Enk+H]$^+$ (blue) and [Tyr+H]+ (green) as dopants.

4.3.3 The Influence of Thermal Evaporation on the Droplet Size Distribution

The pick-up of an impurity by a helium droplet involves an inelastic collision where the internal energy of the ion, E_{int}, and the collision kinetic energy are transferred to the droplet [42, 75]. Thus, the energy associated with the pick-up is given by

$$E_{\text{pick-up}} \quad = \quad \frac{1}{2} \frac{m_{\text{ion}} m_{\text{D}}}{m_{\text{ion}} + m_{\text{D}}} (v_{\text{ion}} - v_{\text{D}})^2 + E_{\text{int}}, \tag{4.2}$$

where m_{ion} and m_{D} are the masses of the ion and the droplet, respectively, and v_{ion} and v_{D} denote the corresponding velocities.

The ions confined in the hexapole trap are thermalised at ~ 300 K before pick-up by the traversing beam of helium droplets takes place. Thus, the ion velocities, $v_{\text{ion}} \sim 20 - 60$ m s^{-1}, are negligible compared to the droplet velocities, $v_{\text{D}} \sim 400 - 500$ m s^{-1}. In addition, since $m_{\text{D}} \gg m_{\text{ion}}$, Equation 4.2 can be simplified to

$$E_{\text{pick-up}} \sim \frac{1}{2} m_{\text{ion}} v_D^2 + E_{\text{int}}. \tag{4.3}$$

After pick-up, the energy $E_{\text{pick-up}}$ is dissipated into the helium environment, which results in the release of helium atoms from the droplet surface and the evaporative cooling of the remaining droplet.

The number of helium atoms released during this process is estimated as ~ 1600 atoms per 1 eV of the pick-up energy [27]. The internal energy in Equation 4.3 can be approximated as ~ 0.3 eV *per* amino acid residue, based on an estimation of the internal energy of a protein of ~ 30 eV using typical values for the heat capacity [136]. Thus, thermalisation of a helium droplet doped with a protein like [Ubi+8H]$^{8+}$ could lead to the evaporation of $\sim 5.3 \cdot 10^4$ atoms, while evaporation of only $\sim 4 \cdot 10^3$ atoms is required to thermalise small peptides such as [Leu-Enk+H]$^+$. A comparison with the experimental results of Table 4.2 (also see Refs. [134, 135]) shows that the fraction of helium atoms evaporated during the pick-up process is small compared to the measured size distributions of the doped droplets. Therefore, a complete evaporation of the droplet is not expected to be an issue under the experimental conditions presented here. Further, keeping the parameters of the source constant, it is observed that droplets doped with larger ions yield larger size distributions (see Figure 4.5). However, the opposite would be expected based on helium atom evaporation alone.

In order to experimentally study the evaporative cooling during the pick-up process, the size distributions of the helium droplets were measured using an ion trap whose housing is refrigerated with liquid nitrogen. There, the ions are cooled to temperatures of around 80 K prior to pick-up. Thereby, E_{int} is drastically reduced and thus supposedly also the number of helium atoms lost during evaporation. The experiment was repeated using [Tyr+H]$^+$, [Leu-Enk+H]$^+$, [2Leu-Enk+H]$^+$, and [Ubi+8H]$^{8+}$ as dopants. It was found that cooling down the ions before pick-up does not lead to a significant difference in the measured size

Table 4.3: The size distributions of helium droplets doped with different biomolecular ions have been measured with the housing of the trap kept at room temperature (~ 300 K) and cooled down using liquid nitrogen (~ 80 K).

Dopant	T_{Nozzle} (K)	~ 300 K $n_{\text{He}}^{\text{Mean}}$	~ 80 K $n_{\text{He}}^{\text{Mean}}$
$[\text{Tyr+H}]^+$	25	$2.6 \cdot 10^4$	$2.7 \cdot 10^4$
$[\text{Tyr+H}]^+$	23	$5.0 \cdot 10^4$	$5.0 \cdot 10^4$
$[\text{Leu-Enk+H}]^+$	25	$3.0 \cdot 10^4$	$2.9 \cdot 10^4$
$[\text{Leu-Enk+H}]^+$	23	$4.9 \cdot 10^4$	$4.7 \cdot 10^4$
$[\text{2Leu-Enk+H}]^+$	23	$5.4 \cdot 10^4$	$5.5 \cdot 10^4$
$[\text{Ubi+8H}]^{8+}$	17	$1.7 \cdot 10^6$	$1.8 \cdot 10^6$

distributions. As shown in Table 4.3, all the size-dependences described in this and the previous sections remain, within the error bars, unaltered.

In principle, thermal evaporation as a constraint in the pick-up process could explain that a minimum droplet size (prior to pick-up) is required to incorporate an impurity of a certain mass and size. Otherwise, the in comparison large number of helium atoms necessary to dissipate E_{int} would lead to the complete evaporation of the droplet. As mentioned in Section 4.1, this effect has been demonstrated by Lewerenz *et al.* [76]. There, the reduction of droplet size due to thermalisation after the pick-up of a SF_6 molecule set a lower limit of ~ 1000 helium atoms to the size of undoped droplets necessary to incorporate the investigated molecule.

However, thermal evaporation alone can not explain the results presented here. In this work, it is shown that there is a droplet size dependent pick-up process that leads to a minimum size of doped droplets that can be detected.

4.3.4 Possible Constraints on the Pick-up Probability

In order to explain the origin of the droplet size dependent pick-up probability observed here, two different hypotheses are discussed: the role of the kinetic energy on the pick-up process and the possibility of a size dependent stability of the doped droplet.

The Effect of the Kinetic Energy on the Pick-up Probability

A combined experimental and theoretical study is presented on the role of the kinetic energy on the pick-up probability. The main idea is schematically depicted in Figure 4.6. In the pick-up process, the collision kinetic energy is transferred to the droplet and dissipated through friction with the helium environment. Assuming a flat, particle-in-a-box-like potential, a necessary condition to trap an impurity in a helium droplet is that the collision kinetic energy is dissipated while passing through the droplet, such that a kinetic energy remains that is less

than the binding energy to the helium environment. In this section, the following possibility is discussed: the "large" collision kinetic energy characteristic of the larger dopants is not dissipated rapidly enough and, thus, the pick-up process is limited as a function of dopant size.
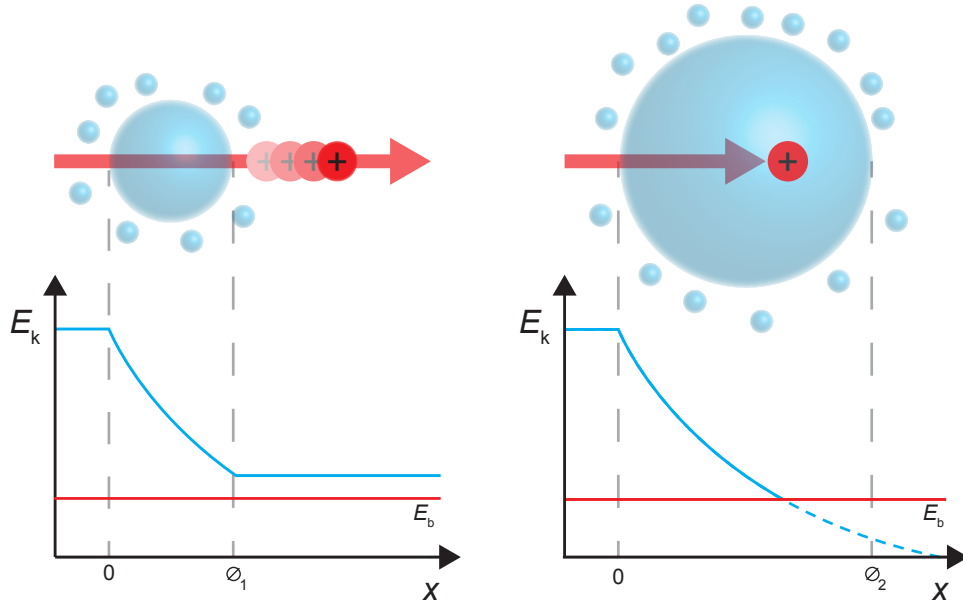
Figure 4.6: To trap a solute, it is proposed that the initial collision kinetic energy (E_k) must fall below the binding energy between the impurity and the helium environment (E_b) within the diameter of the droplet (ϕ).

In order to understand the propagation of molecular ions through liquid helium we used simple models based on classical hydrodynamics. It is important to note that several characteristics of the experiment are simplified for the sake of discussion. First, it is assumed that the investigated species as well as the helium droplets are perfectly spherical. Second, the helium environment surrounding the embedded molecule is assumed to be a fluid with viscosity values independent of the velocity of propagation (assuming the velocity is larger than v_L). Finally, no quantum turbulence effects [137] have been taken into account here. Therefore, the models discussed in the remainder aim at the interpretation of the experimental data rather than at a rigorous theoretical description of the doping process.

Motion of a Particle in Fluid Helium

One of the best-known properties of superfluid helium is its frictionless flow below the so-called Landau velocity, $v_L \sim 58$ m s^{-1} [61]. At higher velocities, helium becomes viscous and exerts a drag force on the impurities due to elementary excitations. The typical relative velocities involved in the pick-up process are large compared to v_L, which leads to friction and dissipation

of the kinetic energy of the impurity in helium.

Thus, during the pick-up, the ions can be considered as moving through a normal, non-superfluid helium liquid. Under such conditions, the ion motion can be described in terms of classical hydrodynamics. The Reynolds number (Re) can be used to determine if the type of flow expected from the motion of an impurity through a fluid corresponds to either the laminar ($Re \leq 0.5$) or the transition regime ($1 \leq Re \leq 1000$) [138]. This dimensionless factor measures the ratio of inertial resistance to viscous resistance for a flowing fluid and can be expressed as

$$Re = \frac{\rho v l}{\eta}, \tag{4.4}$$

where ρ is the density of the fluid, v the relative speed, l the particle diameter, and η the viscosity coefficient. The bulk viscosity of helium at $T = 2.17 \ldots 4.20$ K at saturated vapour pressure is in the range $\eta = (2.50 \ldots 3.25) \cdot 10^{-6}$ kg m^{-1}s^{-1} [62]. Under these conditions, the density of helium is in the range of $\rho = 146 \ldots 105$ kg m^{-3} [62]. Assuming a circular cross-section of the studied ions (see Table 4.2) and initial velocities between 400 m s^{-1} and 500 m s^{-1}, values of the corresponding Reynolds numbers in the range of $Re = 9 - 93$ are obtained.

The Navier-Stokes equation for steady flow of an incompressible fluid moving at a velocity v and pressure p is [139]

$$(\mathbf{v} \cdot \nabla)\mathbf{v} = -\frac{1}{\rho}\nabla p + \frac{\eta}{\rho}\Delta \mathbf{v}. \tag{4.5}$$

From Equation 4.5, the drag force on a spherical particle of radius R moving through a viscous fluid such as bulk helium can be deduced and is given by

$$F = \frac{1}{2}\rho v^2 \pi R^2 C_D, \tag{4.6}$$

where C_D is the drag coefficient. In order to determine the drag coefficient, it is important to note that $(\mathbf{v} \cdot \nabla)\,\mathbf{v}$ and $(\eta/\rho)\Delta \mathbf{v}$ can be approximated as

$$(\mathbf{v} \cdot \nabla)\mathbf{v} \approx \frac{v^2}{l} \qquad \text{and} \qquad \frac{\eta}{\rho}\Delta \mathbf{v} \approx \frac{\eta\, v}{\rho\, l^2}. \tag{4.7}$$

The ratio of the two terms is the Reynolds numbers. Therefore, for small Reynolds numbers the term $(\mathbf{v} \cdot \nabla)\,\mathbf{v}$ can be neglected and Equation 4.5 reduces to a linear equation

$$\eta\Delta \mathbf{v} - \nabla p = 0. \tag{4.8}$$

Thus, for $Re \leq 0.5$, the drag force on the particle is well described by the Stokes' approximation. The flow is expected to correspond to the laminar regime and the drag coefficient is given by [138]

$$C_D = \frac{24}{Re}. \tag{4.9}$$

However, for $1 \leq Re \leq 1000$, the term $(\mathbf{v} \cdot \nabla) \, \mathbf{v}$ can no longer be neglected and the flow is better described by the transition regime. Hence, a correction in the drag coefficient needs to be introduced by adding an additional term to the expansion [138]

$$C_D = \frac{24}{Re} + \frac{3.6 Re^{0.687}}{Re}. \tag{4.10}$$

In addition to the Reynolds number, another point to take into account when describing the motion of a particle through a viscous fluid is the importance of the boundary conditions: in the frame of this work the dopant is not moving through an infinite bath of bulk helium but through finite helium nano droplets.

In a first order approximation, the role of the boundary conditions on the drag coefficient can be determined as a function of a critical distance R_c [139]. At large distances r from the impurity, the term $(\mathbf{v} \cdot \nabla) \, \mathbf{v}$ is of the order $v^2 R/r^2$ and the term $(1/\rho) \, \nabla p$ is of the order of $\eta Rv/\rho r^3$ [139]. Therefore, the condition

$$(\mathbf{v} \cdot \nabla)\mathbf{v} \gg \frac{1}{\rho} \nabla p \tag{4.11}$$

holds only at large distances from the impurity, and thus the flow is better described by the transition regime (Equation 4.10). However, Equation 4.11 shows that the term $(\mathbf{v} \cdot \nabla) \, \mathbf{v}$ can be neglected at small distances from the sphere, and thus the flow is better described by the Stokes' approximation.

Following Equation 4.11, we can roughly approximate the critical distance (R_c) at which the term $(\mathbf{v} \cdot \nabla)\mathbf{v}$ can be neglected as [139]

$$R_c \sim \frac{\eta}{\rho v}. \tag{4.12}$$

For the experimental conditions introduced previously in this section, the critical distance R_c below which the flow is better described by the laminar regime is calculated to be in the range of $R_c \sim 35 - 77$ Å. These values for R_c are of the order of magnitude of the typical radius of the helium droplets investigated in this work (see Table 4.1). Therefore, taking into consideration exclusively the boundary conditions related to the finite size of the helium droplets, the flow would be better described by the Stokes' approximation. However, based solely on Re, the transition regime could provide a more rigorous description of the flow. As a consequence, the choice of approximation necessary to describe the motion of the dopants through the droplet with the current experimental conditions remains unclear. In order to shed more light on this question, the motion will be calculated according to both approximations (Equations 4.9 and 4.10, respectively) and compared to the experimental data in the following section.
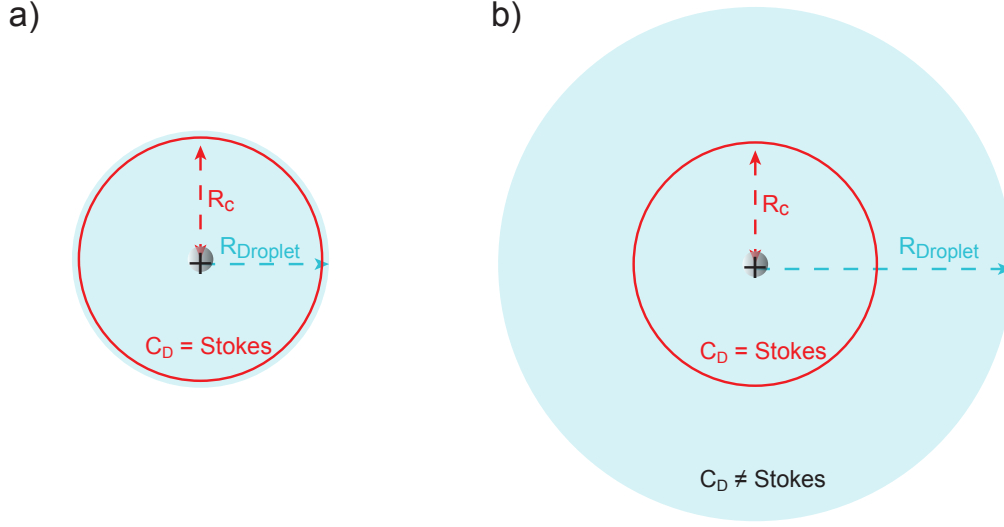
Figure 4.7: The boundary conditions related to the finite size of the helium droplets (blue circles) can be described by the critical distance R_c, the distance between the impurity and the edge of the droplet (red). For a particle moving inside a droplet with a radius smaller or comparable to R_c (panel (a)), the drag coefficient C_D can be approximated by the Stokes' formula. (eq. 4.9). However, for larger droplets (panel (b)), this approximation is no longer valid.

Comparison to the Experimental Results

Using Stokes' formalism as presented above, the drag force on a spherical particle moving through a viscous fluid is

$$F = \frac{1}{2}\rho v^2 \pi R^2 \frac{24}{Re}. \tag{4.13}$$

From Equation 4.13 the velocity of an impurity moving through fluid helium can be deduced and is given by

$$v(t) = v_{\mathrm{D}} e^{-t\frac{6\pi\eta r_{\mathrm{ion}}}{m_{\mathrm{ion}}}}, \tag{4.14}$$

while its position is given by

$$x(t) = \frac{v_{\mathrm{D}} m_{\mathrm{ion}}}{6\pi\eta r_{\mathrm{ion}}}(1 - e^{-t\frac{6\pi\eta r_{\mathrm{ion}}}{m_{\mathrm{ion}}}}). \tag{4.15}$$

In order for a particle to be captured by a droplet its collision kinetic energy must fall below its binding energy to the helium environment (assuming a flat, particle-in-a-box-like potential). Making use of Equation 4.14, it is calculated that the collision energy of small species like $[\mathrm{Tyr+H}]^+$ and $[\mathrm{Leu\text{-}Enk}]^+$ ($E_k \sim 0.7$ eV and ~ 1.4 eV, respectively) is almost completely dissipated on timescales of ~ 30 picoseconds. On the other hand, the dissipation
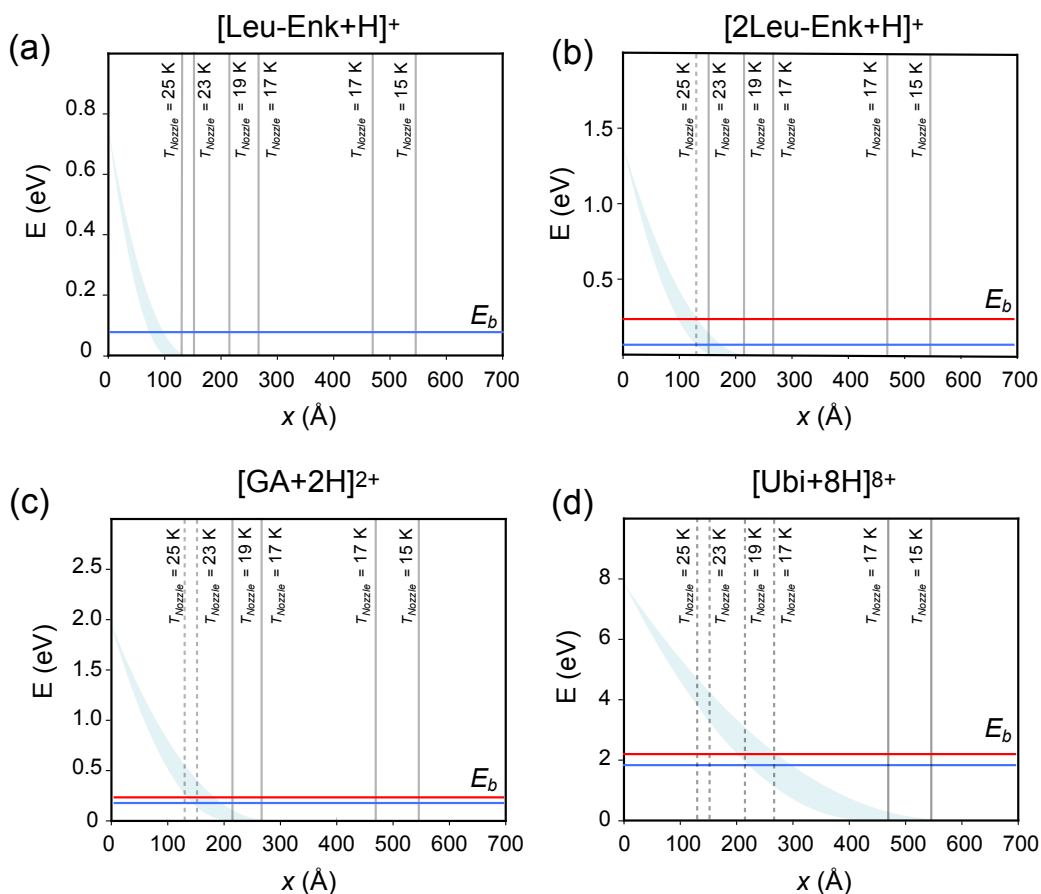
Figure 4.8: Dissipation of the ion kinetic energy as a function of the path length inside ⁴He, obtained using the Stokes' approximation (laminar flow). The results correspond to the following ions: (a) [Leu-Enk+H]$^+$, (b) [2Leu-Enk+H]$^+$, (c) [GA+2H]$^{2+}$, and (d) [Ubi+8H]$^{8+}$. The calculated binding energies (E_b) are displayed as horizontal blue lines. In addition, the experimentally estimated upper boundary of the binding energies are shown in red. The mean diameter of helium droplets for each T_{Nozzle} is shown in grey. The solid line corresponds to the cases where doping was detected experimentally.
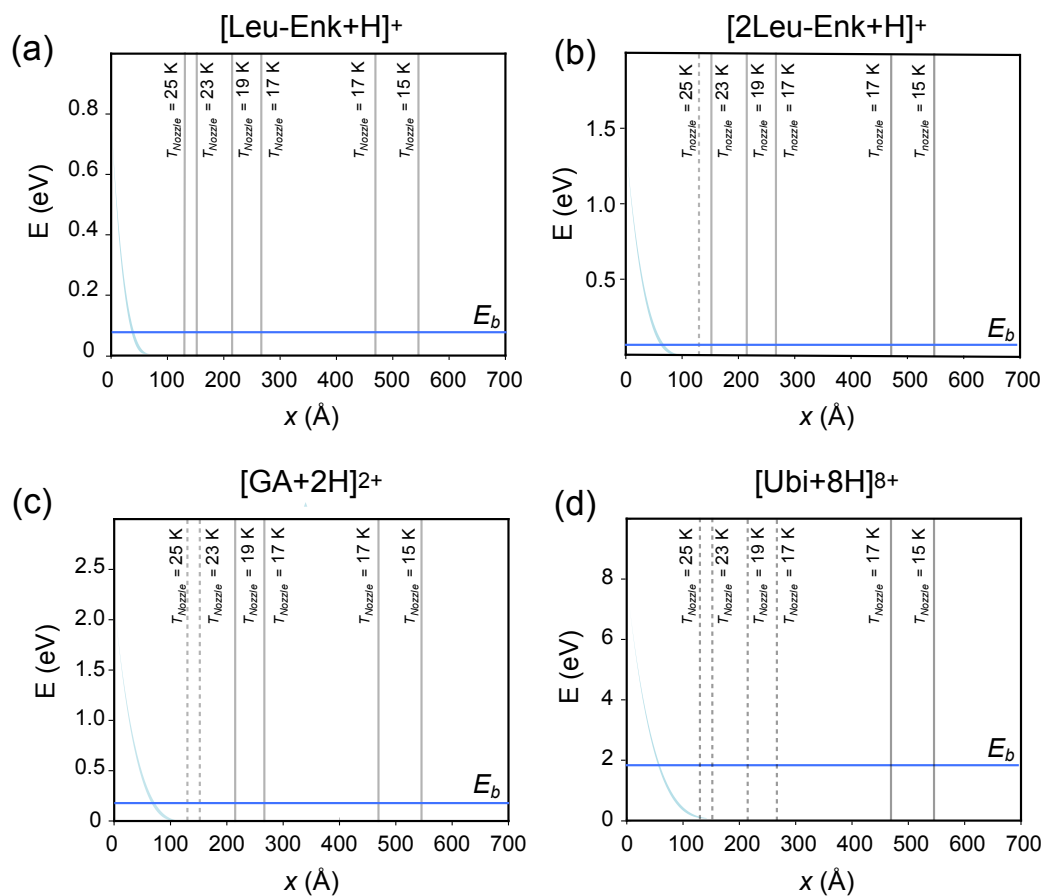
Figure 4.9: Dissipation of the ion kinetic energy as a function of the path length inside ^{4}He, obtained assuming a flow in the transition regime. The results are given for the following ions: (a) [Leu-Enk+H]$^+$, (b) [2Leu-Enk+H]$^+$, (c) [GA+2H]$^{2+}$, and (d) [Ubi+8H]$^{8+}$. The calculated binding energies (E_b) are displayed as horizontal blue lines.

of the kinetic energy of larger ions like [Ubi+8H]$^{8+}$ ($E_k \sim 8$ eV) would require up to 200 picoseconds.

Calculating the distance necessary to sufficiently dissipate the kinetic energy of the collision can be used to predict a minimum droplet size as a function of mass and size of the dopant. Figure 4.8 shows the dissipation of the collision kinetic energy as a function of distance x depicted as the blue-shaded area. The upper and lower limits of the kinetic energy curve correspond, respectively, to the viscosity of helium at 2.17 K and 4.2 K. The calculated and experimentally determined (discussed in detail below) binding energies are displayed as blue and red horizontal lines, respectively. Vertical grey lines mark the mean diameter of the droplets at different T_{Nozzle}. The solid vertical lines indicate the sizes for which the pick-up of each molecule was detected experimentally. In the results shown in Figure 4.8 (a), the kinetic energy of [Leu-Enk+H]$^{+}$ is almost completely dissipated after ~ 100 Å. Therefore, it is predicted that using [Leu-Enk+H]$^{+}$ as a probe will lead to the detection of doped droplets with diameters of at least $x \sim 100$ Å. However, panel (b) shows that ~ 180 Å are required to dissipate the kinetic energy of [2Leu-Enk+H]$^{+}$ below the calculated binding energy. Consequently, the smallest droplet doped with [2Leu-Enk+H]$^{+}$ is expected to have a diameter of $x \sim 180$ Å. Finally, the dissipation of the kinetic energy of even larger ions like [GA+2H]$^{2+}$, panel (c), or [Ubi+8H]$^{8+}$, panel (d), requires distances of $x \geq 200$ Å and $x \geq 400$ Å, respectively.

In a similar fashion, upper boundaries of the experimental binding energies can be determined comparing the dissipation of the kinetic energy shown in Figure 4.8 and the diameter of the largest droplet for which no signal was obtained (shown as dashed, vertical grey lines). Figure 4.8 (a) shows that using [Leu-Enk+H]$^{+}$ as a probe allows to detect doped droplets with diameters of at least ~ 130 Å, the smallest droplet whose size can be determined with the current setup. Therefore, no experimental binding energy can be determined in this case. Panel (b) shows that [2Leu-Enk+H]$^{+}$-doped droplets could be detected with diameters of $x \geq 150$ Å. However, no droplets with a diameter of $x \sim 130$ Å ($T_{\text{Nozzle}} = 25$ K) could be observed using this molecule as a probe. At $x \sim 130$ Å, the kinetic energy in this particular case is calculated to have dissipated until ~ 0.25 eV. Thus, a maximum binding energy of ~ 0.25 eV between [2Leu-Enk+H]$^{+}$ and the droplet is experimentally determined. Following the same approach, upper boundaries of the binding energy of ~ 0.23 eV and ~ 2.2 eV are experimentally obtained for the ions [GA+2H]$^{2+}$ and [Ubi+8H]$^{8+}$, respectively. A complete list of the calculated as well as experimentally determined binding energies can be found in Table 4.4. These values are in remarkably good general agreement with the binding energies calculated as described in Section 4.2.3.

As opposed to the laminar regime presented above, the flow of a particle in the transition regime can no longer be described by the Stokes approximation. In this case, the drag force

Table 4.4: Theoretical binding energy E_b^{theory} and experimental upper boundary of the binding energies for viscosities of helium at a temperature of 2.17 K and 4.2 K, respectively, using the Stokes' approximation.

Dopant	E_b^{theory} (eV)	$E_b^{T\,=\,2.17\ \text{K}}$ (eV)	$E_b^{T\,=\,4.2\ \text{K}}$ (eV)
[Leu-Enk+H]$^+$	0.08	-	-
[2Leu-Enk+H]$^+$	0.08	0.25	0.6
[GA+2H]$^{2+}$	0.18	0.23	0.02
[Ubi+8H]$^{8+}$	2.5	2.2	1.0

on the sphere is given by

$$F = \frac{1}{2}\rho v^2 \pi R^2 \left(\frac{24}{Re} + \frac{3.6 Re^{0.687}}{Re} \right). \tag{4.16}$$

Equation 4.16 can not be analytically solved in order to obtain the velocity and the position of an impurity moving through fluid helium. However, a numerical treatment of Equation 4.16 allows to calculate the dissipation of the kinetic energy of a particle moving through fluid helium as a function of time. As a result, it is calculated that the collision kinetic energy for small species such as [Leu-Enk+H]$^+$ is almost completely dissipated on timescales of ≤ 10 picoseconds while the dissipation of larger species like [Ubi+8H]$^{8+}$ takes place on timescales of ≤ 100 picoseconds.

Figure 4.9 shows the calculated dissipation of the collision kinetic energy as a function of distance x. Comparison with the results displayed in Figure 4.8 shows a much more rapid dissipation of the kinetic energy as a consequence of the extra damping term (see Equations 4.9 *vs.* 4.10). In Figure 4.9 (a) it is observed that the kinetic energy deposited during the pick-up of [Leu-Enk+H]$^+$ falls below the calculated binding energy after only $x \sim 40$ Å. Similarly, distances of $x \sim 60$ Å are necessary in the case of [Ubi+8H]$^{8+}$ (panel (d)). Therefore, assuming a flow in the transition regime it is obtained that doped droplets with diameters down to only $x \sim 130$ Å should be detected, independent of the size and mass of the particle used as a probe. In addition, as a consequence of the very rapid dissipation of the kinetic energy as a function of distance characteristic of this regime, no experimental binding energies can be estimated following this model.

It is important to note that, due to the simplicity of the proposed models, the complex nature of the motion of an ion through a helium droplet, and the number of factors that have not been taken into account in the frame of this work, a cautious interpretation of the presented results is required. On one hand, the remarkably good agreement obtained with the Stokes' model could indicate that the kinetic energy may play an important role in the size-dependent pick-up probability. Further, it could be interpreted as that an insufficient dissipation of the collision energy within the droplet diameter involved in the pick-up of the larger dopants leads to a sharp limit on the minimum doped droplet size that can be detected.

This is in good agreement with the recent results obtained by Chen *et al.* [77]. There, it was suggested that a drop in the doping efficiency with kinetic energy of caesium cations is related to a limited deceleration rate inside a helium droplet. On the other hand, there is a clear disagreement between the experimental and the calculated results when the flow is described by the transition instead of the laminar regime. Although the disagreement could be the consequence of the flow being inadequately described by the transition regime, it could also be interpreted as an indicator of an incomplete picture of the role of the kinetic energy on the droplet size dependent pick-up as discussed here. Nevertheless, the model calculations do predict a clear trend: larger droplets are necessary to equilibrate larger dopants. Further, the discussed model indicates that the minimum droplet size required to pick up a dopant scales with the mass of the dopant over its radius.

In order to confirm this hypothesis, further experiments with full control over the relative velocity between the ion and the droplet for a fixed droplet size are required. In the current experimental setup, the ions are confined inside an ion trap and, thus, their velocity can not be varied. In principle, the velocity of the helium droplets can be tuned over a certain range by changing the temperature of the nozzle or the stagnation pressure. Unfortunately, varying these parameters results in a different size distribution of the produced droplets, thus hindering a systematic investigation.

One possibility to circumvent the problems mentioned above would be, for example, to develop a new ion trap in which the ions can be "bounced" from one end of the trap to another. Although experimentally challenging, such an experimental setup could provide a gradual change in relative velocity between the ion and the droplet. As a consequence, the role of the collision kinetic energy as constraint in the pick-up process could be studied more systematically.

Size Dependent Stability of Doped Droplets

Another possible explanation for the experimental results presented here is the requirement that there is a minimum number of helium atoms necessary to maintain an impurity solvated after pick-up.

The binding energy of an impurity to the entire droplet can be described in terms of the chemical potential μ. Complexes displaying negative μ values are considered *heliophilic*, indicating that a complete immersion of the particle inside the droplet is energetically favourable. To date, all closed shell atoms and molecules investigated have shown to be heliophilic [27]. Therefore, with the exception of alkali atoms, the attractive potential of the helium cluster is expected to solvate the impurity towards the centre of the droplet. However, it is unclear how many helium atoms are necessary to "maintain" the attractive solvation potential necessary to capture an impurity of a certain mass and size. Based on this argument one can establish another factor that determines the size-dependent pick-up process observed here: the minimum ion-doped droplet size measured for each probe represents the number

of helium atoms at which it is still energetically favourable to remain embedded inside the droplet. In other words, if the droplet contains a smaller number of helium atoms the complex becomes *heliophobic*, the impurity-droplet complex becomes unstable, the dopant is "ejected" from the droplet and thus, the ion-doped droplet can not be detected.

Although a rigorous theoretical treatment of this possible pick-up constraint is beyond the scope of this work, future experiments are proposed in order to shed more light into this question. One way to gain insight onto this is to progressively reduce the number of helium atoms of a doped droplet until the complex can no longer be detected. This can be achieved, for example, by making use of the ion ejection process after photo excitation discussed in Section 2.2.4. There, it was discussed that an ion can be ejected from the helium droplet upon absorption of (multiple) resonant photons [33–36]. Although, the mechanisms involved in the ion ejection are not yet fully understood, there is enough experimental evidence demonstrating that it does not result from the total evaporation of helium atoms after photon absorption [33, 34, 81, 82]. Nevertheless, photon absorption is expected to lead to the evaporation of a certain number of helium atoms. The long pulses of IR radiation (~ 10 µs) provided by the FHI FEL are ideal to slowly shrink the size of the doped droplet. The number of helium atoms evaporated after photon excitation can be easily estimated considering that every helium atom leaving the droplet takes away its binding energy of 5 cm^{-1} [62]. Having a precise control over the laser flux as well as a detailed knowledge of the absorption cross section of the selected vibrational mode of the probe molecule allows to calculate how many photons are absorbed. Using this information and monitoring the ejection yield as a function of photon absorption provides an alternative manner to estimate the minimum droplet size for which it is energetically favourable for an impurity to remain solvated.

4.4 Conclusions

In this chapter, the size distributions of a pulsed beam of ion-doped helium droplets consisting of between $\sim 10^4$ to $\sim 10^6$ helium atoms have been characterised. The main focus has been placed on a systematic investigation of the pick-up probability as a function of the mass and size of the dopant. The experimental results demonstrate that there is a droplet size dependent pick-up process that leads to a minimum size of doped droplets that can be detected. However, these results can not be explained in terms of thermal evaporation.

The existence of two possible additional constraints are discussed, namely the role of the kinetic energy and the possibility of a minimum number of helium atoms required for solvation to be energetically favourable. A possible kinematic constraint on the pick-up probability arising from classical hydrodynamics has been investigated comparing the experimental results with simple models. The model calculations indicate that larger droplets are required to equilibrate larger dopants, where the required minimum droplet size scales with the mass over the radius of the dopant. In principle, the good agreement obtained between the experimental data and one of the proposed theoretical models could be interpreted as an indicator of the

existence of such a kinematic constraint. However, a cautious interpretation of the results is required due to the simplicity of the model presented here and further experiments are suggested in order to conclusively demonstrate it. In addition, the possibility that the complex becomes unstable after pick-up for droplets consisting of a certain number of helium atoms has been discussed and further experiments to test the validity of this hypothesis are proposed.

An investigation of the constraints that govern the pick-up process is not only essential for the understanding of its intrinsic properties and dynamics, but also in order to dope impurities in the smallest possible droplet. It has been experimentally demonstrated that the ejection yield after absorption of resonant photons is larger for smaller droplets [33, 34]. The ejection of an ion after photo excitation is routinely employed as a marker for photon absorption in order to obtain vibrational and electronic spectra of ions embedded in helium droplets [33, 34]. Thus, reducing the size of the helium droplets required to dope a certain particle would further facilitate the spectroscopic investigation of molecules using this technique.

5 Infrared Spectroscopy of Protonated Leu-Enkephalin and its 18-crown-6 Complex Embedded in Helium Droplets* *

IR spectra of the protonated five amino acid peptide leu-enkephalin (Tyr-Gly-Gly-Phe-Leu) embedded in superfluid helium droplets have been recorded using a free-electron laser as radiation source. The results show resolved spectra, that are in very good agreement with theoretical calculations, as well as with the available gas-phase data indicating that the helium environment does not induce a significant matrix-shift. The effect of the interaction between the charge and the peptide backbone has been investigated by complexing protonated leu-enkephalin with one 18-crown-6 molecule. The good agreement obtained between the experimental and theoretical results allows for an assignment of a preferred molecular structure.

---

*Chapter based on:

6 Charge-induced Unzipping of Gas Phase Proteins to a Defined Secondary Structure*

The secondary structure of isolated proteins was experimentally investigated at sub-Kelvin temperatures as a function of charge state. The obtained infrared spectra of the proteins ubiquitin and cytochrome c display two distinct absorption bands at positions typical for the condensed phase: the amide I (C=O stretch) and amide II (N-H bend) bands. A new band, however, appears for high charge states that is substantially red-shifted from the amide II band observed at lower charge states. The experimental results are supported by a theoretical study of the proteins' secondary structure. The observations are interpreted in terms of Coulomb-driven transitions in secondary structures from mostly helical to extended C_5-type hydrogen bonded structures. This interpretation is supported by simple energy considerations, as well as by quantum chemical calculations on model peptides. The transition in secondary structure observed here is most likely universal for isolated proteins in the gas phase.

6.1 Introduction

The structure and dynamics of proteins is determined by a delicate balance between various attractive and repulsive interactions. Aside from covalent bonds, various non-covalent interactions such as Pauli repulsion, dispersive interactions, hydrogen bonding, as well as Coulomb interactions shape the potential energy surface and dictate the resulting structural and dynamical preferences. Isolating molecules in the gas phase hinders the interactions with solvents typical in condensed phase experiments. As a result, the interplay between hydrogen bonding and Coulomb repulsion becomes more relevant in structure formation in the gas phase.

In the past, gas-phase ion mobility methods were used to observe the Coulomb driven transition from folded, compact shapes to more elongated conformations [135, 162]. There, the "size" of the ions could be determined by measuring their collision cross-sections as a function of charge for the proteins cytochrome c [135, 162–164] and ubiquitin [164–169], showing that a variety of structures can be populated. For high charge states, presumably helical structures undergo a gradual increase in collision cross-section, which is an indication of a possible unzipping of helices to even more extended structures [135, 164]. However, while ion mobility spectrometry provides information on the overall size and shape of the protein, it is not directly sensitive to structure details such as the secondary structure. This gap can be filled by infrared (IR) spectroscopy, where the position and shape of absorption bands can be used to gain information on the more local secondary structure. Particularly important are the C=O stretching modes (amide I) and N-H bending modes (amide II), since the positions and shapes of their absorption bands are sensitive to the local hydrogen bonding.

Here, the change in secondary structure of the proteins ubiquitin and cytochrome c has been investigated as a function of charge state in the cold environment provided by helium droplets using a free-electron-laser as a radiation source. The experimental results indicate a smooth transition from helical into extended structures that can be traced by distinct bands within the amide II region.

6.2 Materials

Ubiquitin from bovine erytrocytes ($\sim$ 8.5 kDa, Ubi) and cytochrome c ($\sim$ 12 kDa, CytC) from equine heart were purchased from Sigma Aldrich and used without further purification. Each protein was dissolved at 50 µM in a 1:1 H_2O:MeOH solution with 1% formic acid. In order to enhance the number of charges, 15 % propylene carbonate (PC) was added to the mixture. Droplets containing on average $\sim 10^6$ helium atoms were generated at a nozzle temperature of $\sim$ 15 K to embed the investigated proteins.

6.3 Results and Discussion

6.3.1 Ion Ejection and Laser Power Dependence

Figure 6.1 (a) shows several time-of-flight (TOF) mass spectra of the ejected $[CytC+9H]^{9+}$ (left panel) and $[CytC+15H]^{15+}$ ions (right panel) from the droplets upon IR photo excitation for different laser powers. The signals at a mass-to-charge (m/z) ~ 800 and ~ 1400 correspond to the parent ion of $[CytC+15H]^{15+}$ and $[CytC+9H]^{9+}$, respectively. The experimental data of Figure 6.1 (a) and the results on the ejection of the pentapeptide $[Leu-Enk+H]^{+}$ presented in Chapter 5 display very similar trends despite the differences in size and number of charges between dopants. It is observed that high photon densities can lead to the fragmentation of the parent ion. On the other hand, the intensity of the ejected signal diminishes concomitant with a reduction of the laser power until the ejected ions can no longer be observed. Also in this experiment, no helium adducts are present at any measured photon density, thus indicating a remarkably low interaction of the embedded proteins with the helium environment. Moreover, the total absence of helium adducts further supports that the observation of the parent ion is indeed the result of a non-statistical process as opposed to a total evaporation of helium atoms.

The ejection yield as a function of laser power was investigated for two different charge states of cytochrome c, $[CytC+9H]^{9+}$ and $[CytC+15H]^{15+}$, as depicted in Figure 6.1 (b). Similarly to the results obtained in Chapter 5 on the ejection of $[Leu-Enk+H]^{+}$, the efficiency of the ejection of cytochrome c for a given laser power depends on which vibrational mode is being excited. However, comparing the left and the right panel of Figure 6.1 (b) shows that this dependence seems to be much more dramatic in the case of $[CytC+9H]^{9+}$ than for $[CytC+15H]^{15+}$. For $[CytC+9H]^{9+}$, exciting the vibrational modes present at 1550 cm^{-1} leads to a rapid increase of the integrated ion signal with a relatively low laser pulse energy until it saturates at ~ 15 mJ. Contrarily, the vibrational oscillators excited at 1670 cm^{-1} require at least ~ 20 mJ in order to eject the same ion. In this case, no saturation can be observed. Interestingly, the ejection of cytochrome c with a higher number of charges ($[CytC+15H^{15+}]$) seems to yield a very similar behaviour of the ion ejection as a function of laser power for both vibrational modes, 1500 cm^{-1} and 1670 cm^{-1}. The effect of the charge state on the intensity of the ejected signal as a function of vibrational mode will be discussed in more detail later in this chapter.

6.3.2 IR Spectroscopy of Ubiquitin and Cytochrome c Ions

Figures 6.2 and 6.3 show the IR spectra of ubiquitin and cytochrome c ions, respectively, measured in helium droplets. These spectra result from the average of several independent scans recorded over the 1400 cm^{-1} − 1800 cm^{-1} wavenumber range. Depending on the charge state of the parent ion, the spectra have been classified according to their in comparison low (L), intermediate (I), and high (H) number of charges.

a)

b)
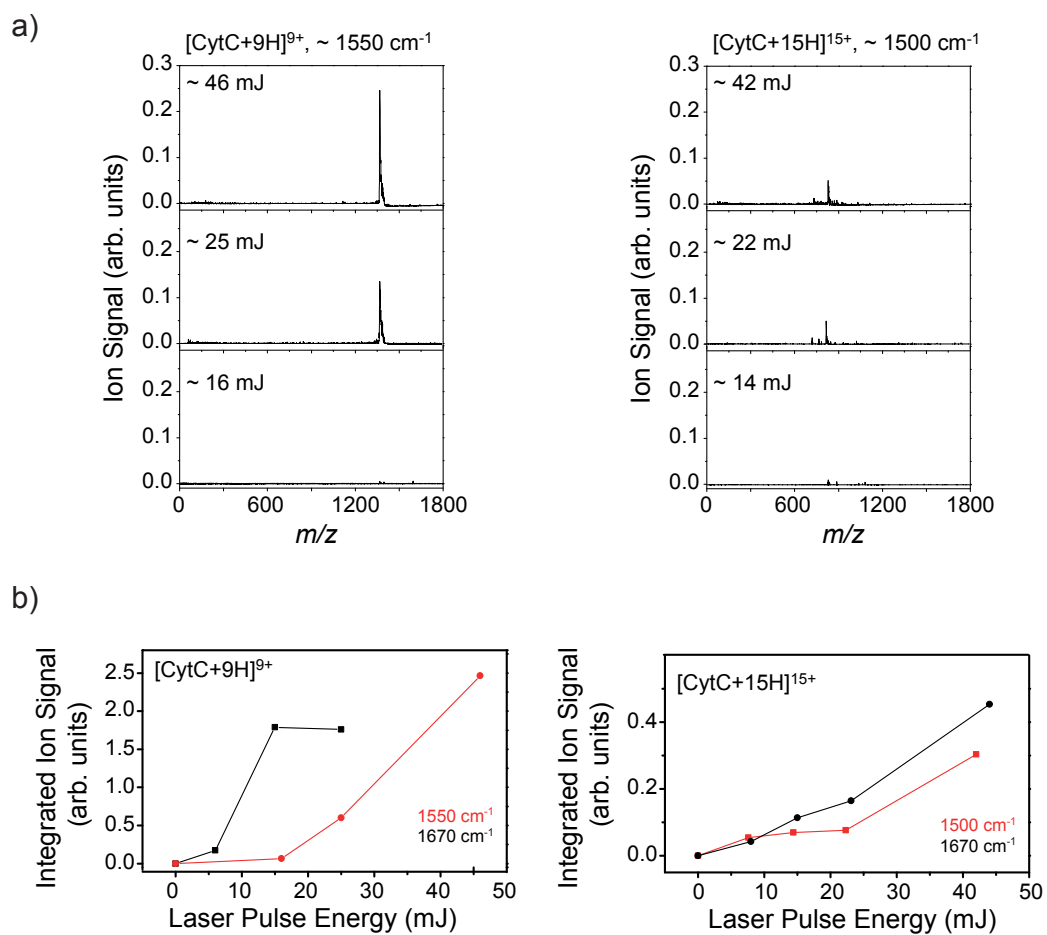
Figure 6.1: a) TOF mass spectra of the ejected $[CytC+9H]^{9+}$ and $[CytC+15H]^{15+}$ ions from the droplets upon IR photo excitation for different laser powers at a wavelength of 1550 cm^{-1} and 1500 cm^{-1}, respectively. b) Integrated signal of the ejected ions $[CytC+9H]^{9+}$ and $[CytC+15H]^{15+}$ as a function of laser power for two different wavelengths.

With the exception of cytochrome c in the 24+ charge state, all spectra show a band near ~ 1650 cm^{-1}. For proteins, a band at this position usually dominates the mid-IR spectrum. It is the so-called amide I band, which stems from protein backbone C=O stretch vibrations. In the spectra shown here, the position of this band is observed to shift to higher wavenumbers with increasing charge state concomitant with a decrease in relative intensity. Between 1400 cm^{-1} and 1600 cm^{-1}, two more bands can be observed. They occur in the region where, for proteins, one band from the backbone N-H bending vibrations (amide II) is expected to be present. However, the experimental results show two bands: one near 1480 cm^{-1} (labeled amide IIa) and one near 1550 cm^{-1} (labeled amide IIb). The amide IIb band is observed only for low and intermediate charge states. In contrast, the amide IIa band appears for intermediate charge states and grows in relative intensity with increasing number of charges while the amide IIb band disappears.

Besides the spectra depicted in Figures 6.2 and 6.3, spectra for most in-between charge states were measured, showing the same trend. The relative intensities of the amide IIa and IIb bands as a function of charge state are shown in Figures 6.4 (a) and (b). Clearly, the curves show a very similar behaviour, with the difference being that the cross-over from amide IIb to IIa is observed to occur around a charge state of 11+ for ubiquitin and 14+ for the larger protein cytochrome c.

It is important to note that the ion ejection mechanism from helium droplets is not yet understood. Moreover, the obtained spectra result from the absorption of multiple photons. Therefore, the relative intensities of the ejected ions should be regarded as a general guide. Due to the time structure of the IR light pulse, consecutive absorption events will take place over a period of several microseconds. Since the ion is embedded in the helium droplet, the molecule will most likely have cooled down to the equilibrium temperature of ~ 0.37 K in between absorption events. As a result, it could be expected that each absorption takes place from a cold ion in its vibrational ground state. Contrary to the experiments using the *IR-MPD* technique [12], anharmonicities are not expected to play a role. This is confirmed by recent IR spectra of peptides in helium droplets [83], as discussed in Chapter 5. Although bands in the spectra scale nonlinearly with absorption cross-section and laser power, here, as a first approximation, a linear correction has been performed dividing the signal by the laser power.

In the condensed phase, amide I bands are typically found in a range between 1654 cm^{-1} for mostly helical or random coil species to 1633 cm^{-1} for β-sheet rich structures. Moreover, the amide I band generally shows a red-shift with increasing hydrogen bonding [1]. Since the position of the band observed here at ~ 1650 cm^{-1} falls in this range, it could be considered an indicator of a mostly helical structure. The amide II band is usually found at ~ 1550 cm^{-1} and its exact position is not as directly correlated to the secondary structure [1]. The position of the amide IIb band observed here is thus in good agreement with the amide II band of proteins in the condensed phase. However, the origin of the amide IIa band can not be assigned in a straight forward manner.

93
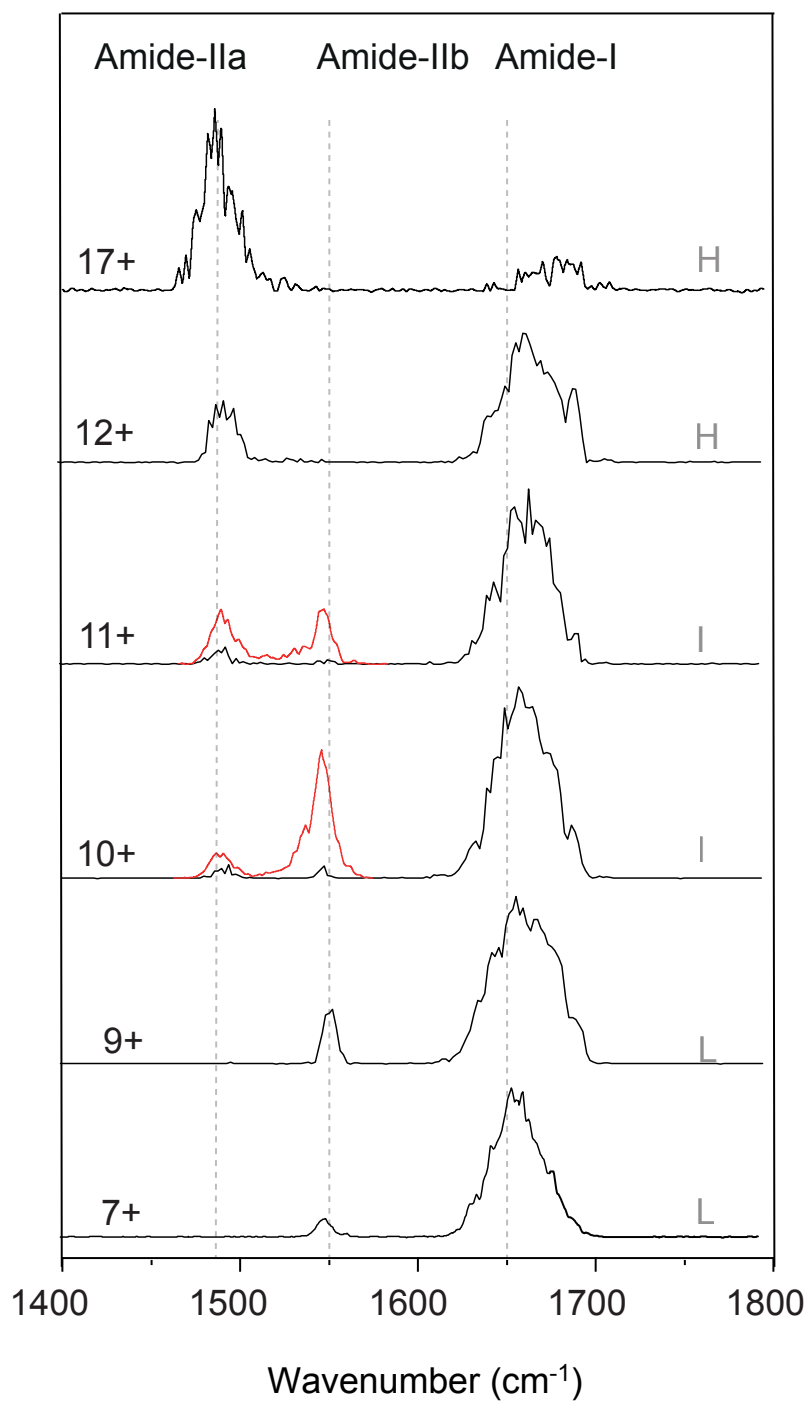
Figure 6.2: IR spectra of ubiquitin as a function of charge state. The regions where a higher photon density was employed are depicted in red.
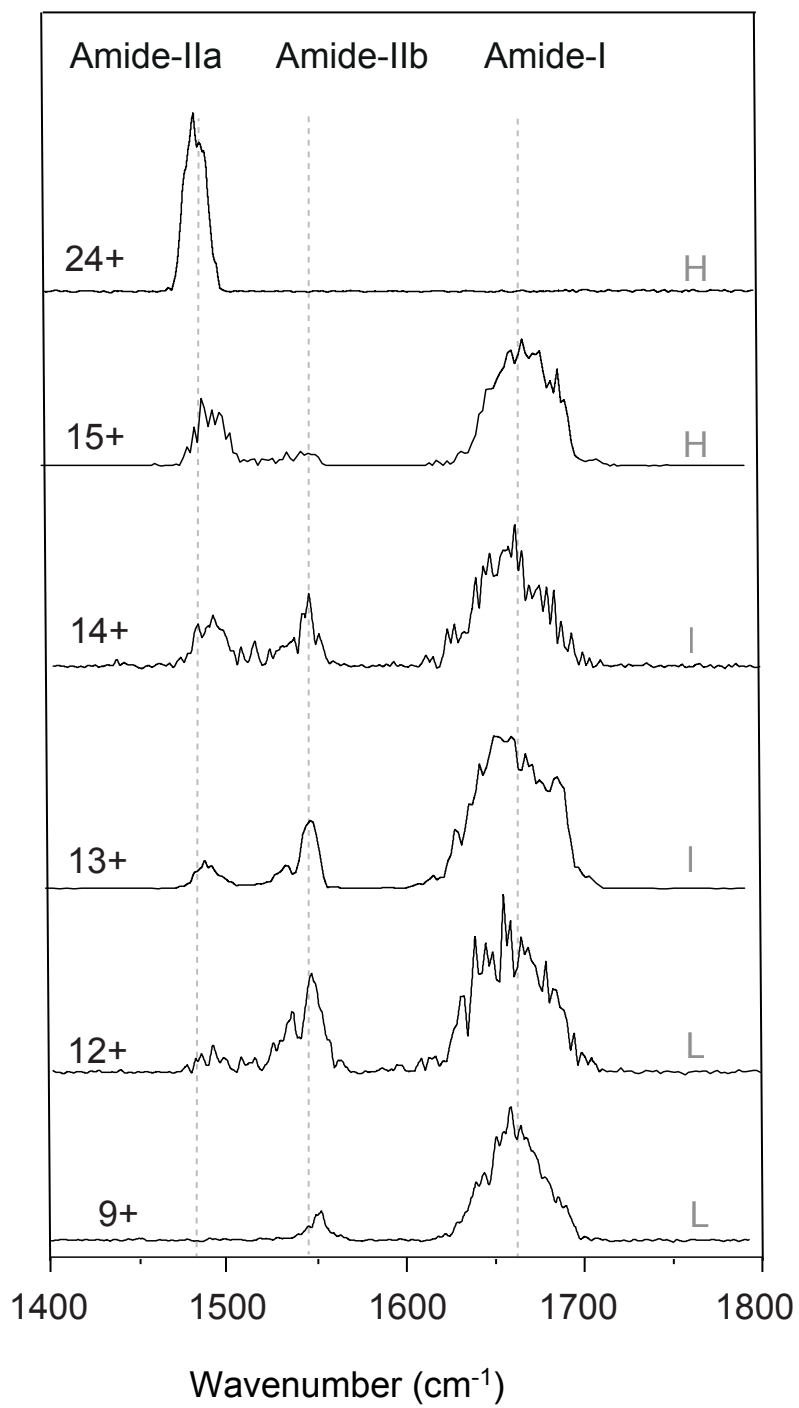
**Figure 6.3:** IR spectra of cytochrome c as a function of charge state.
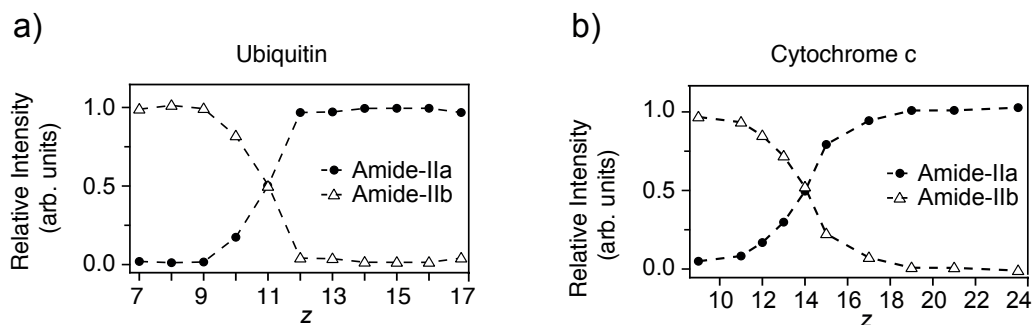
Figure 6.4: Variations in relative intensities of the amide IIa and IIb band as a function of charge state of ubiquitin (panel (a)) and cytochrome c (panel (b)), respectively.

IR spectra of cytochrome c have been measured before over a smaller range of charge states using the *IR-MPD* technique in a room temperature ion trap [170]. The experimental results are reproduced in Figure 6.5 (taken from Ref. [170]). There, qualitatively similar but much broader spectra were observed. Interestingly, the spectra of the higher charge states show an additional band at ~ 1483 cm^{-1} as well. However, in their work [170], a satisfying assignment could not be given.

6.3.3 The Role of Coulomb Repulsion

Ion mobility experiments have shown that increasing the charge on proteins can lead to a transition from compact, possibly native-like structures to more extended, unfolded structures [135, 165]. There, such a transition was observed as a sharp increase in collision cross-section occuring in a charge state range of 7+ to 8+ for cytochrome c [135] and around 6+ to 7+ for ubiquitin [165]. In those experiments, the presence of more extended structures after the initial unfolding has been observed as a gradual increase in collision cross-section with increasing charge. However, the collision cross-section limit of a fully extended string-like structure is predicted to occur at very high values. The experimental cross-sections obtained so far have not reached that limit even for the higher charge states [135, 165]. Nevertheless, an increase in collision cross-section as a function of charge state is consistent with a model based on Coulomb repulsion that predicts such an unfolding at low charge states after which a helical conformation is the most stable one over a large range of charge states. In that model, only at very high charge states is a string-like structure finally lowest in energy [135].

The transition observed here from the amide IIb to IIa band may indicate a drastic change in secondary structure, which occurs over a small range of charge states. Helical structures allow for a stable hydrogen bonding pattern while, at the same time, providing a relatively large distance between the charges in order to minimise Coulomb repulsion. At one point, however, increasing the number of charges and, thus, the Coulomb repulsion, will cause an
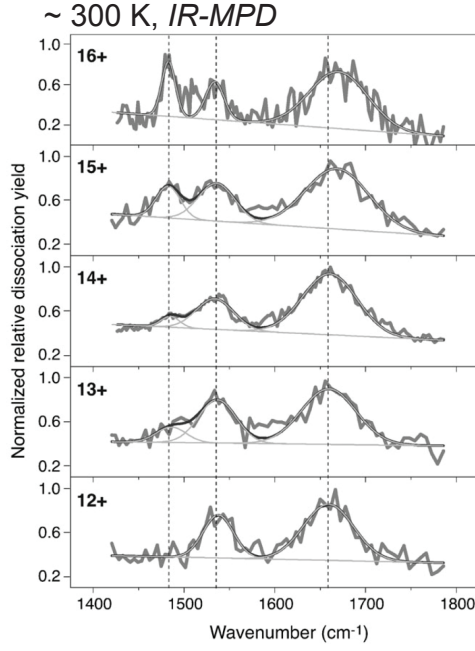
Figure 6.5: The IR spectrum of cytochrome c has been measured at room temperature using the *IR-MPD* technique by Oomens *et al.* [170]. The spectra of the high charge states show an additional band at ~ 1483 cm^{-1} as well.

unzipping of the helix allowing charges to be at even larger distances. Such an unzipped, completely extended structure resembles the backbone orientation of a single strand $\beta-$sheet, with C_5-type hydrogen bonds between adjacent C=O and N-H groups that serve as stabilising elements.

To estimate the energy difference between a helical and a fully extended structure, the corresponding Coulomb potential energy (E_C) of N charges separated by distances r_{ij} can be calculated as

$$E_C = \frac{1}{4\pi\epsilon_0\epsilon_r} \sum_{i=1}^{N} \sum_{j=i+1}^{N} \frac{q_i q_j}{r_{ij}}, \tag{6.1}$$

where ϵ_0 and ϵ_r are the vacuum and relative permittivities, respectively. Assuming N equal charges being distributed equidistant over a length L, Equation 6.1 can be expressed as

$$E_C = \frac{1}{L} \frac{q^2(N-1)}{4\pi\epsilon_0\epsilon_r} \sum_{i=1}^{N} \sum_{j=i+1}^{N} \frac{1}{j-i}. \tag{6.2}$$

The difference between the electric potential energy per amino acid residue (ΔE_C) of an extended and a helical structure as a function of charge state can be calculated as

$$\Delta E_C = \frac{q^2(N-1)}{4\pi\epsilon_0\epsilon r} \left(\frac{1}{3.5 n_A} - \frac{1}{1.5 n_A} \right) \sum_{i=1}^{N} \sum_{j=i+1}^{N} \frac{1}{j-i}, \tag{6.3}$$

where the length of the α-helix is taken as $L_{\text{Helix}} = 1.5 \cdot n_{\text{A}}$ (Å) and that of an extended
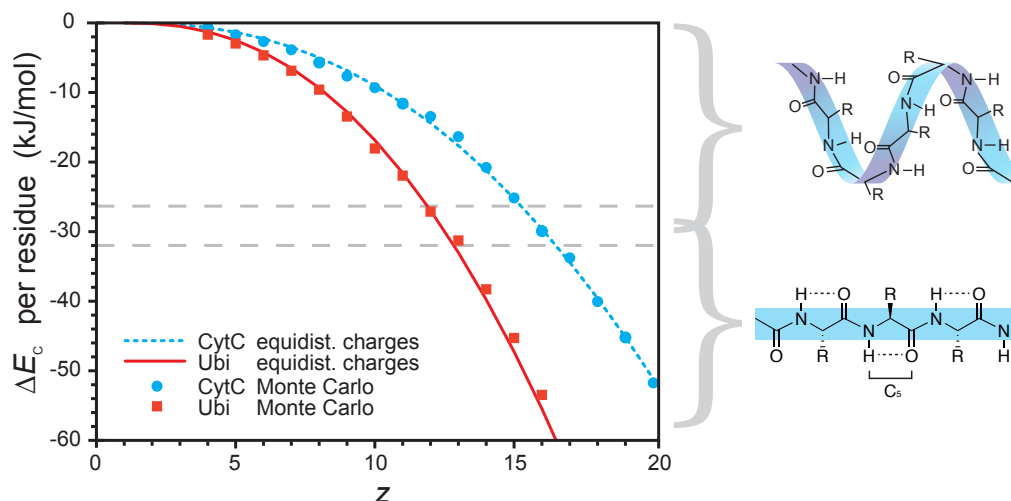
Figure 6.6: Difference in electric potential (ΔE_C) per amino acid residue of ubiquitin and cytochrome c (depicted in red and blue, respectively). The grey, dashed horizontal lines mark the helix stabilisation energy per amino acid residue as calculated in Refs. [171, 172]. A helical structure is preferred for species with ΔE_C smaller than the helix stabilisation energy. Contrarily, species with a larger ΔE_C favour a more extended structure in order to overcome the strong Coulomb repulsion.

structure by $L_{\text{Ext.}} = 3.5 \cdot n_A$ (Å), n_A being the number of amino acids and $\epsilon_r = 1$.

The difference between the electric potential energy per amino acid residue for different charge states is depicted in Figure 6.6. The red and blue lines represent the value ΔE_C obtained for equally spaced charges for ubiquitin and cytochrome c, respectively. In a more realistic model, the molecular charge distribution is based on individual amino acid basicities and Coulomb potential energy. In order to calculate such charge distribution, a Monte Carlo simulated annealing scheme, similar to the approach taken by Schnier *et al.* [173] was used. In this model, the well known amino acid sequences of ubiquitin and cytochrome c (the heme group is ignored) are used. Both the helical and the extended conformations are approximated as linear chains with a total length of $L_{\text{Helix}} = 1.5 \cdot n_A$ (Å) and $L_{\text{Ext.}} = 3.5 \cdot n_A$ (Å), respectively, with equidistant spacing between amino acids. The initial charge distributions are assigned randomly and the annealing parameters are chosen such that the same lowest energy charge distribution is reliably reached for repeated calculations. The resulting ΔE_C values are shown as red squares and blue circles and are in good agreement with the simple equidistant model.

Quantum theory gives, depending on the method, values for the helix stabilisation energy per amino acid with reference to a fully extended structure of ≈ -26.4 [171] and ≈ -32.6 kJ/mol [172]. Those values are shown as grey dashed lines in Figure 6.6. When the charge on the molecule increases, the extended structure becomes more stable once the difference in Coulomb energy ΔE_C falls below the helix stabilisation energy. The model thus predicts
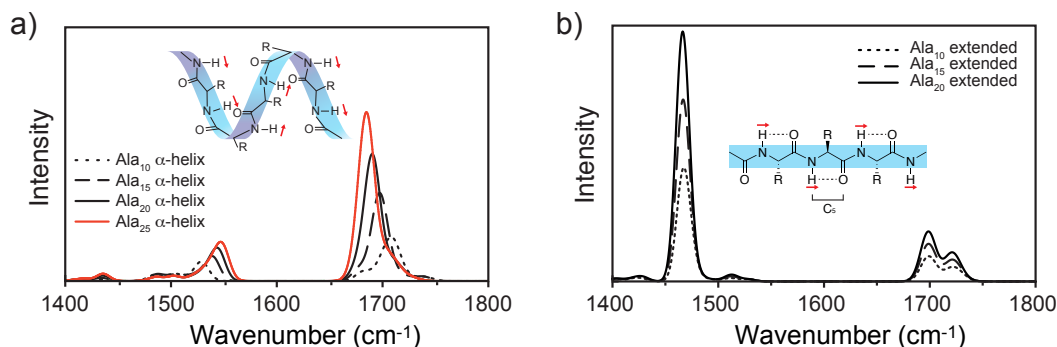
Figure 6.7: The IR spectra of polyalanine peptides with a helical and an extended structure are depicted in panels a) and b), respectively.

that for ubiquitin, an extended structure is favoured starting at around 12+ or 13+ and, for cytochrome c, at around 15+ or 16+. This roughly resembles the charge state region where the experimental transition between amide IIb to amide IIa band occurs. Therefore, a helix unzipping in order to form a C$-$5-type secondary structure seems a viable explanation from an energetic point of view.

6.3.4 Calculated IR Spectra of Polyalanine Peptides[†]

In order to test if a change in the secondary structure such as the unzipping of a helix is supported by the spectral signatures in terms of wavenumber position, IR spectra of polyalanine peptides were calculated for extended C_5-type as well as for helical structures. The calculations were performed at the B3LYP level of theory, using the def2-SVP basis set and adding dispersion corrections using the Grimmer D3 [152], as implemented in Gaussian09 [153]. All vibrational frequencies are scaled by 0.965.

Figure 6.7 (a) shows calculated spectra for Ala_{10} to Ala_{25} in α-helical conformations. Due to an increase in hydrogen bonding and macro-dipole, the amide I band position shifts from 1708 cm^{-1} for the Ala_{10} α-helix to 1685 cm^{-1} for the Ala_{25} α-helix. For the same reason, the amide II band position shifts from 1528 cm^{-1} to 1547 cm^{-1}. In Figure 6.7 (b), the calculated IR spectra for extended conformations are shown. Their amide I and II signatures do not depend significantly on size and show a split amide I band at 1721 cm^{-1} and 1698 cm^{-1} as well as an amide II band at 1466 cm^{-1}.

Interestingly, and in contrast to the spectra calculated for the $\alpha-$helices, the calculated spectra of the extended structures display an amide II band with a much stronger intensity than the amide I band. This effect originates from the directions of the transition dipoles of the N-H and C=O oscillators (depicted as red arrows in the inset of Figures 6.7 (a) and (b)). For the C=O stretching vibration, the transition dipole is oriented parallel to the C=O bond and thus individual transition dipoles can add up constructively in helical structures. On

---

[†]calculations by Gert von Helden

the other hand, the transition dipole of the amide II N-H bending vibration is perpendicular to the N-H bond and parallel with the peptide chain. For a helical structure, this results in transition dipoles that do not add up constructively, thus leading to a reduction in the overall macro transition dipole. For an extended C_5-type structure, however, the individual N-H transition dipoles are again parallel to each other.

The experimental results show a red shift of about 70 cm^{-1} of the amide IIa with respect to the amide IIb band. In the calculations, the red shift observed due to the transition from a helix to an extended structure is about 80 cm^{-1}. It must be noted that the calculations are performed for an idealised structure with no charges, containing only alanine. Hence, the remarkable good agreement between the experimental and the calculated data strongly supports an unzipping as an explanation for the observed change in line positions. Moreover, in the experiment, the intensity of the amide IIa band is observed to strongly increase with charge state until it dominates the spectra of proteins with very high charge states, as predicted by theory. Therefore, helix unzipping into an extended structure for high charge states is supported by the simple electrostatic model as well as by IR spectral simulations, which qualitatively predict the observed changes in peak positions and relative intensities.

6.4 Conclusion

The IR spectra of ubiquitin and cytochrome c ions have been measured as a function of charge state using helium droplets. Due to the good resolution and signal-to-noise ratio of the experimental results, several spectroscopic features can be distinctly identified: for sufficiently high charge states, an additional band is observed in the amide II region. The increase of intensity of this band is concomitant with a decrease in intensity of the bands observed for the low and intermediate charge states.

The experimental results can be explained as a helix unzipping by means of Coulomb repulsion to form a secondary structure that is stabilised by C_5 hydrogen bonds. This is supported by a simple electrostatic model where the number of charges necessary to cause a transition from a helical to an extended structure is calculated. Moreover, the mentioned change in secondary structure is supported both in terms of relative intensities as well as in wavelength positions by the calculated IR spectra of polyalanine complexes. The unzipping is observed for two proteins, ubiquitin and cytochrome c, and has also been observed to occur for other proteins [174].

Indications of such a transition have been previously observed using ion mobility techniques [135, 165, 169]. However, this transition was observed rather as a gradual increase in cross-section with charge state, not quite approaching the calculated limit for a completely linear structure. In this work, it is also not clear if the overall structure is fully linear, and the presence of kinks and bends caused by interactions of the charged side chain groups with the protein backbone can not be fully excluded. However, the spectroscopic evidence presented here shows that for high charge states the structure is at least locally linear and extended

with absence of helical elements. In such an extended structure, only weak C_5 type hydrogen bonding between nearest neighbour N-H and C=O groups is present and the structure is dominated by Coulomb repulsion. While such a single strand $\beta-$sheet structure is not expected to be relevant in the condensed phase, it is likely a universal form of secondary structure in highly charged gas-phase protein ions. Therefore, the experimental results presented here are of fundamental importance for mass spectrometry experiments in which highly charged peptide or protein ions are investigated, for example for protein sequencing.

7 Summary and Future Perspectives

A new experimental setup was developed and made fully operational that combines superfluid helium nano droplets with mass spectrometry and techniques of optical spectroscopy, thus providing a unique environment to investigate mass-to-charge selected molecules at sub-Kelvin temperatures.

Species of interest can be embedded inside liquid helium droplets *via* mechanical impact, the so-called pick-up technique. In this work, helium droplets were doped with biomolecular cations. Due to the presence of an electrical charge, the ion-doped droplets can be directly manipulated and detected. This was used to gain insight into the limitations and constraints of the pick-up process by systematically investigating the pick-up probability for dopants of various sizes and masses by droplets consisting of between $\sim 10^4$ to $\sim 10^6$ helium atoms. To date, thermal evaporation is considered the main factor determining the minimal droplet size required to pick up a certain impurity. However, the experimental results demonstrate that there is a droplet size dependent pick-up process that leads to a minimum size of doped droplets that can be detected. These results cannot be explained in terms of thermal evaporation alone. This was further confirmed by the results obtained from investigating the role of the internal energy of the dopant as a pick-up constraint. Using liquid nitrogen to refrigerate the housing of the new ion trap developed in the frame of this work, allowed to drastically reduce the internal energy of the confined ions prior to pick-up. However, the thereby reduced number of evaporated helium atoms did not alter the minimum size of ion-doped droplets that could be detected.

In order to shed more light onto the pick-up process, the existence of two possible additional constraints are discussed: the role of the kinetic energy and the requirement of a droplet with a minimum number of helium atoms in order to keep an impurity solvated. For pick-up to take place, the collision energy must be dissipated below the binding energy within the droplet diameter (assuming a particle-in-a-box-like potential). The kinematic constraint is based on the idea that the "large" collision energy of the larger dopants that is transferred to the droplet during the pick-up cannot be dissipated rapidly enough. The motion of an ion through liquid helium was studied using simple models based on classical hydrodynamics. Comparison with the experimental results showed strong indications of the existence of such a kinematic constraint. The second constraint discussed here is based on a possible heliophobicity of the system as a function of droplet size. Only droplets consisting of a minimum helium atoms can maintain the attractive solvation potential necessary to capture an impurity of a certain mass and size. Further experiments to test the validity of this hypothesis are proposed.

After being successfully incorporated in a helium droplet, the molecule can be interrogated by means of, for example, infrared (IR) laser spectroscopy. Using the free electron laser facility of the Fritz Haber Institute the vibrational modes of positively charged leucine enkephalin ions were investigated. The experimental results showed a distinctly resolved spectrum that is remarkably well reproduced by the calculated IR spectra [25]. An excellent agreement was obtained as well with gas-phase studies of leucine-enkephalin [25]. Hence, it was concluded that any possible effects of the helium environment are negligible, and that embedding biomolecular cations in a helium matrix yields vibrational spectra that resemble those obtained for the isolated molecules with great accuracy.

The role of charge solvation on the structure of leucine enkephalin was studied by complexing the charged site of this peptide with a 18-crown-6 molecule. As a consequence, the otherwise dominating interaction between the charge and the peptidic backbone was reduced. The experimental results show that disrupting the charge self-solvation has a great impact on the structure and, hence, on the IR spectrum. In order to explain the experimental findings the IR spectra of several low energy conformers were calculated. The high resolution of the IR spectra obtained using helium droplets allowed for an assignment of the molecular structure.

In the last part of this thesis, a combined experimental and theoretical study of the secondary structure of isolated gas-phase proteins as a function of charge state is presented. The IR spectra of the proteins ubiquitin and cytochrome c exhibit an amide I (C=O stretch) and an amide II (N-H bend) band at wavelengths similar to those observed in the condensed phase for helical structures. Increasing the number of charges on the protein leads to a gradual change of the vibrational spectra with the appearance of a new, distinct band in the amide II region. The overall good agreement with a simple theoretical model in terms of energy and spectral signature allowed to rationalise the experimental results in terms of Coulomb repulsion as a charge-induced unzipping of the helical structure to a defined, extended secondary structure that is stabilised by C_5 H-bonds. Moreover, although very different in their native state, both proteins ubiquitin and cytochrome c display a similar unzipping of their helical structure with increasing charge state. Therefore, such an extended structure with C_5 H-bonds is likely to be a universal form of secondary structure in the gas phase.

The experimental results shown here represent the first investigation of the vibrational modes of large biomolecular ions embedded in helium droplets. The systematic study of the characteristics and limitations of helium droplets as a tool to investigate the structure of peptides and proteins at low temperatures also enables further progress towards a deeper understanding of the structural properties of other biological molecules such as, for example, carbohydrates. Carbohydrates are ubiquitous biological polymers of great relevance in nature. However, a detailed structural analysis is challenging due to their branched structures and complex stereochemistry. As a result, only limited information is available about their intrinsic structural properties. Recently, the identification of different carbohydrate anomers has been made possible by means of ion mobility-mass spectrometry techniques [175]. Another step towards an in-depth understanding of the function of carbohydrates is the investigation of

their structure by means of IR spectroscopy. To date, the limited resolution of the vibrational spectra measured at room temperature made an interpretation of the spectral signature rather difficult. However, preliminary results obtained by embedding carbohydrates in the cold, weakly interacting environment of superfluid helium droplets has been observed to yield high resolution spectra with distinctly narrow bands. The potential of this experimental approach is seen from Figure 7.1, where the IR spectra of two trisaccharide anomers is shown. Variation of the glycosidic bond of the last building block from a β- (upper panel) to an α- conformation (lower panel) has a great impact on the structure, yielding a unique spectral signature in each case.
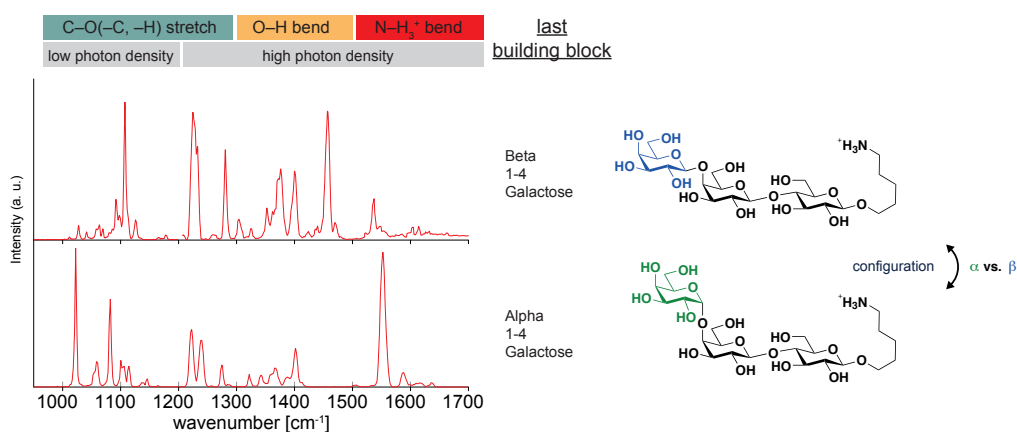
Figure 7.1: IR spectra of two trisaccharides isomers whose last building block is linked by a glycosidic bond in $\beta-$ (upper panel) and $\alpha-$ (lower panel) conformation, respectively.

The setup developed in this thesis also allows for a detailed investigation of fundamental dynamical aspects of superfluid helium itself. Using cations of very different sizes enables to investigate the process by which a particle is ejected from the droplet upon absorption of multiple resonant photons. Although vibrational spectra of ions in helium droplets are typically obtained by monitoring the ejection yield as a function of IR frequency, limited information is available about the process itself. The Fritz-Haber-Institute's free electron laser facility opens new opportunities to shed more light onto the principles and dynamics of the ejection process. For example, the energetics of this process can be systematically characterised as a function of laser fluence, excitation energy, helium droplet size and identity of the dopant based on its absorption cross-section. Further, the dynamics of the ejection process can be studied, for example, by varying the time interval between the micro pulses of the free electron laser. Following this approach could lead to the experimental determination of the cooling rate of the droplet after photo excitation.

Bibliography

[1] Barth, A. *Biochim. Biophys. Acta* **2007**, *1767*, 1073–1101.

[2] Fenn, J. B.; Mann, M.; Meng, C. K.; Wong, S. F.; Whitehouse, C. M. *Mass Spectrom. Rev.* **1990**, *9*, 37–70.

[3] Fenn, J. B.; Mann, M.; Meng, C. K.; Wong, S. F.; Whitehouse, C. M. *Science* **1989**, *246*, 64–70.

[4] Hillenkamp, F.; Karas, M.; Beavis, R. C.; Chait, B. T. *Anal. Chem.* **1991**, *63*, 1193–1202.

[5] Barber, M.; Bordoli, R. S.; Elliott, G. J.; Sedgwick, R. D.; Tyler, A. N. *Anal. Chem.* **1982**, *54*, 645–657.

[6] Pringle, S. D.; Giles, K.; Wildgoose, J. L.; Williams, J. P.; Slade, S. E.; Thalassinos, K.; Bateman, R. H.; Bowers, M. T.; Scrivens, J. H. *Int. J. Mass Spectrom.* **2007**, *261*, 1–12.

[7] Ruotolo, B. T.; Benesch, J. L. P.; Sandercock, A. M.; Hyung, S. J.; Robinson, C. V. *Nat. Protoc.* **2008**, *3*, 1139–1152.

[8] Bohrer, B. C.; Merenbloom, S. I.; Koeniger, S. L.; Hilderbrand, A. E.; Clemmer, D. E. *Annu. Rev. Anal. Chem.* **2008**, *1*, 293–327.

[9] Campbell, S.; Rodgers, M. T.; Marzluff, E. M.; Beauchamp, J. L. *J. Am. Chem. Soc.* **1995**, *117*, 12840–12854.

[10] Wood, T. D.; Chorush, R. A.; Wampler, F. M.; Little, D. P.; O'Connor, P. B.; McLafferty, F. W. *P. Natl. Acad. Sci. USA* **1995**, *92*, 2451–2454.

[11] Wyttenbach, T.; Bowers, M. T. *J. Am. Soc. Mass Spectrom.* **1999**, *10*, 9–14.

[12] Oomens, J.; Sartakov, B. G.; Meijer, G.; von Helden, G. *Int. J. Mass Spectrom.* **2006**, *254*, 1–19.

[13] Polfer, N. C. *Chem. Soc. Rev.* **2011**, *40*, 2211–2221.

[14] Polfer, N. C.; Oomens, J. *Mass Spectrom. Rev.* **2009**, *28*, 468–494.

[15] Miller, D. J.; Lisy, J. M. *J. Phys. Chem. A* **2007**, *111*, 12409–12416.

[16] Nicely, A. L.; Miller, D. J.; Lisy, J. M. *J. Am. Chem. Soc.* **2009**, *131*, 6314–6315.

[17] Kupser, P.; Pagel, K.; Oomens, J.; Polfer, N. C.; Koksch, B.; Meijer, G.; von Helden, G. *J. Am. Chem. Soc.* **2010**, *132*, 2085–2093.

[18] Nagornova, N. S.; Rizzo, T. R.; Boyarkin, O. V. *J. Am. Chem. Soc.* **2010**, *132*, 4040–4041.

[19] Gerlich, D. *Adv. Chem. Phys.* **1992**, *82*, 1–176.

[20] Gerlich, D.; Horning, S. *Chem. Rev.* **1992**, *92*, 1509–1539.

[21] Rizzo, T. R.; Stearns, J. A.; Boyarkin, O. V. *Int. Rev. in Phys. Chem.* **2009**, *28*, 481–515.

[22] Goebbert, D. J.; Wende, T.; Risshu, B.; Meijer, G.; Asmis, K. R. *J. Phys. Chem. A* **2009**, *113*, 5874–5880.

[23] Asmis, K. R.; Neumark, D. M. *Acc. Chem. Res.* **2012**, *45*, 43–52.

[24] Garand, E.; Fournier, J. A.; Kamrath, M. Z.; Schley, N. D.; Crabtree, R. H.; Johnson, M. A. *Phys. Chem. Chem. Phys.* **2012**, *14*, 10109–10113.

[25] Burke, N. L.; Redwine, J. G.; Dean, J. C.; McLuckey, S. A.; Zwier, T. S. *Int. J. Mass Spectrom.* **2014**, *378*, 196–205.

[26] Nagornova, N. S.; Rizzo, T. R.; Boyarkin, O. V. *Angew. Chem. Int. Ed.* **2013**, *52*, 6002–6005.

[27] Toennies, P. J.; Vilesov, A. F. *Angew. Chem. Int. Ed.* **2004**, *43*, 2622–2648.

[28] Goyal, S.; Schutt, D. L.; Scoles, G. *Phys. Rev. Lett.* **1992**, *69*, 933–936.

[29] Hartmann, M.; Miller, R. E.; Toennies, J. P.; Vilesov, A. F. *Science* **1996**, *272*, 1631–1634.

[30] Lindinger, A.; Toennies, J. P.; Vilesov, A. F. *J. Chem. Phys.* **1999**, *110*, 1429–1436.

[31] Stienkemeier, F.; Lehmann, K. K. *J. Phys. B* **2006**, *39*, 127–166.

[32] Bierau, F.; Kupser, P.; Meijer, G.; von Helden, G. *Phys. Rev. Lett.* **2010**, *105*, 133402–4.

[33] Filsinger, F.; Ahn, D.; Meijer, G.; von Helden, G. *Phys. Chem. Chem. Phys.* **2012**, *14*, 13370–13377.

[34] Smolarek, S.; Brauer, N. B.; Buma, W. J.; Drabbels, M. *J. Am. Chem. Soc.* **2010**, *132*, 14086–14091.

[35] Zhang, X.; Brauer, N. B.; Berden, G.; Rijs, A. M.; Drabbels, M. *J. Chem. Phys.* **2012**, *136*, 044305–10.

[36] Loginov, E.; Hernando, A.; Beswick, J. A.; Halberstadt, N.; Drabbels, M. *J. Phys. Chem. A* **2015**, *119*, 6033–6044.

[37] Sanger, F.; Thompson, O. P. *Biochem. J.* **1953**, *53*, 353–366.

[38] Pauling, L.; Corey, R. B.; Branson, H. R. *P. Natl. Acad. Sci. USA* **1951**, *37*, 205–211.

[39] Pauling, L.; Corey, R. B. *P. Natl. Acad. Sci. USA* **1951**, *37*, 251–256.

[40] Whittle, E.; Dows, D. A.; Pimentel, G. C. *J. Chem. Phys.* **1954**, *22*, 1943–1943.

[41] Norman, I.; Porter, G. *Nature* **1954**, *174*, 508–509.

[42] Scheidemann, A.; Toennies, P. J.; Northby, J. A. *Phys. Rev. Lett.* **1990**, *64*, 1899–1902.

[43] Allen, J. F.; Misener, A. D. *Nature* **1938**, *141*, 75.

[44] Kapitza, P. *Nature* **1938**, *141*, 74.

[45] Allen, J. F.; Jones, H. *Nature* **1938**, *141*, 242–244.

[46] Tilley, D. R.; Tilley, J. *Superfluidity and Superconductivity*; IOP Publishing, Bristol, 1990.

[47] Hall, H. E.; Vinen, W. F. *P. Roy. Soc. Lond. A Mat.* **1956**, *238*, 204.

[48] Hall, H. E.; Vinen, W. F. *P. Roy. Soc. Lond. A Mat.* **1956**, *238*, 215–234.

[49] Brauer, N. B.; Smolarek, S.; Loginov, E.; Mateo, D.; Hernando, A.; Pi, M.; Barranco, M.; Buma, W. J.; Drabbels, M. *Phys. Rev. Lett.* **2013**, *111*, 153002–6.

[50] Fárník, M.; Henne, U.; Samelin, B.; Toennies, P. J. *Phys. Rev. Lett.* **1998**, *81*, 3892–3895.

[51] Harms, J.; Toennies, P. J. *Phys. Rev. Lett.* **1999**, *83*, 344–347.

[52] Schlesinger, M.; Mudrich, M.; Stienkemeier, F.; Strunkz, W. T. *Chem. Phys. Lett.* **2010**, *490*, 245–248.

[53] Gomez, L. F.; et al. *Science* **2014**, *345*, 906–909.

[54] Grebenev, S.; Hartmann, M.; Havenith, M.; Sartakov, B. G.; Toennies, P. J.; Vilesov, A. F. *J. Chem. Phys.* **2000**, *112*, 4485–4495.

[55] Stienkemeier, F.; Higgins, J.; Ernst, W. E.; Scoles, G. *Phys. Rev. Lett.* **1995**, *74*, 3592–3595.

[56] Close, J. D.; Federmann, F.; Hoffmann, K.; Quaas, N. *Chem. Phys. Lett.* **1997**, *276*, 393–398.

[57] Bergmann-Schäfer *Gase, Nanosysteme, Flüssigkeiten*; de Gruyter, Berlin, 2006.

[58] Wilks, J.; Betts, D. S. *An Introduction to Liquid Helium*; Clarendon Press, Oxford, 2nd ed., 1987.

[59] Keesom, W. H.; MacWood, G. E. *Physica* **1938**, *5*, 737–744.

[60] Tisza, L. *Nature* **1938**, *141*, 913.

[61] Landau, L. *Phys. Rev.* **1941**, *60*, 356–358.

[62] Donnelly, R. J.; Barenghi, C. F. *J. Phys. Chem. Ref. Data* **1998**, *27*, 1217–1274.

[63] Brooks, J. S.; Donnelly, R. J. *J. Phys. Chem. Ref. Data* **1977**, *6*, 51–104.

[64] Andronikashvilli, E. *J. Phys. USSR* **1946**, *10*, 201–206.

[65] Henshaw, D. G.; Woods, D. B. *Phys. Rev.* **1961**, *121*, 1266–1274.

[66] Guénault, T. *Basic Superfluids*; Taylor & Francis, 2003.

[67] Allum, D. R.; McClintock, P. V. E.; Phillips, A.; Bowley, R. M. *Phil. Trans. R. Soc. A* **1977**, *284*, 179–224.

[68] Gough, T. E.; Knight, D. G.; Scoles, G. *Chem. Phys. Lett.* **1983**, *97*, 155–160.

[69] Gough, T. E.; Mengel, M.; Rowntree, P. A.; Scoles, G. *J. Chem. Phys.* **1985**, *83*, 4958–4961.

[70] Hartmann, M.; Miller, R.; Toennies, P. J.; Vilesov, A. F. *Phys. Rev. Lett.* **1995**, *75*, 1566–1569.

[71] Bartelt, A.; Close, J. D.; Federmann, F.; Quaas, N.; Toennies, P. J. *Phys. Rev. Lett.* **1996**, *77*, 3525–3528.

[72] Toennies, P. J.; Vilesov, A. F. *Annu. Rev. Phys. Chem.* **1998**, *49*, 1–41.

[73] Brink, D. M.; Stringari, S. *Z. Phys. D* **1990**, *15*, 257–263.

[74] Callegari, C.; Lehmann, K. K.; Schmied, R.; Scoles, G. *J. Chem. Phys.* **2001**, *115*, 10090–10110.

[75] Callicoatt, B. E.; Mar, D. D.; Apkarian, V. A.; Janda, K. C. *J. Chem. Phys.* **1996**, *105*, 7872–7875.

[76] Lewerenz, M.; Schilling, B.; Toennies, P. J. *J. Chem. Phys.* **1995**, *102*, 8191–8207.

[77] Chen, L.; Chang, J.; Freund, W. M.; Kong, W. *J. Chem. Phys.* **2015**, *143*, 44310–7.

[78] Gspann, J.; Vollmar, H. *J. Low Temp. Phys.* **1981**, *45*, 343–354.

[79] Buchenau, H.; Toennies, P. J. *J. Chem. Phys.* **1991**, *95*, 8134–8148.

[80] Callicoatt, B. E.; Förde, K.; Jung, L. F.; Ruchti, T.; Janda, K. C. *J. Chem. Phys.* **1998**, *109*, 10195–10200.

[81] Lewis, W. K.; Applegate, B. E.; Sztáray, J.; Sztáray, B.; Baer, T.; Bemish, R. J.; Miller, R. E. *J. Am. Chem. Soc.* **2004**, *126*, 11283–11292.

[82] Lewis, W. K.; Bemish, R. J.; Miller, R. E. *J. Chem. Phys.* **2005**, *123*, 141103–4.

[83] González Flórez, A. I.; Ahn, D.; Gewinner, S.; Schöllkopf, W.; von Helden, G. *Phys. Chem. Chem. Phys.* **2015**, *17*, 21902–21911.

[84] Merritt, J. M.; Douberly, G. E.; Miller, R. E. *J. Chem. Phys.* **2004**, *121*, 1309–1316.

[85] Kwon, Y.; Ceperley, D. M.; Whaley, K. B. *J. Chem. Phys.* **1996**, *104*, 2341–2348.

[86] Nakayama, A.; Yamashita, K. *J. Chem. Phys.* **2000**, *112*, 10966–10975.

[87] Marinetti, F.; Bodo, E.; Gianturco, F. A. *Chem. Phys. Chem.* **2007**, *8*, 93–100.

[88] Di Paola, C.; Bodo, E.; Gianturco, F. A. *Eur. Phys. J. D* **2006**, *40*, 377–385.

[89] Atkins, P.; de Paula, J. *Physical Chemistry*; Oxford University Press, 2014.

[90] Hollas, J. M. *Modern Spectroscopy*; John Wiley & Sons, Ltd, 2005.

[91] Rijs, A. M.; Oomens, J. *Gas-Phase IR Spectroscopy and Structure of Biological Molecules*; Springer, 2015.

[92] MacAleese, L.; Maître, P. *Mass Spectrom. Rev.* **2007**, *26*, 583–605.

[93] Woodin, R. L.; Bomse, D. S.; Beauchamp, J. L. *J. Am. Chem. Soc.* **1978**, *100*, 3248–3250.

[94] Lehmann, K. K.; Scoles, G.; Pate, B. H. *Annu. Rev. Phys. Chem.* **1994**, *45*, 241–274.

[95] Lisy, J. M. *J. Chem. Phys.* **2006**, *125*, 132302–19.

[96] Bieske, E. J.; Dopfer, O. *Chem. Rev.* **2000**, *10*, 3963–3998.

[97] Kamariotis, A.; Boyarkin, O. V.; Mercier, S. R.; Beck, R. D.; Bush, M. F.; Williams, E. R.; Rizzo, T. R. *J. Am. Chem. Soc.* **2005**, *128*, 905–916.

[98] Relph, R. A.; Guasco, T. L.; Elliott, B. M.; Zamrath, M. Z.; McCoy, A. B.; Steele, R. P.; Schofield, D. P.; Jordan, K. D.; Viggiano, A. A.; Ferguson, E. E.; Johnson, M. A. *Science* **2010**, *327*, 308–312.

[99] Goebbert, D. J.; Meijer, G.; Asmis, K. R. *AIP Conf. Proc.* **2009**, *1104*, 22–29.

[100] Levandier, D. J.; Goyal, S.; McCombie, J.; Pate, B.; Scoles, G. *J. Chem. Soc. Faraday Trans.* **1990**, *86*, 2361–2368.

[101] Goyal, S.; Robinson, G. N.; Schutt, D. L.; Scoles, G. *J. Chem. Phys.* **1991**, *95*, 4186–4189.

[102] Choi, M. Y.; Douberly, G. E.; Falconer, T. M.; Lewis, W. K.; Lindsay, C. M.; Merritt, J. M.; Stiles, P. L.; Miller, R. E. *Int. Rev. in Phys. Chem.* **2006**, *25*, 15–75.

[103] Yang, S.; Ellis, A. M. *Chem. Soc. Rev.* **2013**, *42*, 472–484.

[104] Hoffmann, W.; *(private communication)*.

[105] Nauta, K.; Miller, R. E. *Science* **1999**, *283*, 1895–1897.

[106] Nauta, K.; Miller, R. E. *Science* **2000**, *287*, 293–295.

[107] Gutberlet, A.; Schwaab, G.; Birer, O.; Masia, M.; Kaczmarek, A.; Forbert, H.; Havenith, M.; Marx, D. *Science* **2009**, *324*, 1545–1548.

[108] Bierau, F.; Ph.D. thesis; Freie Universität Berlin; 2012.

[109] Kebarle, P. *J. Mass Spectrom.* **2000**, *35*, 804–817.

[110] Wende, T.; Ph.D. thesis; Freie Universität Berlin; 2012.

[111] Jackson, J. D. *Classical Electrodynamics, 3rd ed.*; John Wiley & Sons, 1998.

[112] Abramowitz, M.; Stegun, I. A. *Handbook of Mathematical Functions with Formulas, Graphs, and Mathematical Tables*; Dover Publications Inc., 1972.

[113] Douglas, D. J.; Frank, A. J.; Mao, D. *Mass Spectrom. Rev.* **2005**, *24*, 1–29.

[114] Boyarkin, O. V.; Mercier, S. R.; Kamariotis, A.; Rizzo, T. R. *J. Am. Chem. Soc.* **2006**, *128*, 2816–2817.

[115] Jašík, J.; Žabka, J.; Roithová, J.; Gerlich, D. *Int. J. Mass Spectrom.* **2013**, *354*, 204–210.

[116] Pentlehner, D.; Riechers, R.; Dick, B.; Slenczka, A.; Even, U.; Lavie, N.; Brown, R.; Luria, K. *Rev. Sci. Instrum.* **2009**, *80*, 43302–9.

[117] Pentlehner, D.; Ph.D. thesis; Universität Regensburg; 2010.

[118] Daly, N. R. *Rev. Sci. Instrum.* **1960**, *31*, 264–267.

[119] Schöllkopf, W.; Gewinner, S.; Junkes, H.; Paarmann, A.; von Helden, G.; Bluem, H.; Todd, A. M. M.; *The new IR and THz FEL Facility at the Fritz Haber Institute in Berlin. Proceedings of SPIE 2015, Prague, Czech Republic, April 13-16, 2015.*

[120] Oepts, D.; van der Meer, A. F. G.; van Amersfoort, P. W. *Infrared Phys. Techn.* **1995**, *36*, 297–308.

[121] von Helden, G.; van Heijnsbergen, D.; Meijer, G. *J. Phys. Chem. A* **2003**, *107*, 1671–1688.

[122] Wiley, W. C.; McLaren, I. H. *Rev. Sci. Instrum.* **1955**, *26*, 1150–1157.

[123] Claas, P.; Mende, S. O.; Stienkemeier, F. *Rev. Sci. Instrum.* **2003**, *74*, 4071–4076.

[124] Henne, U.; Toennies, P. J. *J. Chem. Phys.* **1998**, *108*, 9327–9338.

[125] Lewerenz, M.; Schilling, B.; Toennies, P. J. *Chem. Phys. Lett.* **1993**, *206*, 381–387.

[126] Slipchenko, M. N.; Kuma, S.; Momose, T.; Vilesov, A. F. *Rev. Sci. Instrum.* **2002**, *73*, 3600–3605.

[127] Sliter, R.; Gomez, L. F.; Kwok, J.; Vilesov, A. F. *Chem. Phys. Lett.* **2014**, *600*, 29–33.

[128] Humphrey, W.; Dalke, A.; Schulten, K. *J. Molec. Graphics* **1996**, *14*, 33–38.

[129] Allinger, N. L.; Zhou, X.; Bergsma, J. *J. Mol. Struc. - THEOCHEM* **1994**, *312*, 69–83.

[130] Klamt, A.; Schüürmann, G. *J. Chem. Soc. Perkin Trans.* **1993**, *2*, 799–805.

[131] TURBOMOLE V7.0 2015, a development of University of Karlsruhe and Forschungszentrum Karlsruhe GmbH, 1989-2007, TURBOMOLE GmbH since 2007; available from http://www.turbomole.com.

[132] MOPAC2012, James J. P. Stewart, Stewart Computational Chemistry, Colorado Springs, CO, USA, 2012.

[133] Warnke, S.; Baldauf, C.; Bowers, M. T.; Pagel, K.; von Helden, G. *J. Am. Chem. Soc.* **2014**, *136*, 10308–10314.

[134] Warnke, S.; Hoffmann, W.; Seo, J.; *(private communication)*.

[135] Shelimov, K. B.; Clemmer, D. E.; Hudgins, R. R.; Jarrold, M. F. *J. Am. Chem. Soc.* **1997**, *119*, 2240–2248.

[136] Meinhold, L.; Merzel, F.; Smith, J. C. *Phys. Rev. Lett.* **2007**, *99*, 138101–4.

[137] Vinen, W. F.; Niemela, J. J. *J. Low Temp. Phys.* **2002**, *128*, 167–231.

[138] Clift, R.; Grace, J. R.; Weber, M. E. *Bubbles, Drops, and Particles*; Academic Press, 1978.

[139] Landau, L. D.; Lifshitz, E. M. *Fluid Mechanics*; Pergamon Press, 1959.

[140] de Vries, M. S.; Hobza, P. *Ann. Rev. Phys. Chem.* **2007**, *58*, 585–612.

[141] Gerhards, M.; Unterberg, C.; Gerlach, A. *Phys. Chem. Chem. Phys.* **2002**, *4*, 5563–5565.

[142] Canuel, C.; Mons, M.; Piuzzi, F.; Tardivel, B.; Dimicoli, I.; Elhanine, M. *J. Chem. Phys.* **2005**, *122*, 74316–6.

[143] Zwier, T. S. *J. Phys. Chem. A* **2001**, *105*, 8827–8839.

[144] Stearns, J. A.; Boyarkin, O. V.; Rizzo, T. R. *J. Am. Chem. Soc.* **2007**, *129*, 13820–13821.

[145] Nagornova, N. S.; Rizzo, T. R.; Boyarkin, O. V. *Science* **2012**, *336*, 320–323.

[146] Wassermann, T. N.; Boyarkin, O. V.; Paizs, B.; Rizzo, T. R. *J. Am. Soc. Mass Spectrom.* **2012**, *23*, 1029–1045.

[147] Robertson, W. H.; Diken, E. G.; Price, E. A.; Shin, J. W.; Johnson, M. A. *Science* **2003**, *299*, 1367–1372.

[148] Heine, N.; Fagiani, M. R.; Rossi, M.; Wende, T.; Berden, G.; Blum, V.; Asmis, K. R. *J. Am. Chem. Soc.* **2013**, *135*, 8266–8273.

[149] Sztáray, J.; Memboeuf, A.; Drahos, L.; Vékey, K. *Mass Spectrom. Rev.* **2011**, *30*, 298–320.

[150] Polfer, N. C.; Bohrer, B. C.; Plasencia, M. D.; Paizs, B.; Clemmer, D. E. *J. Phys. Chem. A* **2008**, *112*, 1286–1293.

[151] Polfer, N. C.; Oomens, J.; Suhai, S.; Paizs, B. *J. Am. Chem. Soc.* **2007**, *129*, 5887–5897.

[152] Grimme, S.; Antony, J.; Ehrlich, S.; Krieg, H. *J. Chem. Phys.* **2010**, *132*, 154104–19.

[153] Frisch, M. J.; et al.; *Gaussian 09, Revision D.01, Wallingford CT*; 2013.

[154] Banks, J. L.; et al. *J. Comput. Chem.* **2005**, *26*, 1752–1780.

[155] *Schrödinger Release 2014-4: Macromodel, version 10.6, Schrödinger, LLC, New York, NY*; 2014.

[156] Cai, X.; Dass, C. *Rapid Commun. Mass Spectrom.* **2005**, *19*, 1–8.

[157] Julian, R. R.; Beauchamp, J. L. *J. Am. Soc. Mass Spectrom.* **2002**, *13*, 493–498.

[158] Grebenev, S.; Sartakov, B. G.; Toennies, J. P.; Vilesov, A. F. *J. Chem. Phys.* **2003**, *118*, 8656–8670.

[159] da Silva, F. F.; Waldburger, P.; Jaksch, S.; Mauracher, A.; Denifl, S.; Echt, O.; Mark, T. D.; Scheier, P. *Chem. Eur. J.* **2009**, *15*, 7101–7108.

[160] Warnke, S.; Ph.D. thesis; Freie Universität Berlin; 2015.

[161] González Flórez, A. I.; Ahn, D.; Mucha, E.; Gewinner, S.; Schöllkopf, W.; von Helden, G. *Angew. Chem. Int. Ed.* **2015**; http://dx.doi.org/10.1002/anie.201510983.

[162] Clemmer, D. E.; Hudgins, R. R.; Jarrold, M. F. *J. Am. Chem. Soc.* **1995**, *117*, 10141–10142.

[163] Valentine, S. J.; Clemmer, D. E. *J. Am. Soc. Mass Spectrom.* **2002**, *13*, 506–517.

[164] Going, C. C.; Williams, E. R. *Anal. Chem.* **2015**, *87*, 3973–3980.

[165] Valentine, S. J.; Countermann, A. E.; Clemmer, D. E. *J. Am. Soc. Mass Spectrom.* **1997**, *8*, 954–961.

[166] Koeniger, S. L.; Merenbloom, S. I.; Sevugarajan, S.; Clemmer, D. E. *J. Am. Chem. Soc.* **2006**, *128*, 11713–11719.

[167] Koeniger, S. L.; Merenbloom, S. I.; Clemmer, D. E. *J. Phys. Chem. B* **2006**, *110*, 7017–7021.

[168] Koeniger, S. L.; Clemmer, D. E. *J. Am. Soc. Mass Spectrom.* **2007**, *18*, 322–331.

[169] Wyttenbach, T.; Bowers, M. T. *J. Phys. Chem. B* **2011**, *115*, 12266–12275.

[170] Oomens, J.; Polfer, N. C.; Moore, D. T.; van der Meer, L.; Marshall, A. G.; Eyler, J. R.; Meijer, G.; von Helden, G. *Phys. Chem. Chem. Phys.* **2005**, *7*, 1345–1348.

[171] Tkatchenko, A.; Rossi, M.; Blum, V.; Ireta, J.; Scheffler, M. *Phys. Rev. Lett.* **2011**, *106*, 118102–4.

[172] Hua, S.; Xu, L.; Li, W.; Li, S. *J. Phys. B* **2011**, *115*, 11462–11469.

[173] Schnier, P. D.; Gross, D. S.; Williams, E. R. *J. Am. Soc. Mass Spectrom.* **1997**, *8*, 954–961.

[174] Hoffmann, W.; Seo, J.; Warnke, S.; von Helden, G.; Pagel, K.; *Unzipping of model proteins in the gas phase, (in preparation).*

[175] Hofmann, J.; Hahm, H. S.; Seeberger, S.; Pagel, K. *Nature* **2015**, *526*, 241–244.

Publications List

Pick-up probability of molecular ions as a function of mass and size by superfluid helium droplets
A. I. González Flórez, E. Mucha , D. Ahn, B. Sartakov, M. Lemeshko and G. von Helden
(in preparation).

Charge-induced unzipping of gas phase proteins to a defined secondary structure
A. I. González Flórez, E. Mucha , D. Ahn, S. Gewinner, W. Schöllkopf, K. Pagel and G. von Helden
Angew. Chem. Int. Ed. **2015**, DOI: 10.1002/anie.201510983.

Infrared Spectroscopy of Protonated Leu-Enkephalin and its 18-crown-6 Complex Embedded in Helium Droplets
A. I. González Flórez, D. Ahn, S. Gewinner, W. Schöllkopf and G. von Helden
Phys. Chem. Chem. Phys. **2015**, *17*, 21902-21911.

An electrostatic mirror for neutral polar molecules
A. I. González Flórez, S. A. Meek, H. Haak, H. Conrad, G. Santambrogio and G. Meijer
Phys. Chem. Chem. Phys. **2011**, *13*, 18830-18834.

Curriculum Vitae

For reasons of data protection, the curriculum vitae is not published in the electronic version.

Eidesstattliche Erklärung

(gemäß §7, Ziffer (4) der Promotionsordnung vom 20.08.2013 des Fachbereichs Physik an der Freien Universität Berlin)

Die Disseration habe ich selbstständig angefertigt. Alle Hilfsmittel und Hilfen habe ich angegeben, insbesondere habe ich die wörtlich oder dem Sinne nach anderen Veröffentlichungen entnommenen Stellen kenntlich gemacht.

Die Dissertation hat bisher weder in der gegenwärtigen noch in einer anderen Fassung weder dem Fachbereich Physik der Freien Universität Berlin noch einer anderen Fakultät oder Universität vorgelegen.

_____   _____
            Ort, Datum   Unterschrift

Acknowledgments

If one reads the previous works of the students that earned their PhD title in the Molecular Physics department of the Fritz Haber Institute here in Berlin there are two recurrent expressions: great scientific work and even better social atmosphere. My experience here is not any more original - it is indeed a place where science excels while keeping a fantastic social agenda.

First of all I would like to thank my two supervisors: Gert von Helden and Gerard Meijer. I would like to thank Gerard Meijer for taking me under his wing already for my diploma thesis, for giving the opportunity to perform my doctoral thesis and for always being a source of support and great scientific discussions. I would like to thank Gert von Helden, my direct supervisor, for providing me with the possibility to work with a setup as unique as the helium droplets machine, guiding me through my doctoral research and patiently explaining the basics of chemistry to a physicist like me. There are few people as gifted as he is at healing a stubborn machine purely by standing next to it. I believe they call it the supervisor aura. Although not directly my supervisor, I would still like to thank Kevin Pagel for his very helpful insights, for listening to me every time I came by his office to show him a new spectrum and suggesting all the possible reasons that may be behind those sharp lines.

My everyday work at the helium droplets machine was shared, mainly, with two people: Doo-Sik Ahn and Eike Mucha. I would like to thank Doo-Sik for introducing me to the experiment and sharing its pains and glories with me during almost three years. After Doo-Sik left, Eike joined me starting as an extremely gifted undergrad and becoming the best successor the setup could hope for. In addition to his scientific capabilities, his surprisingly wide knowledge of random-facts-of-the-day information and his natural good mood always made the long hours in the lab way more amenable.

Indeed, many hours and long nights were spent in the lab particularly during the beam time shifts. Therefore, I would like to thank Wieland Schölkopf, Sandy Gewinner, Wolfgang Erlebach, and Andreas Liedke. Thank you for the many infrared photons, and for tolerating and giving in when asked for "only 20 more minutes".

I would also like to thank the mechanical workshop for the great work they did in order to develop the new experimental setup. In particular, I would like to thank the head of the workshop, Petrik Bishop. His great work, reliability and good mood always made a pleasure to work with him. The fact that he would turn a blind eye and let me get something done extra fast when I "really, really need it" was also a great bonus.

But research with helium droplets are not only challenging experimental-wise. In order to